# DEVELOPMENT OF AN EMBEDDABLE FIBER OPTIC SENSING SYSTEM FOR MONITORING CHEMICAL PARAMETERS INSIDE CONCRETE

LIN ZHEN

PhD

The Hong Kong Polytechnic University

2026

The Hong Kong Polytechnic University

Department of Civil and Environmental Engineering

**Development of an Embeddable Fiber Optic Sensing System for Monitoring Chemical Parameters inside Concrete**

**LIN Zhen**

A thesis submitted in partial fulfillment of the requirements for the degree of

**Doctor of Philosophy**

July 2025

# CERTIFICATE OF ORIGINALITY

I hereby declare that this thesis is my own work and that, to the best of my knowledge and belief, it reproduces no material previously published or written, nor material that has been accepted for the award of any other degree or diploma, except where due acknowledgement has been made in the text.

__________________________ (Signed)

_________LIN Zhen_________(Name of student)

# DEDICATION

*To my family*

*for their love and support*

# ABSTRACT

Hong Kong, a coastal metropolis, critically depends on marine infrastructure such as bridges and artificial islands to facilitate transportation and underpin economic development. However, those marine infrastructures are inherently impermanent as concrete structures deteriorate due to phenomena such as corrosion, carbonation, and chemical degradation. Chemical parameters like relative humidity, chloride, and sulphate will accelerate deterioration. Proactive monitoring of these parameters can enable early intervention to prevent catastrophic structural failure. Among all the sensing technologies for monitoring chemical parameters inside concrete, fiber optic sensing systems have attracted great interest due to their advantages such as small size, waterproofness and high corrosion resistance, remote monitoring and multiplexing. Nevertheless, field application of fiber optic sensing system for monitoring chemical parameters inside concrete remains rare and the relationship between the fiber optic sensing system signals and chemical parameters is complex.

To address these gaps, this thesis developed two types of embeddable fiber optic sensing systems for monitoring chemical parameters inside concrete including fiber Bragg grating (FBG)-based sensing system and fluorescence-based sensing system, validated their feasibility for the field applications in real marine concrete structure, and employed machine learning to analyze the data collected from the long-term field test of the fiber optic sensing system.

First, an embeddable FBG-based sensing system for monitoring relative humidity inside concrete was developed based on the strain change induced by the swelling or shrinking of the polyimide (PI) coating on FBG sensors under varying humidity conditions. After calibration, the FBG-based sensing system was installed in a concrete beam sample placed in an exposure site to validate long-term field performance. The FBG-based sensing system worked well for more than two years, including under extreme weather conditions.

Then a Gaussian Process (GP) model was trained using the data collected from the long-term field tests of FBG-based relative humidity sensing system and the data collected from an automatic weather buoy to predict the relative humidity inside the concrete beam sample. The GP model provided predictions with 90% confidence level, which consistently encapsulated most measured relative humidity values across multiple channels and seasonal conditions. The results indicated that the GP model provided a viable method for estimating the relationship between the signals from FBG-based sensing system and relative humidity inside the concrete.

Also, an embeddable fluorescence-based sensor for monitoring chloride ions inside concrete was developed, utilizing quinine sulphate as the chloride ion fluorescent indicator. The performance of the developed fluorescence-based sensor for monitoring chloride was tested in chloride ion solutions, concrete simulation solutions with different pH values, solutions containing diverse ions for selectivity assessment, and mortar specimens. The results showed that the fluorescence intensity of the developed fluorescence-based sensor proportionally correlated with the chloride ion concentration in different chloride ion solutions in accordance with the Stern-Volmer law. The fluorescence-based sensor exhibited a remarkable stability across the pH range (8.6-12.6) and had a high selectivity for chloride ions. In the mortar specimens the fluorescence-based sensor's sensitive depths are better than 3 mm and the sensing accuracy for chloride concentration is better than 0.1%. The results indicated substantial potential for field application of the embeddable fluorescence-based sensing system for monitoring chloride inside concrete in the field.

Then a fluorescence-based sensor for monitoring sulphate was developed using scandium-morin complex as the sulphate ion fluorescent indicator. The molarity ratio of scandium and morin was set at 2:1 due to the highest peak intensity in the excitation-emission maps. The scandium-morin complex solution was immobilized as a film on glass substrates using cellulose acetate. Performance tests in sulphate solutions showed that the fluorescence intensity of the developed fluorescence-based sulphate sensor proportionally correlated with the sulphate ion concentration in different sulphate ion solutions in accordance with the Stern-Volmer law. Furthermore, a fluorescence-based sensor for monitoring chloride and sulphate was developed with dual-ion sensing element which had an isolation layer to prevent two fluorescent indicators from contacting. The performance of the sensor was tested in the chloride and sulphate solutions with different concentrations. The results showed that the fluorescence-based sensor for monitoring chloride and sulphate had two peaks and the peaks were sensitive to chloride ions and sulphate ions, respectively. The performance of the embeddable fluorescence-based sensing system for monitoring chloride and sulphate was tested in the wave wall project at Lei Yue Mun. The results showed that the chloride sensitive peak and sulphate sensitive peak had a slow downward trend during the commission. The intensity fluctuation of chloride sensitive peak was larger than that of sulphate sensitive peak.

This study underscores the considerable potential of the field applications of fiber optic sensing systems for monitoring chemical parameters inside concrete enabling a more profound understanding of deterioration mechanisms. And it demonstrates the critical role of machine learning in analyzing the substantial datasets generated by fiber optic sensing system to elucidate relationships between optical signals and target chemical parameters.

# LIST OF PUBLICATIONS

**Journal Papers:**

Qiao H., **Lin Z.**, Sun X.T., Li W., Zhao Y.P., and Guo C.R., 2023. Fiber optic-based durability monitoring in smart concrete: A state-of-art review. *Sensors*. 23(18):7810.

**Lin Z.**, Ouyang Q.F., Guo C.R., and Ni Y.Q., 2024. Fluorescent probe-based fiber optic sensor for real-time monitoring of chloride ions in coastal concrete structures. *Sensors*. 24(12):3700.

**Conference Papers:**

**Lin Z.**, Sun T., and Ni Y.Q.. Fluorescence-based fiber optic sulphate sensor for long term sulphate ion monitoring in concrete structures. *International Workshop on Structural Health Monitoring*, 12-14 September 2023, San Francisco, California, USA.

**Lin Z.**, Ding S.Q., and Ni Y.Q.. FBG-based fiber optic humidity monitoring system for seawater sea-sand concrete and humidity prediction with machine learning. *Ninth Asia-Pacific Conference on FRP in Structures*, 8-11 December 2024, Adelaide, South Australia, Australia.

# ACKNOWLEDGEMENTS

With the thesis being completion, looking back on my journey towards the PhD degree, I am filled with complex emotions, but overall, it has been a delightful journey full of adventures. In this journey, I would like to express my deepest appreciations to all the people who have ever helped me.

First, I would like to give my heartfelt thanks to my supervisor, Prof. Yi-Qing Ni, for offering me the opportunity to pursue a PhD degree. I am sorry that in the early years of my PhD period, my work always did not meet his standards and took a lot of his time helping me revise my work. I can still remember his evaluation of the slides I prepared for the theme-based project task meeting for the first time, "Zhen, you are giving a progress report of your recent work, rather than an introduction to the commercial humidity monitoring sensors purchased for the tests." It is his constant guidance and insightful suggestions during the past five years that has helped me gradually grow into a researcher who meets his standards.

I am also extremely grateful to Prof. Tong Sun, Dr. Si-Qi Ding and Dr. Chuan-Rui Guo. Prof. Tong Sun and her colleagues gave me a lot of suggestions in the development of FBG-based sensors and fluorescence-based sensors. Dr. Si-Qi Ding and Dr. Chuan-Rui Guo spent a lot of time discussing my thesis and new topics. Many thanks.

My sincere gratitude also goes to Prof. Siu-Kai Lai and Prof. Si-Wei Liu for providing valuable suggestions during my confirmation of PhD registration.

I appreciate the financial support from the National Rail Transit and Electrification and Automation Engineering Technology Center (Hong Kong Branch), and Theme-based Research Scheme titled “Sustainable Marine Infrastructure Enabled by the Innovative Use of Seawater Sea-Sand Concrete and Fibre-Reinforced Polymer Composites”.

I am very grateful for the help of the technicians from The University Research Facility in 3D Printing and Water and Waste Laboratories. Many thanks to Hong Kong Observatory for sharing the data from their automatic weather station.

Many thanks to Dr. Yu Xiang, Dr. Li-Ling Fang, Dr. Xiong Sha, and other members in the theme-based research scheme. Successfully completing Task 3 could not have been achieved without their help.

Thanks also to Ms. Wendy, Dr. You-Wu Wang, Dr. Su-Mei Wang, Dr. Wai-Kei Ao, Mr. Xin Ye, Mr. Wei-Jia Zhang, Ms. Qi Zhu, Mr. Lei Yuan, Mr. En-Ze Rui, Mr. Yu-Lin Wang, Ms. Si-Yi Chen, Mr. Gao-Feng Jiang, Mr. Da-Zhi Dang, Mr. Qi-Fan Zhou and all other center colleagues for their kind suggestions and assistance. Special thanks to administrative help from Mr. Tai-Tung Wai, Mr. Wing-Hong Kwan, and assistance from Mr. Shuo Hao.

I also appreciate my friends, Mr. Jun-Jie Li, Mr. Chu Yang, Mr. Kai-Ming Ye and Mr. Yu-Jiang Wang for their warm friendship.

Once again, I would like to thank everyone who has helped me on this journey.

Finally, I want to end this acknowledgment with my sincere thanks to my mom and dad for their support. Thank you all for everything. During Covid, I was not able

to go back home for three years, I am more than ever conscious of home is the warmest harbor. Wish them good health.

# TABLE OF CONTENTS

# LIST OF FIGURES

# LIST OF TABLES

# LIST OF ABBREVIATIONS

| | |
|---|---|
| ANN | Artificial Neural Networks |
| BOTDA | Brillouin Optical Time Domain Analysis |
| BOTDR | Brillouin Optical Time Domain Reflectometry |
| CCTV | Closed Circuit Television |
| CAD | Computer-Aided Design |
| CPE | Customer Premises Equipment |
| DFOS | Distributed Fiber Optic Sensor |
| DTS | Distributed Temperature Sensing |
| EMI | Electromagnetic Interference |
| FBG | Fiber Bragg Grating |
| FOS | Fiber Optic Sensor |
| FRP | Fiber Reinforced Polymer |
| GP | Gaussian Process |
| HGP | heteroscedastic Gaussian Processes |
| HZMB | Hong Kong-Zhuhai-Macao Bridge |
| Fe-C | iron-carbon |
| k-NN | k-Nearest Neighbors |
| LPFG | Long Period Fiber Grating |
| LTE | Long Term Evolution |
| ML | Machine Learning |
| M&F | Modelling and Forecasting |
| MMF | Multimode Fiber |

| | |
|---|---|
| MSM | Multimode-Single-mode- Multimode |
| NTC | Negative Temperature Coefficient |
| NDT | Non-destructive Testing |
| OFDR | Optical Frequency Domain Reflectometry |
| OSA | Optical Spectrum Analyzer |
| PAA | Poly Acrylic Acid |
| PAH | Poly Allylamine Hydrochloride |
| PEEK | Polyether Ether Ketone |
| PMMA | Polymethyl Methacrylate |
| PVC | Polyvinyl Chloride |
| PCA | Principal Component Analysis |
| PPP-BOTDA | Pulse-Pre-Pump BOTDA |
| RI | Refractive Index |
| RL | Reinforcement Learning |
| RH | Relative Humidity |
| SWSSC | Seawater Sea-sand Concrete |
| SMF | Single-Mode Fibers |
| SMS | Single-mode-Multimode-Single-mode |
| SpBS | Spontaneous Brillouin Scattering |
| SLA | Stereolithography |
| STL | Stereolithography |
| SBS | Stimulated Brillouin Scattering |
| SHM | Structural Health Monitoring |
| SMA | Sub-Miniature version A |
| SVM | Support Vector Machines |

| | |
|---|---|
| SPR | Surface Plasmon Resonance |
| TEOS | Tetraethyl Orthosilicate |
| TGP | Treed Gaussian Processes |
| UHPC | Ultra-High-Performance Concrete |
| UV | Ultraviolet |
| UPS | Uninterruptible Power Supply |
| VHGP | Variational Heteroscedastic Gaussian Process |
| VHGP | Variational Heteroscedastic Gaussian Process |
| X-CT | X-Ray Computed Tomography |

# CHAPTER 1. INTRODUCTION

## 1.1 Research Background and Motivations

Hong Kong is a coastal metropolis and relies heavily on marine infrastructures like bridges, artificial islands and so on for convenient transportation and economic development. Concrete remains the predominant construction material for such infrastructure due to its cost-effectiveness and versatility (Shi et al. 2012). Concrete structures in marine environments are inherently susceptible to degradation. Mechanisms including corrosion, carbonation, and chemical degradation compromise structural integrity, shorten service life, and if not addressed promptly, can lead to catastrophic failures.

Consequently, stringent preventative maintenance regimes have been widely adopted in recent decades to mitigate deterioration. However, conventional preventative maintenance focus on physical parameters (e.g., strain, vibration), overlooking the role of chemical factors such as relative humidity, chloride ion concentration, and sulphate ion concentration, all of which critically influence concrete degradation (Angst et al. 2009; Zhang, Hu, et al. 2021; Figueira et al. 2017).

Elevated internal relative humidity significantly compromises concrete durability by accelerating degradation mechanisms. Relative humidity directly influences the physicochemical mechanisms that degrade concrete structure. In regions with elevated RH, the progression of carbonation and corrosion is markedly intensified, posing a significant threat to the structural longevity of concrete. Besides, high moisture levels facilitate the dissolution of atmospheric carbon dioxide ($CO_2$) into concrete, thereby accelerating carbonation, lowering the pH of the concrete and compromising its protective capacity. Concurrently, humid conditions promote the mobility of electrolytic ions (e.g., chlorides and sulphates) within the concrete, enhancing the electrochemical reactions responsible for steel corrosion. These synergistic degradation mechanisms underscore the necessity of continuous relative humidity monitoring in structural health monitoring systems.

Chloride-induced corrosion represents another primary degradation pathway. Steel reinforcement in concrete is maintained in a passive state due to the formation of a protective iron oxide layer on its surface, however, chloride ion exposure disrupts this passive film, which is critical for corrosion resistance, thereby initiating corrosion (Koleva et al. 2017). Partial or complete loss of the passive layer leads to the active corrosion of steel bars. The resulting iron corrosion products are expensive and will generate internal stresses that induce concrete cracking and subsequent structural deterioration. Chloride ions primarily originating from deicing salts or marine environment and atmospheric $CO_2$, are two predominant agents responsible for passive film breakdown and corrosion initiation (Poursaee 2016).

A localized breakdown of the passive layer occurs when enough chloride ion reaches reinforcing bars, and the corrosion process is then initiated. Within concrete, chlorides exist in two distinct phases: (1) free chlorides, dissolved in the pore solution, and (2) bound chlorides, chemically or physically absorbed onto cement hydrates. Only the free chlorides dissolved in the pore solution are responsible for initiating the process of corrosion (Martín Pérez et al. 2000).

Sulphate attack constitutes a significant chemical degradation mechanism, causing expansive cracking, matrix softening, and structural disruption (Hewlett et al. 1998). The deterioration manifests through two primary pathways: (1) the formation of calcium sulphate dihydrate (gypsum), which reduces concrete strength via matrix softening (Khatib 2016) and (2) the crystallization of calcium aluminate tri-sulphate (ettringite), which increases solid volume, inducing internal stresses and cracking (Khatib 2016). These processes are mainly the following two reactions:

$$Ca(OH)_2 + Na_2SO_4 \cdot 10H_2O \rightarrow CaSO_4 \cdot 2H_2O + 2NaOH + 8H_2O \qquad (1\text{-}1)$$

$$\begin{aligned} &2(3CaO \cdot Al_2O_3 \cdot 12H_2O) + 3(Na_2SO_4 \cdot 10H_2O \\ &\rightarrow 3CaO \cdot Al_2O_3 \cdot 3CaSO_4 \cdot 31H_2O + 2Al(OH)_3 + 6NaOH + 17H_2O \end{aligned} \qquad (1\text{-}2)$$

Sulphate attack is broadly classified into internal and external mechanisms. Internal sulphate attack occurs due to the delayed mobilization of sulphate ions within the cement matrix, often triggered by elevated temperatures during curing processes such as steam treatment or mass concrete structures. External sulphate attack is a chemical degradation mechanism where sulphate ions from an external source like underground water, sea water, some earthworks and so on, react with constituents within components of the cement paste (Maierhofer et al. 2010).

Thus, monitoring these chemical parameters inside the concrete is important to address deterioration in advance and prevent catastrophic failure. Among all the new types of sensing technologies for monitoring chemical parameters, fiber optic sensing system has emerged as a highly promising solution for this purpose, offering significant advantages: minimal invasiveness enabling embedded monitoring, inherent corrosion resistance and waterproofness for long-term deployment in harsh environments, remote data acquisition capabilities, and multiplexing potential for reduced system cost per measurement point.

Despite the innovative achievements in the development of the fiber optic sensing system for monitoring chemical parameters, the following challenges remain:

(1) Field Application of Fiber Optic Sensing System: Although previous studies have developed some fiber optic sensing systems for monitoring chemical parameters and have made progress in laboratory validation, there is still a lack of testing under real-world conditions, which limits the verification of the durability and accuracy of the fiber optic sensing systems in complex and varying environments. The transition from controlled laboratory environments to practical field deployment necessitates further investigation.

(2) Application of Fluorescence-Based Sensing System in Monitoring Chemical Parameters inside Concrete: The fluorescence-based sensor is a highly promising technology for monitoring specific anions, (e.g., nitrate, or sulfide) due to their inherent sensitivity, selectivity, and real-time detection capabilities. The fluorescence-based sensing system minimizes interference from other ions and can be integrated into compact, fiber-optic configurations for remote or distributed sensing. However, their application in monitoring chemical parameters inside the concrete remains limited by

challenges in probe stability under harsh conditions. Field validation is needed to ensure reliable performance over long-term deployment.

(3) Machine Learning Integration: The rapid evolution of machine learning (ML) is revolutionizing data analysis worldwide. It can find relationships from massive volumes of data. The reliability of sensor networks during maintenance periods poses a problem, as sensors may go offline, resulting in gaps in data continuity critical for long-term infrastructure assessment. Besides, fiber optic sensing systems generate massive amounts of historical data. Machine learning can autonomously learn from historical and real-time data and makes it particularly suited for predicting chemical parameters inside the concrete structure during maintenance work based on the historical data collected from fiber optic sensing systems. However, there are few studies on the predictions of chemical parameters inside concrete using the data collected from long-term field test of fiber optic sensing system.

In summary, stimulated by the gaps and limitations stated above, this thesis explores the field application of embeddable fiber optic sensing systems for monitoring chemical parameters inside concrete including FBG-based sensing system and fluorescence-based sensing system and applies a GP model to analyze the data collected from the long-term field test of fiber optic sensing system.

## 1.2 Research Objectives

The primary goal of this thesis is field application of the embeddable fiber optic sensing systems for monitoring chemical parameters inside concrete and integration of GP model in the fiber optic sensing system data analysis.

The first objective is the field application of an embeddable FBG-based sensing system for monitoring relative humidity inside concrete. Then, a GP model is trained using data collected from long-term field test of the FBG-based sensing system and data collected from an automatic weather buoy to predict the relative humidity inside the concrete beam sample. The second objective is the field application of an embeddable fluorescence-based sensing system for monitoring chloride and sulphate inside concrete. The specific tasks related to these objectives are summarized below:

I. Develop an embeddable FBG-based sensing system for monitoring relative humidity inside concrete. Install the developed FBG-based sensing system in a concrete beam sample placed in an exposure site to validate the performance of the developed FBG-based sensing system in the field (Chapter 3).

II. Train a GP model with data collected from the long-term field tests of FBG-based sensing system installed in the exposure site and data collected from an automatic weather buoy to predict the relative humidity inside the concrete beam sample (Chapter 4).

III. Develop an embeddable fluorescence-based sensor for monitoring chloride inside concrete. Test the performance of the developed fluorescence-based sensors in chloride solutions, concrete simulation solutions with different pH values, solutions containing diverse ions for selectivity assessment, mortar specimens and high humidity environmental chamber to validate the performance of the fluorescence-based sensor (Chapter 5).

IV. Develop a fluorescence-based sensing system for monitoring chloride and sulphate inside the concrete. Install the developed fluorescence-based sensing system in a wave wall project to validate the performance of the fluorescence-based sensing system in the field (Chapter 6).

## 1.3 Thesis Outline

This thesis consists of seven chapters.

Chapter 1 introduces the motivations and main objectives of this thesis.

Chapter 2 presents a literature review of the status of fiber optic sensors for monitoring chemical parameters. Mover, reviews of principles of fluorescence and quenching, and machine learning aided fiber optic sensing system data analysis are also provided. Then inspirations, limitations and challenges of existing studies are summarized.

Chapter 3 to Chapter 6 presents the main research contents. The first part consists of Chapter 3 and Chapter 4 and focuses on the field application of the embeddable FBG-based sensing system for monitoring relative humidity inside concrete. Chapter 3 proposes the FBG-based relative humidity sensor, followed by installation of the FBG-based sensing system for monitoring relative humidity inside concrete in an exposure site to validate the performance of the sensing system in the field. In Chapter 4, a Gaussian Process model is trained using data collected from the long-term field test of the FBG-based sensing system and data collected from an automatic weather buoy to predict the relative humidity inside the concrete beam sample.

The second part consists of Chapter 5 and Chapter 6 and focuses on the field application of the embeddable fluorescence-based sensing system for monitoring chloride and sulphate inside concrete. Chapter 5 describes the development of the fluorescence-based sensor for monitoring chloride. Then Chapter 5 introduces tests about the response of the developed sensor in chloride ion solutions, concrete simulation solutions with different pH values, solutions containing diverse ions for selectivity assessment, mortar specimens and a high humidity chamber. Chapter 6 introduces the development of the fluorescence-based sensor for monitoring sulphate and optimization of the fluorescent materials molarity ratio. Then describes the development of the fluorescence-based sensor for monitoring chloride and sulphate and introduces tests about the response of the sensor in chloride and sulphate solutions, followed by the installation of the embeddable fluorescence-based sensing system for monitoring chloride and sulphate in a wave wall project to test its performance under real-world conditions.

Chapter 7 summarizes the major conclusions of this thesis and gives recommendations for future research.

# CHAPTER 2. LITERATURE REVIEW

The primary goal of this thesis is the field application of fiber optic sensing system for monitoring chemical parameters inside the concrete, and the application of machine learning in the analysis of the data collected from the long-term field test of fiber optic sensing system. Based on the different research objectives, this chapter provides a review of different fiber optic sensors for monitoring various chemical parameters. Besides relevant topics including principles of fluorescence, quenching and machine learning aided fiber optic sensing system data analysis are also reviewed.

## 2.1 Status of Fiber Optic Sensors for Monitoring Chemical Parameters

### 2.1.1 Introduction

A sensor is a device, module, machine, or subsystem designed to detect changes in its environment and transmit data to other electronic components or systems. In contemporary applications, sensors are ubiquitous; for instance, modern smartphones have integrated diverse sensors such as temperature sensors, accelerometers, magnetometers, gyroscopes, photodetectors (light sensors), barometers (pressure sensors), and gravity sensors (Demchenko 2020).

Fiber optic sensors are among the most widely utilized sensing technologies due to their distinct advantages over conventional sensing technologies. These benefits include the ability to monitor parameters remotely, achieve real-time measurements, operate in compact form factors, resist EMI, withstand water and corrosion, and support multiplexing capabilities. Fiber optic sensors are categorized into various types, such as interferometric, intensity-based, micro bend, polarimetric, wavelength-modulated, distributed, and hybrid sensors. Today, the cost of fiber optic sensing system has significantly reduced and there is an explosion of the research on fiber optic sensing system (Villar et al. 2021).

The operational principle of fiber optic sensors primarily relies on detecting alterations in the properties of light transmitted through the optical fiber cable. Variations in parameters such as intensity, phase, wavelength, or polarization of the light signal are induced by external stimuli. These changes manifest as measurable shifts in the output signal characteristics or reflected wavelength, which can be quantitatively correlated with the physical, chemical, or environmental parameter under investigation.

In this chapter, current status of fiber optic sensors for monitoring chemical parameters are reviewed.

### 2.1.2 FBG-based sensors for monitoring chemical parameters

FBG is one of the most widely employed fiber optic sensing technologies, owing to its unique advantages, including cost-effectiveness, wavelength multiplexing capability, and high linearity (Majumder et al. 2008). Extensive reviews have documented the application of FBG-based sensors in measuring mechanical properties such as strain and displacement (Campanella et al. 2018; Majumder et al. 2008; Zheng et al. 2019). In the following chapter, the application of FBG-based sensors for monitoring chemical parameters in the previous research will be introduced.

*2.1.2.1 Sensing principle of FBG-based sensors*

An FBG contains refraction index with a periodic modulation in the fiber core. This works as a narrowband filter for the incident light (see Figure 2-1). Strain or temperature variations will induce shifts in the reflected central Bragg wavelength (λ) which enable indirect monitoring of chemical parameters.

The relationship between the reflected central Bragg wavelength $\lambda$ and strain change $\Delta\varepsilon$ or temperature change $\Delta T$ in a standard single mode fiber can be given by equation:

$$\frac{\Delta\lambda}{\lambda} = \left(1 - p_{eff}\right)\Delta\varepsilon + (\alpha + \xi)\Delta\mathrm{T} \tag{2-1}$$

In this equation, $\Delta\lambda$ is the change of central wavelength, $p_{eff}$ is the photo-elastic parameter related to the fiber property, $\alpha$ is the thermal expansion coefficient, $\xi$ is the thermal-optic coefficient of fiber core (Hong et al. 2016). The strain changes can be calculated with this equation.

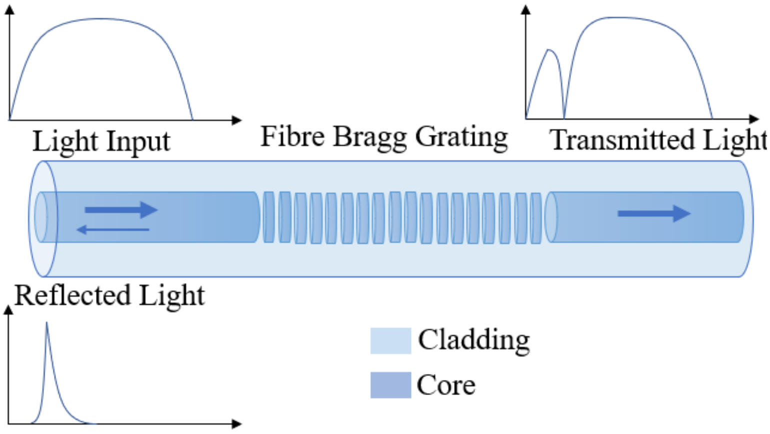


Figure 2-1 Schematic of an FBG

*2.1.2.2 Fabrication of FBG*

The fabrication of FBG typically involves laser-based inscription techniques. Figure 2-2 shows the schematic of laser-beam FBG fabrication system. A laser beam is reflected by a movable mirror and projected through a phase mask positioned parallel to the single-mode fiber. By adjusting the mirror's linear displacement, the laser irradiation produces FBG with precisely controlled grating lengths (Zhang et al. 2010).

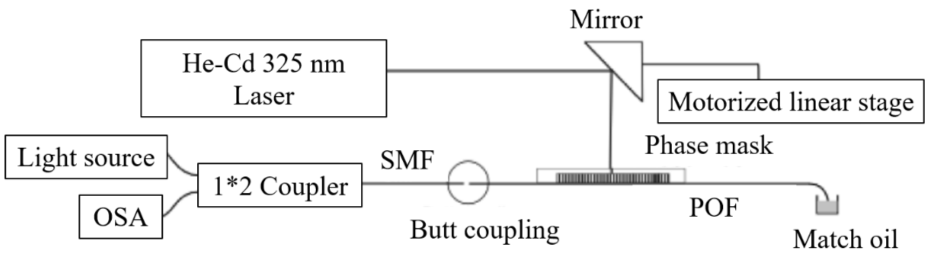


Figure 2-2 Schematic of laser-beam FBG fabrication system (Zhang et al. 2010)

*2.1.2.3 FBG-based sensors for monitoring relative humidity*

Relative humidity is defined as ratio of the partial pressure of water vapor in the air-water mixture at a given temperature. This relationship can be expressed as:

$$RH = \frac{p_{H_2O}}{p_{sH_2O}} \tag{2-2}$$

where $p_{H_2O}$ is the partial pressure of water vapour, and $p_{sH_2O}$ is the saturated water vapour pressure at a given temperature.

FBG coated with humidity-sensitive materials can function as relative humidity sensors due to the strain induced by the hygroscopic swelling or shrinking of the coating material under varying humidity conditions (Kronenberg et al. 2002). Figure 2-3 shows the typical schematic of response test of the FBG-based sensor for monitoring relative humidity in laboratory. In such configurations, saturated salt solutions are employed to generate environments with stable relative humidity, and commercial hygrometers are utilized to validate the relative humidity levels within the chamber.

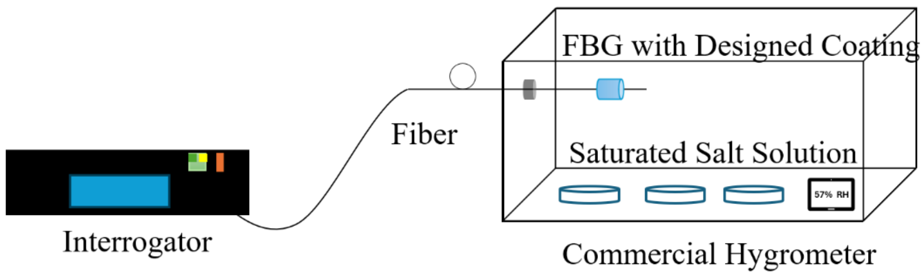


Figure 2-3 Schematic of response test of the FBG-based sensor for monitoring relative humidity in laboratory

Previous studies indicated that agar and polyimide were the most widely adopted humidity-sensitive coatings used in FBG-based sensors for monitoring relative humidity. The sensitivity of these FBG-based sensors, as summarized in Table 2-1, varied depending on the coating material. In the table we can find Massaroni (Massaroni et al. 2017) developed an FBG-based sensor for monitoring relative humidity with agar coating achieved 0.14 nm / 1% RH and this sensor had the highest sensitivity among other FBG-based sensors for monitoring relative humidity listed in the table.

Table 2-1 Summary of current FBG-based sensors for monitoring relative humidity

| Authors | Coating | Sensitivity | Range/1% RH |
|---|---|---|---|
| (Li et al. 2019) | Polyimide | 0.00297 nm / 1%RH | 30-90 |
| (Zhang, Shen, et al. 2021) | Polyimide | less than 0.002 nm / 1%RH | 30-70 |
| (Chai et al. 2018) | Polyimide | 0.00338 nm / 1%RH | 25-95 |
| (Caponero et al. 2018) | Agar | 0.051-0.036 nm / 1%RH | 40-90 |
| (Yeo et al. 2005a) | Polyimide | 0.0056 nm / 1%RH | 23-97 |
| (Guo et al. 2021) | ORMOCER | 0.0024 nm / 1%RH | 11.3-97.3 |
| (Massaroni et al. 2017) | Agar | 0.14 nm / 1%RH | 10-95 |
| (Correia et al. 2012) | Di-Ureasil | 0.0222 nm / 1%RH | 15-95 |
| (Alwis et al. 2016) | Polyimide | 0.005 nm / 1%RH | 20-90 |
| (Yeo et al. 2005b) | Polyimide | 0.0045 nm / 1%RH | 22-97 |

#### *2.1.2.4 FBG-based sensors for monitoring corrosion*

Steel rebar corrosion is one of the most predominant factors compromising the structural integrity and durability of reinforced concrete. Compared to conventional strain gauge sensors, FBG-based sensors for monitoring corrosion exhibit superior advantages, including immunity to chemical degradation and long-term stability, thus suitable for continuous steel corrosion monitoring. The operational principle of FBG-based sensors for monitoring corrosion relies on detecting corrosion product-induced strain, which is mechanically transferred from the degrading steel rebar to the optical fiber cable.

Three primary methodologies exist for transducing corrosion-induced strain in steel rebars to measurable FBG strain:

(1) Fe-C Coating Method: One scheme is to deposit the FBG surface with an iron-carbon (Fe-C) film, which has similar corrosion properties with steel rebar (see Figure 2-4 (a)). Longitudinal dimensional changes in the Fe-C coating due to corrosion reactions induce strain in the FBG, which can be quantified via optical spectrum analyzer (OSA) measurements (Hu et al. 2011).

(2) Fiber Attachment Method: Figure 2-4 (b) and (c) show the schematic of fiber attachment method. The FBG is either helically bound around (Zheng et al. 2009; Chen et al. 2012) or axially aligned with (Almubaied et al. 2017) the steel rebar embedded within the concrete matrix. Dimensional changes of the rebar after corrosion will induce strain in the FBG, which can be quantified via OSA measurements.

(3) Halved Rebar Configuration: Figure 2-4 (d) shows the third method of FBG-based sensor for monitoring corrosion. The steel bar is separated to halves and the FBG is set vertically to the steel axis and is bind on the planed surface (Gao et al. 2011). Expansion of the rebar size after corrosion will induce strain in the FBG, which can be quantified via OSA measurements.

In the latter two methods, radial strain in the steel rebar is mechanically transferred to axial strain in the FBG.

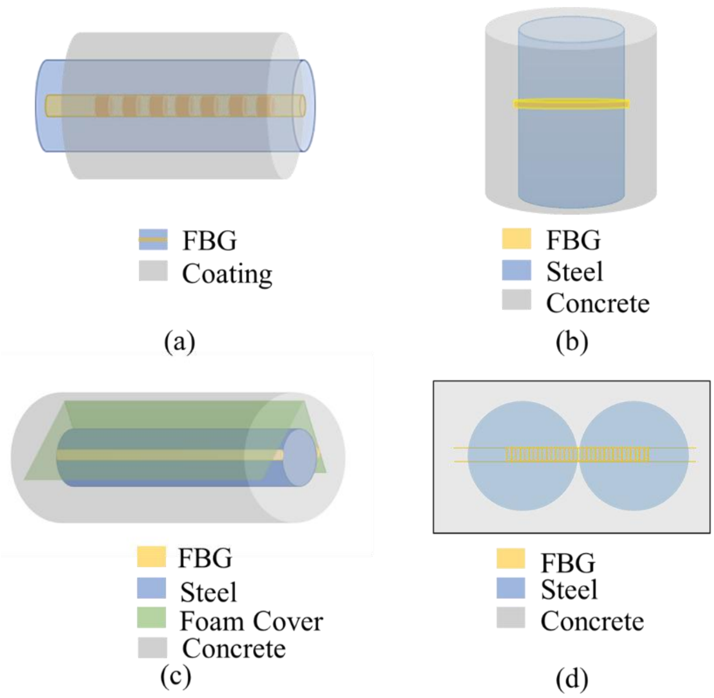


Figure 2-4 Schematic of FBG-based sensors for monitoring corrosion

*2.1.2.5 Summary of FBG-based sensors for monitoring chemical parameters*

FBG sensors have emerged as a transformative technology for structural health monitoring, offering unparalleled advantages over conventional sensing methodologies. Their immunity to EMI, chemical stability, remote multiplexing capabilities, and compatibility with harsh environments position them as a robust solution for real-time, long-term monitoring for chemical parameters. This chapter highlights the versatility of FBG-based sensors for monitoring chemical parameters such as RH, and steel rebar corrosion.

In relative humidity monitoring, hygroscopic coatings (e.g., agar, polyimide) translate moisture induced strain into measurable wavelength shifts. For corrosion detection, FBG sensors transduce steel rebar degradation via Fe-C coatings, helical/axial fiber attachment, or halved-rebar configurations, effectively converting radial or longitudinal strain into optical signals.

While FBG-based sensors hold immense potential for field deployment, challenges remain in ensuring sensor survivability during concrete pouring and optimizing cost effective fabrication. The installation, operation and protection should be carefully considered when designing FBG-based sensing system to provide stable and long-term monitoring of chemical parameters.

### 2.1.3 LPFG-based sensors for monitoring chemical parameters

LPFG has a period from 100 μm to 1 mm (James et al. 2003). The long period fiber grating promotes coupling between the propagating core mode and the co-propagating cladding modes (Rao et al. 2003). This structure makes the wavelength changes with changes of temperature, strain and the refractive index (RI) of the external environment. Variations in parameters such as relative humidity, pH, and chloride content alter the RI, which can be detected by optical spectrum analyzer. Consequently, LPFG-based sensors can monitor chemical parameters.

#### *2.1.3.1 Sensing principle of LPFG-based sensors*

Figure 2-5 shows an LPFG comprising a core, cladding, and periodic gratings. The fiber structure consists of two waveguide components: a high-index core and a low-index cladding. The sensing principle of LPFG-based sensor relies on coupling the light from the fundamental core mode and the forward propagating cladding modes. This coupling causes several resonant wavelengths to emerge in the output spectrum. The resonant wavelength for a specific cladding mode can be derived using coupled-mode theory and the phase-matching condition, as expressed by the following equation (Shu et al. 2002):

$$\lambda = [n_{co}(\lambda) - n_{cl}^{i}(\lambda)]\Lambda \tag{2-3}$$

where $n_{co}(\lambda)$ is the effective refractive index of the propagating core mode at wavelength $\lambda$, $n_{cl}^{i}(\lambda)$is the refractive index of the $i$th cladding mode and $\Lambda$ is the period of the LPFG. The spectral characteristics and central wavelengths of LPFGs are influenced by the grating period, length, and external factors such as temperature, strain, bend radius, and the refractive index of the ambient medium. The changes of RI can be calculated with this equation.

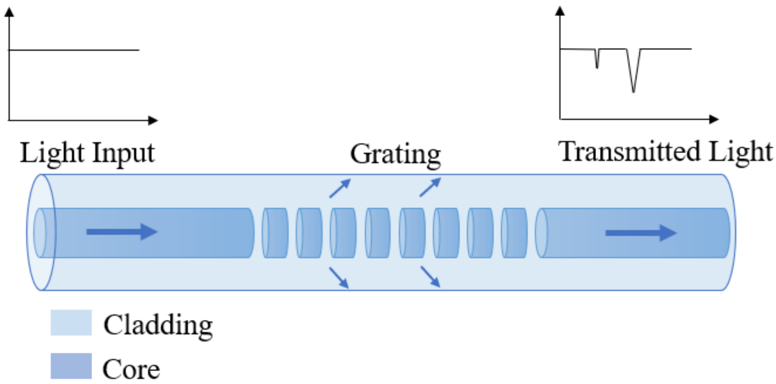


Figure 2-5 Schematic of an LFPG

### *2.1.3.2 Fabrication of LPFG*

The fabrication of LPFG involves introducing periodic refractive index modulations, typically achieved via Ultraviolet (UV) irradiation, ion implantation, or laser irradiation (James et al. 2003). Figure 2-6 shows a typical schematic of laser irradiation LPFG fabrication where a mirror adjusts the laser beam position, and an optical spectrum analyzer monitors the grating formation process.

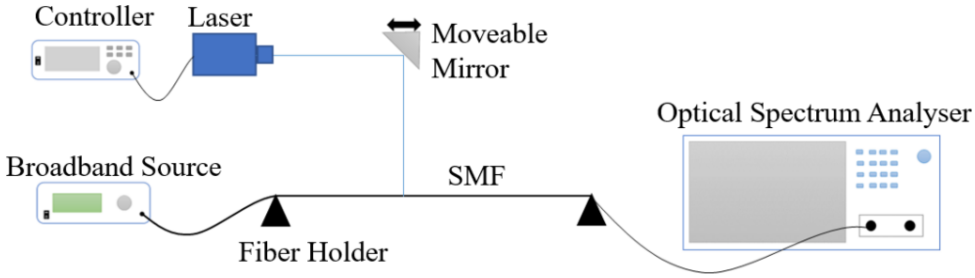


Figure 2-6 Schematic of laser irradiation LPFG fabrication

*2.1.3.3 LPFG-based sensors for monitoring relative humidity*

LPFG sensors have gained prominence in monitoring RH owing to their compact size, high sensitivity, and remote sensing capability. Figure 2-7 shows a schematic of the response test of the LPFG-based sensor for monitoring relative humidity in laboratory. In this configuration, salt solution generates an environment with controlled RH. The coated LPFG sensor is immobilized to eliminate spectral distortions caused by bending or strain. An OSA records the transmission spectrum, while a commercial hygrometer provides reference RH measurements within the chamber. Coated LPFG sensors have demonstrated significant potential for monitoring RH. Relative humidity fluctuations induce swelling or contraction of the hygroscopic coating material, altering its RI and thereby shifting the LPFG's resonance wavelength. Consequently, relative humidity variations can be precisely quantified by tracking these wavelength shifts.

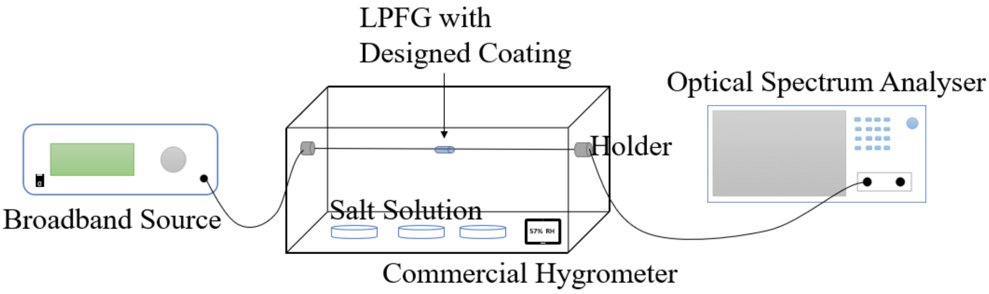


Figure 2-7 Schematic of response test of the LPFG-based sensor for monitoring relative humidity in laboratory

Research efforts explored various coating materials for LPFG-based sensors for monitoring relative humidity, including polyvinyl alcohol (Venugopalan et al. 2008; Liu et al. 2014; Qi et al. 2019), poly allylamine hydrochloride (PAH) and poly acrylic acid (PAA) (Urrutia et al. 2016; Zheng 2014), hydrogel (Yu et al. 2009), gelatin (Tan et al. 2005; Nidhi et al. 2013) and calcium chloride (Fu et al. 2011). Among LPFG-based sensors for monitoring relative humidity, sensors from Fu (Fu et al. 2011) achieved the highest sensitivity (1.36nm/% RH). This high sensitivity was achieved by fiber etching to create air gaps and depositing calcium chloride on the fiber surface (see Figure 2-8). Comparative performance metrics for other LPFG-based sensors for monitoring relative humidity were summarized in Table 2-2. Notably, Theodosiou (Theodosiou et al. 2019) utilized a fiber with multimode cyclic transparent optical polymer. The sensitivity of the developed sensor was 3.3 nm/% RH.

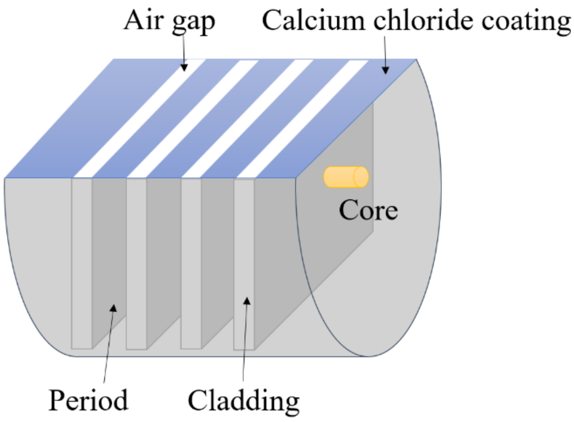


Figure 2-8 Structure of LPFG-based sensor for monitoring relative humidity developed by Fu (Fu et al. 2011)

Table 2-2 Summary of current LPFG-based sensors for monitoring relative humidity

| Author | Coating | Sensitivity | Range |
|---|---|---|---|
| (Venugopalan et al. 2008) | Polyviny alcohol | 0.81 nm / 1% RH | 53-75 |
| (Liu et al. 2014) | Polyviny alcohol | 0.1723nm / 1% RH | 20-80 |
| (Qi et al. 2019) | Polyviny alcohol | 0.07018 nm / 1% RH | 32-99 |
| (Konstantaki et al. 2006) | Poly(ethylene oxide)/cobalt chloride (PEO/$CoCl_2$) | 0.185 nm / 1% RH | 50-77 |
| (Alwis et al. 2013) | Polymide coating and silver mirror at the end | 0.10 nm / 1% RH | 20-80 |
| (Urrutia et al. 2016) | PAH/PAA | 0.06323 nm/ 1%RH | 20-80 |
| (Zheng 2014) | PAH/PAA and $Al_2O_3$/PSS | 0.04 nm / 1% RH | 20-90 |
| (Yu et al. 2009) | Hydrogel coating | 0.0099 nm / 1% RH | 60-100 |
| (Liu et al. 2007) | Hydrogel coating (acrylic acid and vinyl pyridine) | 0.2 nm / 1% RH | 38.9-100 |
| (Tan et al. 2005) | Gelatin coating | 0.833% RH / dBm | 90-99 |
| (Nidhi et al. 2013) | Gelatin/Cobalt Chloride Coating | 0.18 nm/ 1% RH | 35-90 |
| (Fu et al. 2011) | Calcium chloride coating and air gap produced by fiber etching methods | 1.36 nm / 1% RH | 55-95 |
| (Dissanayake et al. 2018) | Graphene oxide | 0.15 dB / 1%RH | 60-95 |
| (Theodosiou et al. 2019) | Multimode cyclic transparent optical polymer | 3.3 nm / 1%RH | 20-40 |
| (Hromadka et al. 2019) | Silica nanoparticles | 0.53 nm/ 1% RH | 35-98 |

*2.1.3.4 LPFG-based sensors for monitoring chloride*

Early investigations into LPFG-based sensors for monitoring chloride were conducted by Tang (Tang et al. 2007), Abi Kaed Bey (Abi Kaed Bey et al. 2008), and Possetti (Possetti et al. 2009). The detection limit was 0.0001% or ∼1 ppm and showed great potential of the application of LPFG-based sensors for monitoring chloride. As summarized in Table 2-3, these sensors achieved a maximum sensitivity of approximately 1 ppm, positioning them as highly precise tools for chloride concentration detection.

Table 2-3 Summary of current LPFG-based sensors for monitoring chloride

| **Author** | **Coating** | **Sensitivity** |
|---|---|---|
| (Laxmeshwar et al. 2018) | - | 0.02848 nm / ppm |
| (Li et al. 2018) | - | 1.26 nm / 1% NaCl |
| (Possetti et al. 2009) | - | 0.00661 nm / $g.L^{-1}$ (NaCl) |
| (Yang et al. 2019) | Hydrogel | 7 nm / M (125.5 pm/‰) |
| (Yang et al. 2017) | Polyelectrolyte | 36 nm / M |
| (Tang et al. 2007) | Gold colloids | 0.071 nm / 1% NaCl |

*2.1.3.5 LPFG-based sensors for monitoring corrosion*

To monitor the corrosion inside the concrete structure, researchers have developed specialized sensors for monitoring corrosion utilizing LPFG technology. Liu (Liu et al. 2012) introduced an LPFG-based sensor for monitoring corrosion. This sensor used phenolic resin as sensing material (see Figure 2-9). In this design, the dissolution of solid rust within the resin altered the RI of the LPFG, inducing a measurable resonance wavelength shift detected via an OSA. Corrosion severity can thus be quantified by correlating particulate accumulation with resonant peak wavelength displacement.

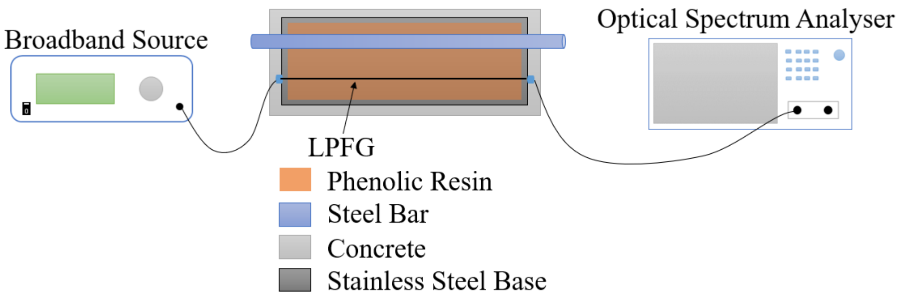


Figure 2-9 LPFG-based corrosion sensor in Liu's research

An alternative approach involved Fe-C coated LPFG sensors for mass-loss measurement during corrosion. Given that Fe-C coatings exhibited chemical composition ratios analogous to steel reinforcement bars in concrete, their degradation can serve as a proxy for rebar corrosion when integrated with LPFG sensors.

Figure 2-10 shows methodology systematically investigated by Huang (Huang et al. 2013; Huang et al. 2014), Chen (Chen et al. 2016), Tang (Tang et al. 2018; Tang et al. 2019), Guo (Guo et al. 2020; Guo et al. 2019). Huang (Huang et al. 2013; Huang et al. 2014) functionalized LPFG sensors with nano iron/silica particles and polyurethane as a LPFG-based sensor for monitoring corrosion. Then based on this sensor, Huang established a correlation between steel bar corrosion and coating degradation. Chen (Chen et al. 2016) advanced the design by depositing a 0.8 μm silver layer followed by electroplating a 20 μm Fe-C coating, achieving enhanced accuracy in detecting corrosion-induced wavelength shifts during NaCl immersion tests. Guo (Guo et al. 2020; Guo et al. 2019) further improved sensor durability by integrating a graphene/silver nanowire (Gr/AgNW) composite, which increased sensitivity and service life by over 90% and 110%, respectively, compared to conventional silver coatings. The Fe-C coated LPFG sensor has shown high sensitivity and great potential in corrosion process of steel rebar, especially in initial corrosion stages.

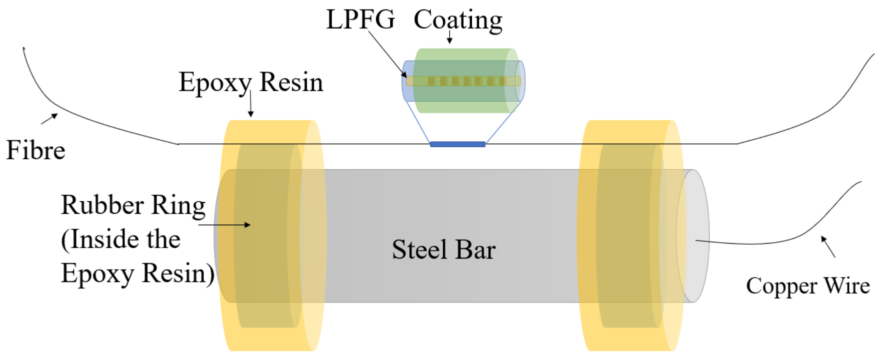


Figure 2-10 Schematic of Fe-C coated LPFG-based sensor for monitoring corrosion

*2.1.3.6 LPFG-based sensors for monitoring pH*

Traditional pH measurements include chemical indicators, in-situ leaching method (Taheri 2019) are inherently destructive. LPFG-based sensors for monitoring pH enable in situ and non-destructive monitoring of pH levels. Hydrophilic hydrogel coatings, which exhibit pH-dependent swelling behavior, have been widely employed in LPFG-based sensors for monitoring pH due to their reversible RI modulation in response to ambient acidity. Table 2-4 summarizes the performance metrics of LPFG-based sensors for monitoring pH reported in prior studies, highlighting their sensitivity, dynamic range, and response time.

Table 2-4 Summary of current LPFG-based sensors for monitoring pH

| **Author** | **Coating** | **Range** | **Response time** | **Sensitivity** |
|---|---|---|---|---|
| (Corres, Matias, et al. 2007) | PB in the PAH/PAA | 4-7 | 60s | 28.3 nm/pH |
| (Mishra et al. 2017) | Hydrogel | 2-12 | 2s | 0.66 nm/pH |
| (Corres, Del Villar, et al. 2007) | Hydrochloride and polyacrylic acid | 4-7 | 120s | 28.3 nm/pH |

| | | | | |
|---|---|---|---|---|
| (Ni et al. 2019) | Polyelectrolytes-wrapped multi-walled carbon nanotubes | 2-13 | - | 0.83 dB/pH |

*2.1.3.7 Summary on LPFG-based sensors for monitoring chemical parameters*

LPFG sensors exhibit sensitivity to a range of critical parameters, encompassing relative humidity, pH, and corrosion inside concrete. The successful integration of LPFG-based sensors for monitoring chemical parameters hinges on meticulous installation practices and robust mechanical protection measures. It is essential to evaluate the sensing efficiency of LPFG-based sensors embedded in concrete.

### 2.1.4 SPR-based sensors for monitoring chemical parameters

SPR refers to the resonant oscillation of conduction electrons at the interface between negative and positive permittivity material stimulated induced by incident light. In fiber cables, light propagates via total internal reflection. Consequently, the SPR principle associated with prism coupling can be adapted to optical fiber configurations (Zhao et al. 2018). This coupling generates a resonant trough in the reflected light intensity, which exhibits sensitivity to changes in the RI (Hu et al. 2016). Jorgenson (Jorgenson et al. 1993) proposed a fiber optic sensor for monitoring chemical parameters based on SPR for the first time in 1992. This theory is the sensing principle of both single-mode-multimode-single-mode (SMS) sensor and multimode-single-mode-multimode (MSM) sensor.

*2.1.4.1 Sensing principle of SPR-based sensors*

The SMS structure is a widely utilized SPR-based sensor configuration. It is fabricated by splicing a segment of multimode fiber (MMF) between two single-mode fibers (SMFs) (see Figure 2-11). Light propagating through the input SMF enters the MMF section, exciting guided modes within the MMF. These modes propagate along the fiber and subsequently re-couple into the output SMF core. Since the longitudinal propagation constants of the excited modes depend on the cladding RI of the MMF, variations in the RI directly modulate the transmission spectrum (Hu et al. 2015).

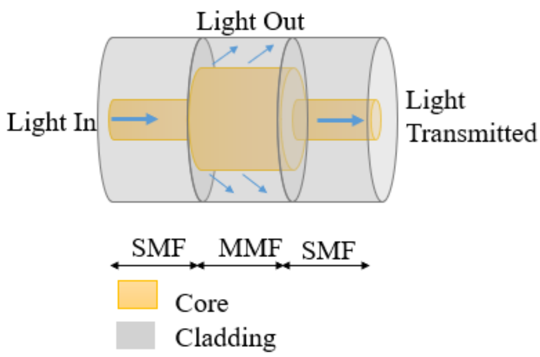


Figure 2-11 Schematic of a SMS structure

MSM structure refers to multimode-single-mode-multimode structure. The MSM structure comprises an SMF spliced between two MMFs (see Figure 2-12). When light transitions from the MMF to the SMF, a portion of the optical power couples from the MMF core to the SMF cladding. Similar to the SMS structure, this coupling produces a resonant trough in the spectrum, the position and depth of which vary with changes in the RI.

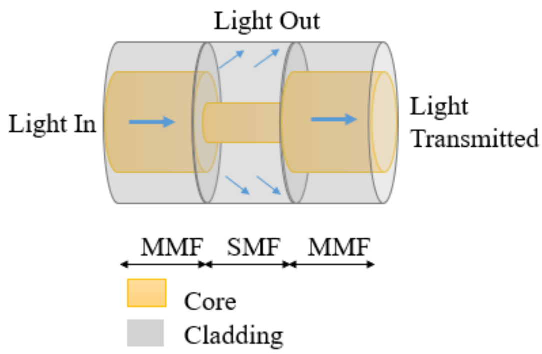


Figure 2-12 Schematic of an MSM structure

*2.1.4.2 Fabrication of SPR-based sensors*

The fabrication process for the SMS structure involves three primary steps: (1) stripping the cladding of the SMF, (2) cleaving the MMF to a predetermined length, and (3) splicing the fibers using a fusion splicer (Zhao et al. 2014). The MSM structure is fabricated using an identical procedure.

*2.1.4.3 SPR-based sensors for monitoring relative humidity*

Various structural modifications of SMS fiber-optic configurations have been explored to enhance sensitivity. Multiple studies An (An et al. 2014), Wang (Wang et al. 2017), Xu (Xu et al. 2017), Lin (Lin et al. 2020) have demonstrated advancements in SMS-based sensors for monitoring RH through innovative structural designs. Figure 2-13(a) shows SMS-based sensor developed by An (An et al. 2014) with two waist-enlarged tapers. The sensitivity of the sensor was 0.223 nm / 1%RH. Figure 2-13(b) shows the side polished SMS-based sensor for monitoring relative humidity designed by Wang (Wang et al. 2017). This sensor was fabricated by a rolling wheel coated with abrasive paper. The sensitivity of this sensor was 0.14 dB / 1%RH. Further optimization was reported by Lin (Lin et al. 2020). Lin designed a spiral micro-structured SMS structure. Then coated the structure with PVA. RH sensitivity of the sensor was 0.650 nm/ 1%RH.

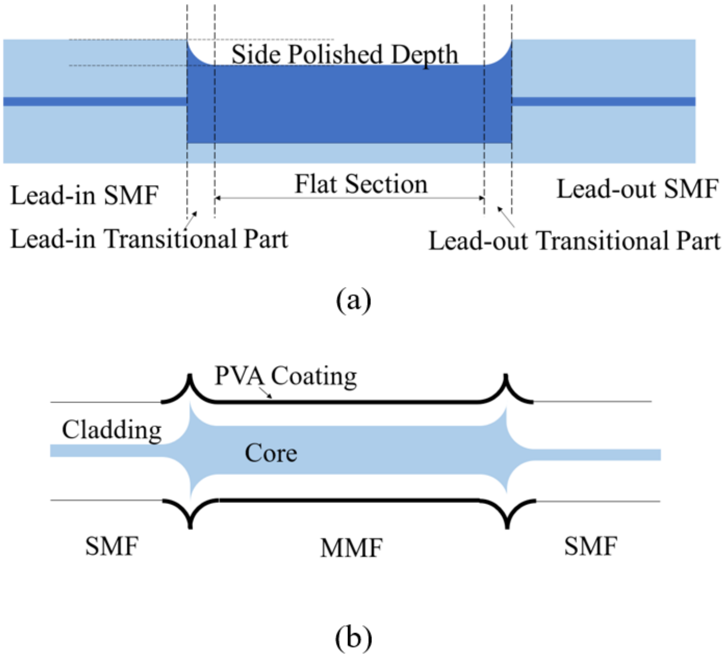


Figure 2-13 Schematic of SPR-based relative humidity sensors

*2.1.4.4 SPR-based sensors for monitoring pH*

pH-sensitive hydrogel coatings have been extensively employed in SPR-based sensors for monitoring pH due to their ability to provide in-situ and non-destructive monitoring of pH levels. Table 2-5 summarizes the performance metrics of SPR-based sensors for monitoring pH reported in previous studies.

Table 2-5 Summary of current SPR-based sensors for monitoring pH

| Author | Coating | Range | Response time | Sensitivity |
|---|---|---|---|---|
| (Tou et al. 2014) | pH responsive poly hydrogel | 6.75-8.25 | 55s | 1.71 nm/pH |
| (Li et al. 2013) | Precursor TEOS and pH-sensitive indicators | 1-13 | 40s | 0.6 dBm/pH |
| (Zhao et al. 2018) | Hydrogel | 1-12 | 24s | 13 nm/pH |

#### *2.1.4.5 Summary on SPR-based sensors for monitoring chemical parameters*

While SPR sensors have demonstrated remarkable advantages in biological study, their utilization within civil engineering field, particularly in monitoring chemical parameters inside concrete, remains significantly underexplored. A primary impediment hindering the broader application of SPR sensors in this field is the intricate fabrication process involved. The complexity of these sensor structures not only complicates standardized production methods but also contributes to elevated costs, posing a significant challenge to their widespread integration in concrete durability monitoring applications.

### 2.1.5 Fluorescence-based sensors for monitoring chemical parameters

#### *2.1.5.1 Sensing principle of fluorescence-based sensor*

Fluorescence-based sensor is a simple yet effective tool for monitoring chemical parameters because of the explicit working principle and capacity of on-site and real-time monitoring (Wen et al. 2019). Fluorescence-based sensors are based on the intensity change caused by the fluorescence or quenching phenomenon of the fluorescent material inside the sensor probe. Commonly employed fluorescent materials in such sensors include high-molecular-weight organic fluorophores, fluorescent dyes, and semiconductor quantum dots, whose emission properties reversibly shift in response to environmental changes (Lin et al. 2019).

Figure 2-14 shows a schematic of a typical fluorescence-based sensor. The system includes four parts: a laser source, an optical spectrometer, a Y-type coupler, and a probe consisting of fluorescent material. The laser controller modulates the intensity of the emitted light, which excites the fluorescent material in the detector. Laser source, spectrometer, and detector are connected by Y-type fiber to monitor the wavelength change of fluorescence (Huang et al. 2021).

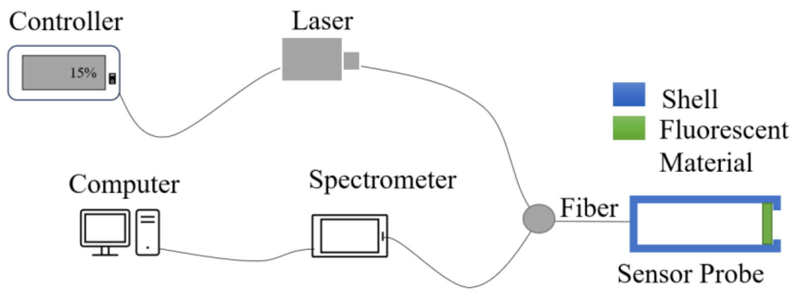


Figure 2-14 Schematic of a fluorescence-based sensor

*2.1.5.2 Principle of fluorescence*

Fluorescence is the light emitted by an atom or molecule after the absorption of electromagnetic energy. The transition from the excited species' first excited electronic singlet level to its ground electronic level will cause fluorescence.

The singlet electronic states are denoted by $S_0$ (fundamental electronic state), $S_1$, $S_2$, and so on. The vertical arrows corresponding to absorption start from the 0 (lowest) vibrational energy level of $S_0$ because most molecules are at this level at room temperature. Vibrational levels are associated with each electronic state. Absorption of a photon can bring a molecule to one of the vibrational levels of $S_1$, $S_2$ and so on. Emission of photons accompanying the electronic states from $S_1$ to $S_0$ is called fluorescence (Figure 2-15). Most fluorescence emission occurs from $S_1$ and therefore its characteristics do not depend on the excitation wavelength. The fluorescence characteristics are strongly dependent on the nature and the chemical structure of emitting species (Valeur et al. 2012). Structural effects include the effects of the molecular structure of organic molecules, the effects of the conjugated polymer, the effects of carbon nanostructure, the effects of metal compounds, and the effects of semiconductor nanocrystals.

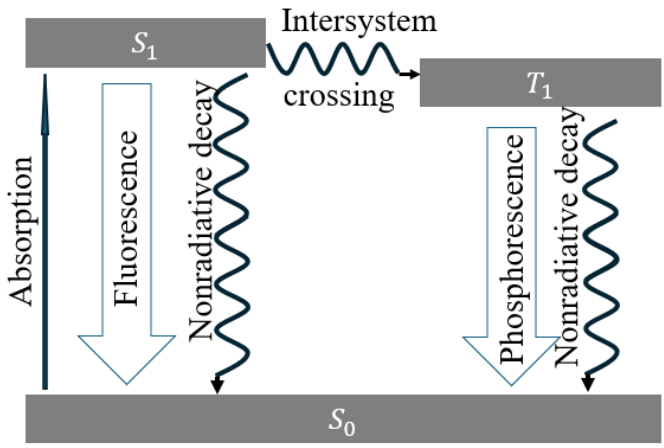


Figure 2-15 Emission of photons accompanying the electronic states (Valeur et al. 2012)

*2.1.5.3 Principle of quenching*

The theory of fluorescence quenching dates to the work of Stern & Volmer on the decay time of fluorescence. They suggested a model to mathematically describe the quenching of fluorescence intensity and lifetime as a function of the target analyte concentration. In terms of fluorescence, the lifetime accounts for the time an electron spends in $S_1$ (the excited singlet state with the lowest energy) before it returns $S_0$ (the ground state) to by the emission of a photon. In their model, Stern & Volmer differentiated between dynamic and static quenching (Bolse et al. 2018).

Dynamic quenching is based on collisional events between a fluorophore and a target analyte. These events can trigger the non-radiative deactivation of excited states if the target is able to diffuse to the fluorophore within the lifetime of the excited states. The mechanism is called collisional quenching as well (Bolse et al. 2018). For a continuous fluorescence excited by a constant fluorescence, the concentration of excited states in the absence of a target is constant according to:

$$\frac{d[n^*]}{dt} = f(t) - \gamma_0[n^*]_0 = 0 \tag{2-4}$$

where $\frac{d[n^*]}{dt}$ is the change of the concentration of excited states in the fluorophore over time, $f(t)$ is the time-dependent function of the fluorescence excitation, $\gamma_0$ is the sum of the non-radiative and the radiative decay rates of the fluorophore $[n^*]_0$ is the initial concentration of excited states in the fluorophore (Bolse et al. 2018). In the presence of a target, Stern and Volmer made the empirical assumption that the nonradiative decay rate is only affected by the contribution of the quenching as:

$$\frac{d[n^*]}{dt} = f(t) - (\gamma_0 + k_q[Q])[n^*]_0 = 0 \tag{2-5}$$

where $k_q$ is the bimolecular quenching constant and $[Q]$ is the target concentration.

$$\frac{[n^*]_0}{[n^*]} = 1 + \frac{k_q}{\gamma_0}[Q] \tag{2-6}$$

The Stern-Volmer equation for dynamic quenching in its most common form can then be derived from the assumption that the fluorescence intensity is directly proportional to the concentration of excited electronic states in the fluorophore such that:

$$\frac{I_0}{I} = 1 + \frac{k_q}{\gamma_0}[Q] = 1 + K_D[Q] \tag{2-7}$$

$I_0$ is the fluorescence intensity in the absence of the target, $I$ is the fluorescence intensity and $K_D$ is the Stern-Volmer constant for dynamic quenching. From another perspective, the fluorescence intensity ratio can be expressed as a ratio of fluorescence lifetimes because the kinetic deactivation of excited states reduces the lifetime in the same manner (Bolse et al. 2018). Mathematically, this is expressed by utilizing the reciprocal decay rates $\tau_0 = \gamma_0^{-1}$ and $\tau = (\gamma_0 + k_q[Q])^{-1}$ such that:

$$\frac{\tau_0}{\tau} = 1 + k_q\tau_0[Q] = 1 + K_D[Q] = \frac{I_0}{I} \tag{2-8}$$

Static quenching assumes that a fluorophore and a target can form a non-fluorescent complex. The Stern-Volmer equation for static quenching can be derived from the association constant for the complex formation in the presence of the target, defined by:

$$K_s = \frac{[n^* - Q]}{[n^*][Q]} \tag{2-9}$$

where $K_s$ is the Stern-Volmer constant for static quenching, $[n^* - Q]$ is the concentration of nonfluorescent complexes, $[n^*]$ is the remaining fluorophore concentration and $[Q]$ is the target concentration. Because the concentration of excited states is constant in the fluorophore due to constant fluorescence excitation, the total fluorophore concentration in the absence of the target is given by:

$$[n^*]_0 = [n^*] + [n^* - Q] \tag{2-10}$$

A rearrangement led to the Stern-Volmer equation for static quenching:

$$\frac{I_0}{I} = 1 + K_s[Q] \quad (2\text{-}11)$$

It is important to note that the fluorescence intensity ratio is not equal to the fluorescence lifetime ratio in the case of static quenching. Here, the observed fluorescence in a quenched state results from uncompleted fluorophores that do not interact with the target. Thus, the decay rates are not affected such that:

$$\frac{I_0}{I} \neq \frac{\tau_0}{\tau} = 1 \quad (2\text{-}12)$$

Measurements deviate from the linear relationship between the quenching of fluorescence and the target concentration if both dynamic and static mechanisms are present. This is called combined quenching. The observed fluorescence quenching would follow the multiplication:

$$\frac{I_0}{I} = (1 + K_D[Q])(1 + K_s[Q]) \quad (2\text{-}13)$$

*2.1.5.4 Fluorescence-based pH sensors*

In prior studies, the majority of experimental setups adopted configurations analogous to the setup depicted in Figure 2-14. A significant number of pH-sensitive fluorescent materials or sensors were optimized for operation within physiological or near-neutral pH ranges (Chao et al. 2017; Ma et al. 2017; Moradi et al. 2019; Gong et al. 2020; Jiang et al. 2013; Adachi et al. 2015; Duong et al. 2006; Derinkuyu et al. 2007) which might not be suitable for the monitoring of concrete durability. As shown in Table 2-6, most pH sensitive fluorescent materials utilized in the previous research are limited in sensing pH range. To address this limitation, subsequent research has focused on developing fluorescence-based pH sensors capable of operating within the pH range of 10-13. As summarized in Table 2-7, azo-dye (Blumentritt et al. 2008), thymol blue (Bartelmess et al. 2020), and coumarin imidazole dye (Nguyen et al. 2014) and Naphth-AlkyneOMe (Tariq et al. 2021) were applied to monitoring pH from 10 to 13. Among these materials, coumarin imidazole dye had the most suitable measuring range.

Table 2-6 Summary of current pH sensitive fluorescent materials

| **Author** | **Material** | **Range** |
|---|---|---|
| (Chao et al. 2017) | Pyrene structure attached to methoxypyridine | 1.26-3.97 and 8.54-10.36 |
| (Ma et al. 2017) | Two water-stable 2-D zinc(II) compounds | 7-11 |
| (Adachi et al. 2015) | Conjugated polymers containing pyridine rings | 1-7 |
| (Moradi et al. 2019) | Hydroxypyrene- 1,3,6-trisulfonic acid trisodium salt (HPTS) | 5.7-9.0 and 4.2-5.7 and 3.4-4.2 |
| (Gong et al. 2020) | 5(6)-FAM and Porphyrin | 5.5-8.0 |
| (Jiang et al. 2013) | Porphyrinic Zr metal−organic framework | 1-11 |
| (Duong et al. 2006) | Fluoresceinamine isomer II (FA) | 4-10 |
| (Derinkuyu et al. 2007) | Chloro phenyl imino propenyl aniline (CPIPA) and nitro phenyl imino propenyl aniline (NPIPA) | 8-12 and 7-12 |

Table 2-7 Summary of current fluorescence-based sensors for monitoring pH

| **Author** | **Coating** | **Range** |
|---|---|---|
| (Blumentritt et al. 2008) | Azo-dye | 10.4-12.24 |
| (Bartelmess et al. 2020) | Thymol blue | 11-13 |
| (Nguyen et al. 2014) | Coumarin imidazole dye | 10-13.2 |
| (Tariq et al. 2021) | Naphth-AlkyneOMe entrapped in a cross-linked polyvinyl alcohol-glutaraldehyde matrix | 10.5-12.5 |

*2.1.5.5 Summary on fluorescence-based sensors for monitoring chemical parameters*

The research of fluorescence-based sensors for monitoring chemical parameters is still on-going. Despite the potential benefits they offer, the broader application of fluorescence-based sensors in concrete faces several significant challenges. The service life of fluorescence-based sensors is constrained by the relatively short lifespan of fluorescence materials, potentially compromising their ability to meet the demands of the long-term concrete durability monitoring. However, the advantages of fiber optic sensors (FOSs) including immunity to corrosion, remote sensing and signal transmission for long distances make this technique a very promising method. With enhancements in the sensing range and improvements in service longevity, fluorescence-based sensors hold the potential for widespread deployment in concrete structure health monitoring.

### 2.1.6 Distributed fiber optic sensors for monitoring chemical parameters

*2.1.6.1 Sensing principle of distributed fiber optic sensos*

The sensing principle of the distributed fiber optic sensors involves transmitting a laser pulse through an optical fiber cable and detecting the reflected or backscattered light. There are three types of backscattering used for measurement including Raman, Brillouin, and Rayleigh (Davis et al. 2017).

Raman backscattering is widely used in distributed temperature sensing (DTS). A DTS instrument sends a short laser pulse along a fiber optic cable. Then the detector measures the laser scattered back in the fiber cable. Most backscatters have the same wavelength as the original laser pulse. Other backscatters show the effect of Raman backscattering. The DTS instrument measures the intensity of these backscatters: Stokes scatter and anti-Stokes scatter. Stokes scatter has a longer wavelength compared to anti-Stokes scatter. Critically, the intensity of anti-Stokes scattering is temperature-dependent, enabling precise thermal measurements (des Tombe et al. 2020).

Brillouin scattering arises from interactions between propagating light and density fluctuations in the optical medium. Two common sensing techniques leveraging this phenomenon are Brillouin optical time domain reflectometry (BOTDR) and Brillouin optical time domain analysis (BOTDA) (Hong et al. 2017).

BOTDR employs single-ended fiber access and relies on spontaneous Brillouin scattering (SpBS). When an incident light propagates forward, it will produce spontaneous Brillouin backscattered light along the fiber (see Figure 2-16). The change of pressure, temperature and strain along the optical fiber cable will caused linearly change of the frequency of the back scattered light changes (Hong et al. 2017; Tang, Zhou, et al. 2021).

BOTDA is a more complicated setup of BOTDR. It is based on the Stimulated Brillouin Scattering (SBS) effect. Figure 2-17 shows the setup of the BOTDA. A pulsed pump wave and a continuous probe wave are injected into opposite ends of the fiber. SBS occurs when the frequency difference between the two waves matches the local Brillouin frequency, amplifying the scattering process. The resulting Brillouin gain spectrum exhibits a frequency shift sensitive to temperature and strain variations (Hong et al. 2017).

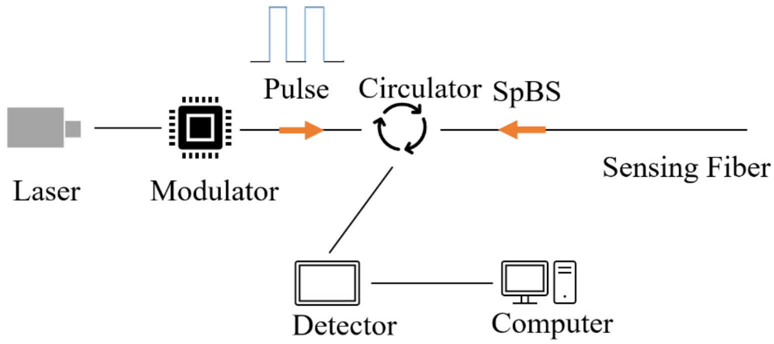


Figure 2-16 Schematic of BOTDR

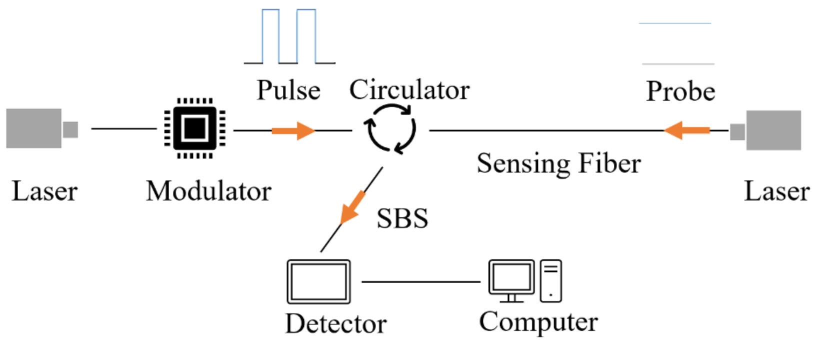


Figure 2-17 Schematic of BOTDA

Optical frequency domain reflectometry (OFDR) operates based on Rayleigh backscattering. This phenomenon is caused by the interactions between the fluctuations in the density of the fiber optic core and the light. Changes in temperature or strain induce expansion or contraction of the fiber, altering the spacing between intrinsic imperfections. This modulates the frequency of backscattered light, enabling high-resolution distributed sensing (Regier et al. 2015).

*2.1.6.2 Distributed fiber optic sensors for monitoring corrosion*

Distributed Fiber Optic Sensor (DFOS) enable continuous monitoring along the entire length of an optical fiber cable, rendering this technology particularly suitable for corrosion detection in extended structures (Fan et al. 2020). In numerous studies, distributed sensors have been employed to monitor corrosion in steel reinforcement bars, predominantly by detecting strain variations induced by the volumetric expansion of corrosion products.

Brillouin backscattering-based sensors for monitoring corrosion are installed mainly in two methods. Figure 2-18 shows the first method is to install a single-mode fiber optic cable tightly around a steel bar (Zhao et al. 2011; Lv et al. 2017). Figure 2-19 shows the other method is to install the fiber optic cable along the steel bar (Fan et al. 2018). Both schematics monitor the strain changes caused by the volume expansion of the corrosion product.

Pulse-pre-pump BOTDA (PPP-BOTDA) technology was applied with higher spatial resolution (Fan et al. 2020; Fan et al. 2018). The special resolution increased from one meter (Zhao et al. 2011) to two centimeters (Fan et al. 2018).

Even though DFOS is a promising method for corrosion monitoring since it can provide corrosion-induced strain over long distances, the monitoring results may be coupled with the mechanical strain caused by external loads.

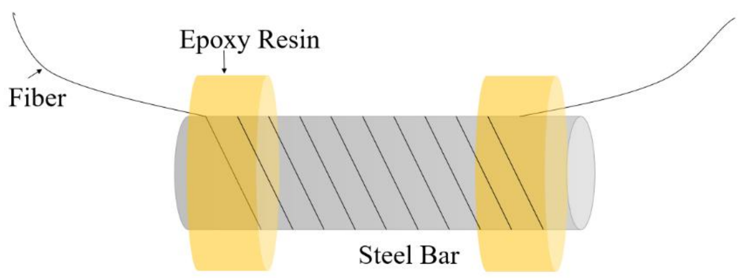


Figure 2-18 Schematic of distributed fiber optic sensors for monitoring corrosion (1)

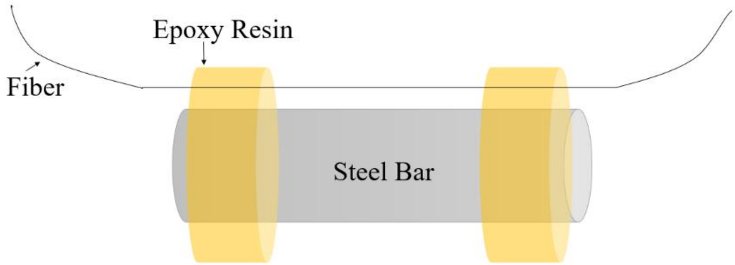


Figure 2-19 Schematic of distributed fiber optic sensors for monitoring corrosion (2)

Apart from Brillouin backscattering, OFDR is another widely used distributed fiber optic sensing technology used in monitoring corrosion. The OFDR technology is applied close to the setup of Brillouin backscattering sensor in monitoring corrosion (Tang, Zhao, et al. 2021; Brault et al. 2019).

*2.1.6.3 Summary on distributed fiber optic sensors for monitoring chemical parameters*

DFOS provides a distinct advantage by enabling continuous strain measurement along the entire length of a fiber optic cable, thereby facilitating holistic structural health monitoring of large-scale infrastructure. The sensitivity and monitoring range can be increased with the optimization of the transfer coefficient. By fine-tuning this transfer coefficient, it becomes possible to amplify the sensor's sensitivity to subtle structural changes and broaden its monitoring capabilities, thereby empowering more accurate and comprehensive assessments of structural integrity and durability over time.

## 2.2 Machine Learning Aided Fiber Optic Sensing System Data Analysis

### 2.2.1 Introduction

Artificial intelligence is a technology that simulates human intelligence and aims to create computer systems capable of performing complex tasks, reasoning, and learning. Machine Learning (ML) is a subset of artificial intelligence, and it enables systems to learn patterns from data without explicit programming. It can simulate and predict target variables by deriving the relationship between input variables and target variables from large data sets. Key machine learning paradigms include supervised learning, unsupervised learning and reinforcement learning.

Supervised learning is a machine learning paradigm that maps input variables to corresponding output variables, requiring manual data labeling. This approach is analogous to a structured educational environment in which an instructor provides explicit guidance to learners, ensuring alignment between inputs and desired outputs. Models developed through supervised learning are purpose-built for specific tasks and depend on extensive manually annotated datasets. These datasets are typically partitioned into three distinct subsets: training data (for model development), testing data (for performance evaluation), and validation data (for hyperparameter tuning) (Alloghani et al. 2020). Supervised learning is commonly used in regression (multinomial regression, nonlinear regression, neural networks, ensemble methods, decision trees, metric learning) and classification (support vector machines, K-nearest neighbor, Bayesian method, Bayesian belief networks, principal component analysis, linear discriminant analysis, decision trees, neural networks, ensemble methods, deep learning, metric learning, manifold learning, collaborative filtering) (Salehi et al. 2018).

Unsupervised learning is a machine learning paradigm focused on identifying inherent patterns within unlabeled datasets without requiring manual annotation. This approach employs techniques such as clustering to enable algorithmic analysis of raw data, operating autonomously rather than relying on predefined labels or human guidance. The process involves training systems to discern latent structures, such as similarities, disparities, or recurrent patterns, directly from unstructured input data. By organizing unannotated information into meaningful groups or categories, unsupervised learning algorithms autonomously infer relationships and classifications absent explicit supervision. This self-organizing capability makes it particularly valuable for exploration data analysis, where the objective is to uncover hidden trends or intrinsic data hierarchies without prior knowledge of outcomes (Alloghani et al. 2020). Unsupervised learning is widely used in clustering (hierarchical clustering, partitional clustering, K-means, spectral clustering, hidden Markov model, Gaussian mixture, Graph theory) (Salehi et al. 2018).

Reinforcement learning (RL) involves an autonomous agent learning optimal decision-making strategies through trial-and-error interactions with an environment. Unlike other approaches, RL utilizes feedback in the form of rewards (positive reinforcement) or penalties (negative reinforcement) to iteratively refine the agent's behavior. This paradigm is widely employed to identify context-specific solutions that maximize cumulative long-term rewards (Goyal et al. 2018). Reinforcement learning is widely used in Agent-based models ( Markov decision processes, temporal difference learning, dynamic programming, deep reinforcement learning, Ad-Hoc techniques, Direct policy search) (Salehi et al. 2018).

The three core paradigms, supervised, unsupervised, and reinforcement learning address distinct challenges and applications. Together, these paradigms underscore the versatility of machine learning, catering to scenarios ranging from well-defined predictive tasks to open-ended discovery and autonomous problem-solving.

### 2.2.2 Machine learning aided fiber optic multiparametric sensing system data analysis

Cross sensitivity presents a significant challenge for fiber optic sensing system data analysis. To address this, ML paradigms are being developed for multiparameter sensing system data analysis. These ML paradigms aim to isolate the influence of individual physical parameters on sensor signals and enable simultaneous prediction of multiple parameters. For instance, recent research utilized the sidelobes of FBG spectra to differentiate strain from temperature effects (Sarkar, Tarhani, et al. 2020). Then, Sarkar (Sarkar, Inupakutika, et al. 2020) employed a random forest model to predict both strain and temperature.

This cross-sensitivity issue is particularly critical for advancing fiber optic sensing system data analysis. Fiber optic sensing systems including direct spectroscopic interrogation of the chemical environment and indirect interrogation via a sensing medium can be enhanced through ML. Methods producing discrete spectral lines (e.g., LIBS, Raman, FTIR) directly identify chemical species. Here, ML primarily enhances detection limits or simplifies complex spectra using dimensionality reduction techniques like Principal Component Analysis (PCA). PCA reduces complex spectral data to key features correlated with process variables, such as monitoring beef coloration during cooking using spectral data and techniques like PCA or ANNs (Lewis et al. 2007). Dyes with distinct optical absorption features are also effective. Porphyrin films on fibers, showing specific visible absorption peaks, function as versatile gas sensors. PCA helps classify sensor states for these, like measuring ammonia under varying humidity (Korposh et al. 2018).

The fiber optic sensing system offers rugged stability for harsh environments. Recent work on high temperature stable oxides shows advantages of ML integration. These materials sense gases via mechanisms like free carrier absorption (Near InfraRed (NIR)), plasmonic (visible/NIR), or interbond absorption (UV), where environmental variables cause subtle, cross-sensitive spectral changes. For instance, different reducing gases subtly affect charge carrier density and mobility in oxides like ITO or LSTO, shaping NIR absorption (Jee et al. 2018).

These works show the importance of using ML algorithms as new tools for fiber optic multiparameter sensing system data analysis. ML aided solution phase multiparameter sensing (e.g., pH) is less explored compared to gases, and needs more research.

### 2.2.3 Machine learning aided accelerated fiber optic sensing system data analysis

Fiber optic sensing system generates huge amounts of data during operation especially BOTDA sensing system. Nonlinear curve-fitting and supervised ML are two commonly used methods to accelerate data analysis.

For instance, Zhang (Zhang et al. 2013) developed a radial basis function neural network (RBFNN) for BOTDR, accelerating data analysis while maintaining BFS precision. It outperformed traditional methods (Levenberg-Marquardt, cubic spline, polynomial fitting) by operating independently of signal knowledge, offering speed, stability, reliability, and precision. Wu (Wu et al. 2017) used a support vector machine (SVM) to achieve a 100-times speed increase over conventional techniques. Wang (Wang et al. 2019) applied deep neural networks (DNN) to a 25 km LEAF fiber, reducing data analysis time from 5656 seconds to just 1.6 seconds. Azad (Azad et al. 2016) employed artificial neural networks (ANN) on a 41km BOTDA system, reducing required data points and mitigating Brillouin linewidth effects on accuracy.

Despite these speed gains, machine learning aided accelerated fiber optic sensing system data analysis face challenges like overfitting and deterministic inversion, lacking prediction confidence intervals.

### 2.2.4 Machine learning aided anomaly detection in fiber optic sensing system data analysis

Pattern recognition algorithms fundamentally aim to automatically identify patterns within data from fiber optic sensing system using machine learning, enabling critical information extraction for rapid decision-making, and prediction of concerned parameters.

Grant Jacob (Grant Jacob et al. 2019) presented a remote fiber-coupled method for particle classification via backscattered light analysis, achieving 97% real-time accuracy in identifying pollen grains using a neural network. Lipski (Lipski 2020) combined 3D printed flexible sensors with FBG arrays and a pattern recognition algorithm to capture complex strain profiles for SHM. This sensor used miniaturized cylindrical shells with coiled FBGs, and spatial strain variations were derived using a threshold-based algorithm informed by nonlinear finite analysis simulations. To address noise and instability in FBG signals (e.g., environmental factors, aging), a denoising technique integrated with a long short-term memory (LSTM) algorithm was proposed for intensity wavelength division multiplexed FBG networks. This model learned spectral reflection features at different strains, forming a sensing signal model capable of discriminating against overlapping strain signals (Manie et al. 2020).

Integrating fiber optic sensing system with machine learning enables real-time SHM and automated failure detection in concrete infrastructure. Kowarik (Kowarik et al. 2020) used a commercial Helios distributed acoustic sensor (DAS) for real-time train monitoring. An ANN processed the DAS data significantly faster than conventional filtering and peak finding. Che (Che et al. 2019) experimentally verified human movement detection and pipeline corrosion monitoring using a neural network DAS system enhanced by FBGs. ANNs classified corrosion by identifying hammer impacts (aluminum, rubber, plastic, steel) with 94.29% accuracy.

While the trained models showed excellent accuracy on specific data sets, factors such as test coupons, testing environment and so on would influence the accuracy of trained models. More generic models require further development.

### 2.2.5 Machine learning aided data generation for fiber optic sensing system data analysis

Training effective ML model faces a significant challenge: the need for extensive, labeled datasets capturing specific events. While large public datasets have enabled strong performance in image and audio tasks, this data abundance is lacking for fiber optic sensing system data analysis. For instance, machine learning applications in fiber optic sensing system data analysis for acoustic event classification have been limited by small training sets (around 4000 samples) (Shi et al. 2019). Compounding this issue, standard image augmentation techniques (e.g., rotation) are unsuitable for FOS feature maps. Consequently, generating synthetic FOS data representing target acoustic events is a crucial research focus. For instance, a Spatiotemporal Convolutional Neural Networks (ST-CNN) framework combined simulated images with real DAS data to create realistic synthetic datasets for vibrational events (Lea et al. 2016). A recent work has explored multi-physics simulation. Tools modeling rock physics, fluid flow, and wave propagation have generated synthetic DAS data for classification of oil/water (Pereira et al. 2021).

Further research should prioritize Physics-Informed Machine Learning (PIML), including frameworks like Physics-Informed Neural Networks (PINNs). These tools can leverage both domain knowledge and sensor data to develop novel data analysis models.

## 2.3 Summary

Among emerging sensing technologies, fiber optic sensing systems have demonstrated considerable potential in monitoring chemical parameters. Chemical parameters, particularly those influencing concrete durability, have gained recognition as critical determinants of long-term performance and degradation mechanisms. Sulphate and chloride attacks, along with high humidity, critically undermine concrete durability through chemical reactions and electrochemical processes. In recent years, fiber optic sensing systems for monitoring chemical parameters have emerged as a pivotal advancement in laboratories. The previous research of fiber optic sensing systems shows the great possibility of using fiber optic sensing systems to monitor chemical parameters inside the concrete.

From previous research, we can find FBG sensors, LPFG sensors, SPR sensors, distributed sensors and fluorescence-based sensors are able to monitor chemical parameters like relative humidity, corrosion, pH and so on. With challenges like limited durability and elevated manufacturing expenses, these fiber optic sensing systems for monitoring chemical parameters are not applied widely in the field. As research efforts intensify and technology advances, there is a growing realization that fiber optic sensing systems for monitoring chemical parameters inside concrete hold the potential to significantly enhance the scope and efficacy to address deterioration.

In fiber optic sensing system data analysis, ML has emerged as a transformative force, offering innovative solutions that transcend the limitations of traditional inspection methods. By leveraging supervised, unsupervised, and reinforcement learning paradigms, ML algorithms such as ANNs, SVMs, and PCA have demonstrated exceptional capability in detecting structural anomalies, optimizing infrastructure design, and predicting long-term performance under dynamic environmental and operational conditions. Applications span diverse domains, from wind turbine blade diagnostics (Dervilis 2013) and reinforced concrete structure monitoring (Butcher et al. 2014) to bridge health assessment (Neves et al. 2017).

The application of supervised, unsupervised, and reinforcement learning paradigms provides versatile tools tailored to specific FOS needs. Key advancements include:

Overcoming Cross-Sensitivity: ML algorithms, particularly supervised models like Random Forests, enable robust multiparametric sensing by isolating and predicting individual physical parameters (e.g., strain and temperature) from complex, cross-sensitive spectral data.

Accelerating Dara Analysis: ML techniques, especially Neural Networks (RBFNN, DNN, ANN) and SVM, dramatically accelerate the processing of massive FOS datasets (e.g., from BOTDA/BOTDR systems), achieving speed improvements of orders of magnitude while maintaining or enhancing precision compared to traditional curve-fitting methods.

Enhancing Anomaly Detection: Pattern recognition algorithms, including CNNs, LSTMs, and ANNs, facilitate real-time SHM and automated failure detection. They enable precise classification of events (e.g., particle types, corrosion impacts, human movement) and strain patterns from complex FOS signals, improving infrastructure monitoring and safety.

Enabling Data Generation: To overcome the scarcity of labelled FOS data, ML-driven synthetic data generation (e.g., using ST-CNN frameworks or multiphysics simulations) is proving crucial for training effective models, particularly for acoustic event classification.

While significant progress has been made, challenges remain, such as model overfitting, the need for confidence intervals in predictions, and the relative under-exploration of ML for solution-phase multiparameter sensing. Future research should prioritize exploring Physics-Informed Machine Learning (PIML/PINNs) to integrate deep domain knowledge with data-driven approaches, further enhancing the robustness, interpretability, and generalizability of ML models for fiber optic sensing system data analysis.

Building on prior advancements, this study investigates the feasibility of integrating FBG-based sensing system and fluorescence-based sensing system for monitoring critical chemical parameters inside concrete. Then trains a GP model to analyze the data collected from long-term field test of the developed sensors. Through these innovative works, this thesis paves the way to a more comprehensive monitoring of marine infrastructures deterioration condition and a more accurate prediction of marine infrastructures life-cycle behavior.

# CHAPTER 3. DEVELOPMENT OF AN EMBEDDABLE FBG-BASED SENSING SYSTEM FOR MONITORING RELATIVE HUMIDITY INSIDE CONCRETE AND FIELD VALIDATION

## 3.1 Introduction

The deterioration rate of concrete structures is significantly accelerated under elevated relative humidity conditions (Barroca et al. 2013). Elevated relative humidity within concrete structures will accelerate steel corrosion and carbonation processes (Qiao et al. 2023). Consequently, monitoring relative humidity variations inside the concrete structures during the concrete structure's service life is critical (Bouteiller et al. 2012; Shoukry et al. 2011; Yu et al. 2020).

Existing research has proposed several non-destructive methods for relative humidity monitoring in concrete structures. Among all non-destructive methods for monitoring relative humidity in concrete structures, fiber optic sensing system gained more attention recently over other non-destructive methods due to distinct advantages including lightweight design, compact size, remote and distributed sensing capabilities, and resistance to chemical degradation. These attributes render fiber optic sensing system particularly suitable for long-term structural health monitoring of concrete in harsh environments (Qiao et al. 2023).

In previous research, FBG-based sensors were applied in some field tests. For example, Kahandawa (Kahandawa et al. 2012) uses FBG sensors for structural health monitoring in aerospace fiber reinforced polymer (FRP) structures. The sensor can monitor the exact location of damage. Čápová (Čápová et al. 2020) develops a FBG-based system for strain and temperature monitoring on the newly constructed prestressed-concrete bridge. Ye (Ye et al. 2018) applies a FBG-based stress monitoring system on an orthotropic steel deck arch bridge. Chen (Chen et al. 2020) uses long-gauge FBG to detect damage on vehicle–bridge. These applications of FBG sensors in SHM show that the FBG sensors can operate well in the field if the FBG sensors are properly installed.

However, the application of FBG-based sensing system for monitoring relative humidity inside concrete is rare. To narrow this gap, in this chapter, an FBG-based sensing system for monitoring relative humidity inside the concrete was developed. The sensing system employs two FBGs inscribed on the same optical fiber cable: one coated with polyimide for humidity sensing and the other uncoated for temperature compensation. To further validate the performance of the developed sensing system, the embeddable FBG-based sensing system for monitoring relative humidity inside the concrete was installed in an exposure site.

## 3.2 Experimental Design

The experiments include the development of the FBG-based relative humidity sensor, development of the embeddable FBG-based sensing system for monitoring relative humidity inside the concrete, installation of the system in a concrete beam sample placed in an exposure site, validation of the performance in the field and collection of long-term relative humidity data.

### 3.2.1 Development of an embeddable FBG-based sensor for monitoring relative humidity inside concrete

Figure 3-1 shows the schematic of FBG-based sensor for monitoring relative humidity inside concrete developed in this study. Two FBGs are inscribed into a single fiber. FBG (RH) was coated with polyimide (PI) using a dip-coating machine (see Figure 3-2). FBG (RH) was used for relative humidity sensing. FBG (T) without coating was used for temperature compensation.

Although FBGs lack inherent sensitivity to relative humidity (RH), FBG (RH) is coated with polyimide. The polyimide coating undergoes volumetric changes (swelling/shrinkage) in response to humidity fluctuations, then induces measurable wavelength shifts in the FBG (Kronenberg et al. 2002).

An FBG sensor consists of a periodic modulation of the refractive index in the fiber core, acting as a narrowband filter for incident light. The central wavelength of the reflected light shifts with strain or temperature changes. For a standard FBG sensor, the relationship between the reflected central Bragg wavelength λ shift and strain change Δε and temperature variation ΔT can be stated as:

$$\frac{\Delta\lambda}{\lambda} = \left(1\text{-}p_{eff}\right)\Delta\varepsilon + (\alpha+\xi)\Delta\mathrm{T} \tag{3-1}$$

where $\Delta\lambda$, $p_{eff}$, $\alpha$ and $\xi$ stand for the shift of central wavelength, the photo-elastic parameter related to the fiber property, the thermal expansion coefficient, and the thermal-optic coefficient of fiber core (Hong et al. 2016).

FBG (T) and FBG (RH) have different sensitivities to temperature. FBG (T) is insensitive to humidity changes. Since FBG (T) and FBG (RH) are inscribed into a single fiber, the temperature change of FBG (T) and FBG (RH) are the same. The shift of central wavelength of FBG(RH) are caused by temperature change and relative humidity change. The temperature change of FBG(RH) can be subtracted by themperature change obtained from FBG(T). Thus, the relative humidity can be calculated with the shift of the central wavelength from FBG (T) and FBG (RH).

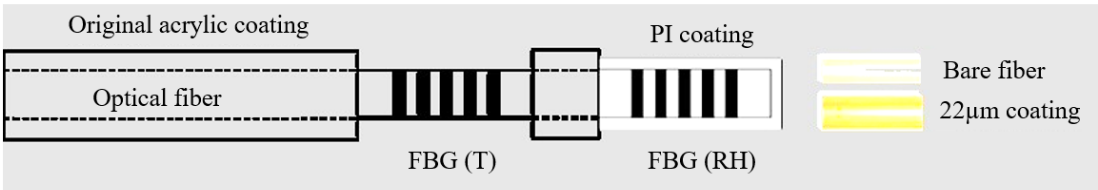


Figure 3-1 Schematic of FBG-based sensor for monitoring relative humidity

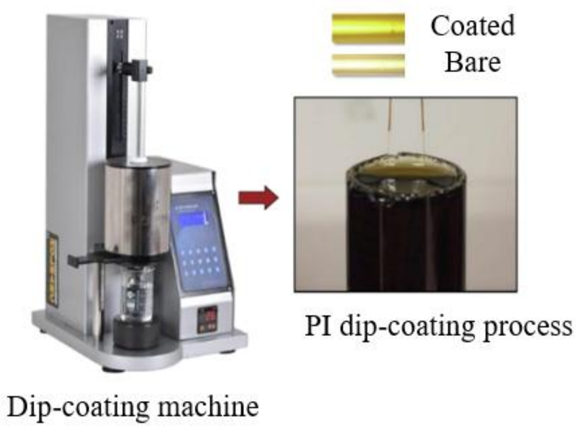


Figure 3-2 Dip-coating process

### 3.2.2 Development of an embeddable FBG-based sensing system for monitoring relative humidity inside concrete

Figure 3-3 shows the schematic of embeddable FBG-based sensing system for monitoring relative humidity inside concrete. The sensing system includes five parts, FBG sensor probes, a connect system, an automatic data collection system, an automatic transmission system and a supporting system.

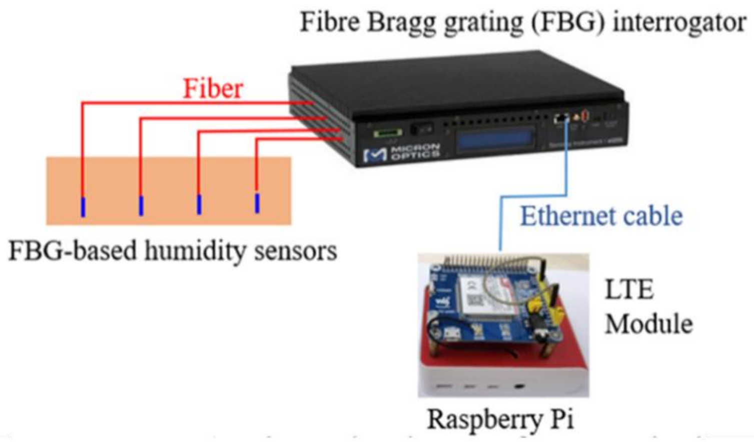


Figure 3-3 Schematic of FBG-based sensing system for monitoring relative humidity

FBG sensor probes: The FBG sensors installed inside the probes are introduced in Chapter 3.2.1. A perforated polyether-ether ketone (PEEK) tube is applied to protect the FBG sensor during the on-site tests (see Figure 3-4).

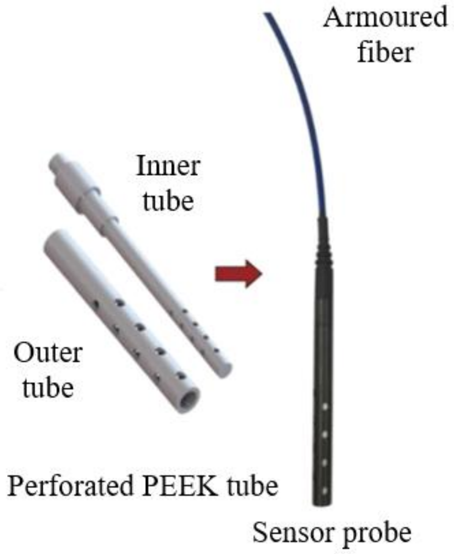


Figure 3-4 FBG sensor probe protected by PEEK tube

Connect system: HAILE GYTA53 steel-tape-armored fiber optic cable is used to connect the FBG sensor probes and the automatic data collection system. The automatic data collection system is located fifty meters away from the sensor probes. Leveraging the fiber optic sensors' long-distance sensing capability, signals from the FBG sensors can be transmitted to the data collection system fifty meters away via the fiber optic cable.

Automatic data collection system: The automatic data collection system includes an optical interrogator (HYPERION si255), which is a ruggedized, industrial grade device capable of static and dynamic full-spectrum analysis, a 24-port optical distribution frame which is used for optical cable management and protection, and a Raspberry Pi which enables automatic data collection.

Automatic transmission system: Figure 3-5 shows the automatic transmission system which includes an LTE module installed in the Raspberry Pi and a cloud server.

Supporting system: Supporting system mainly includes an Uninterruptible Power Supply (UPS) power supply, a customized Polymethyl Methacrylate (PMMA) box and a Closed-Circuit Television (CCTV) system.

These five systems can achieve four key functions include:

Data Processing: The interrogator demodulates wavelength shifts from the FBG sensors. The Raspberry Pi collects the data from the interrogator and uploads the collected data to the cloud server.

Cloud Connectivity: The Long-Term Evolution (LTE) module installed in the Raspberry Pi provides a stable 4G cellular network to upload the data to a cloud server. The cloud server can be accessed remotely with a website.

Power Management: UPS installed in the monitoring system ensures continuous and stable operation.

Environmental Protection: Figure 3-6 shows armored fiber cables on-site were secured using metal hangers and Polyvinyl Chloride (PVC) conduits. The interrogator and Raspberry Pi were housed in a customized PMMA box. Besides, CCTV can be accessed remotely via a website.

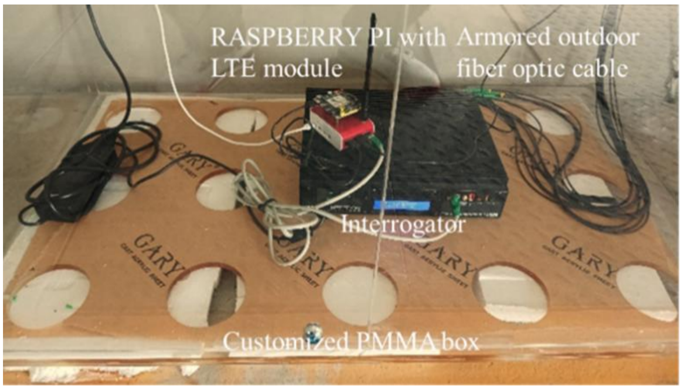


Figure 3-5 Automatic data collection system and transmission system placed in a PMMA box

Figure 3-6 Armored fiber cables fixed on the ground

### 3.2.3 Field tests to validate the embeddable FBG-based sensing system for monitoring relative humidity inside concrete

To validate the field performance of the embeddable FBG-based sensing system for monitoring relative humidity, the sensing system was installed in a concrete beam sample placed in Hong Kong-Zhuhai-Macao Bridge (HZMB) exposure site with the help from the Hong Kong-Zhuhai-Macao Bridge Authority in Zhuhai.

*3.2.3.1 Introduction of HZMB exposure site*

The HZMB is a remarkable infrastructure project which covers 55 kilometers and is composed of 12 kilometers Hong Kong Link Road, 29.6 kilometers Main Bridge and 13.4 kilometers Zhuhai Link Road. The HZMB exposure site is situated on the West Artificial Island of the bridge. In the exposure site samples are under real-world marine conditions, which can provide a more complex environment than that in the environmental chamber. HZMB exposure site can provide dynamic and complex factors like salinity, temperature gradients, pressure, waves, currents, and biofouling which provided unexpected changes in the relative humidity, revealing vulnerabilities that controlled environmental chamber settings miss. Besides in the exposure site, the sensors are exposed to high humidity environment, and high UV radiation which higher the demands on the system stability. Figure 3-7 shows the location and entrance of the exposure site.


(a)

(b)

Figure 3-7 (a) Location of the exposure site (b) Entrance of the exposure site

The exposure site comprises four distinct zones: air zone (+6.2 m), splash zone (+2.5 m), water level variation zone (0.0 m), and underwater zone (-2.1 m). The designed average water level is 0.54 m, and the designed highest water level is 3.26 m.

*3.2.3.2 Concrete beam sample prepared for field tests and installation of FBG sensors*

Figure 3-8 shows FRP reinforced seawater sea-sand concrete (SWSSC) beam samples for field test. The FBG-based relative humidity sensors were embedded within the concrete beam sample. C55 grade of SWSSC was supplied by Gammon Construction Ltd. Seawater was taken from Ap Lei Chau Salt-water Pumping Station in Hong Kong, and sea-sand was imported from overseas. The FRP reinforcing bars were purchased from Dextra Pacific Ltd. Beam size is 1600 mm × 190 mm × 140 mm.

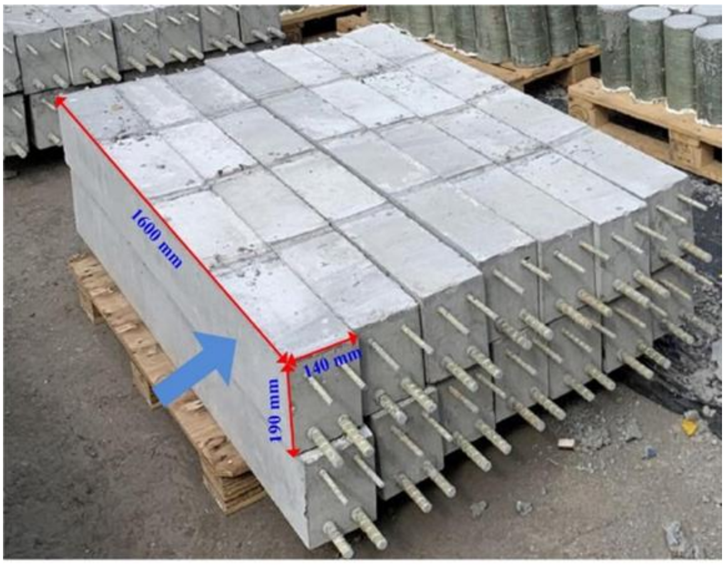


Figure 3-8 FRP reinforced SWSSC beam samples

*3.2.3.3 Calibration of the FBG-based sensors for monitoring relative humidity*

Before installing the FBG-based sensors for monitoring relative humidity inside the concrete beam sample, four FBG sensors were calibrated in an environmental chamber. The temperature and the humidity sensitivity of FBG (T) and FBG (RH) were calibrated as follows:

- Set the relative humidity inside the environmental chamber at 35%.
- Starting from 25℃, increase the temperature inside the environmental chamber by 5℃ every time until 45℃.
- Record the peak wavelength and the corresponding temperature.
- Set the temperature inside the environmental chamber at 25℃.
- Starting from 35%, increase the relative humidity inside the environmental chamber by 10% every time until 75%.
- Record the peak wavelength and the corresponding relative humidity.
- Analyze the data collected with a computer.

*3.2.3.4 Installation of the embeddable FBG-based sensing system for monitoring relative humidity*

After calibration, the FBG-based sensors for monitoring relative humidity were installed inside the prepared concrete beam sample. The steps of the installation of the FBG sensors are as follows: (1) Drilling: Precise holes were drilled into the beam to accommodate the sensors. (2) Sensor Placement: FBG sensors were inserted into cavities carefully and remained suspended in the cavities. Then, fiber optic cables and beam surfaces were sealed using epoxy adhesive to prevent seawater ingress (see Figure 3-9 (a)). (3) Sensor Protection: Four waterproof PVC enclosures were mounted above the sensor locations to shield the instrumentation (see Figure 3-9 (b)). (4) Deployment: The instrumented beam was placed in the HZMB exposure site (see Figure 3-9 (c)).

The automatic data collection system, and automatic transmission system were placed in a pump station 200 meters away from the exposure site. In the pump station, the automatic data collection system, and automatic transmission system were protected by a customized PMMA box and were connected to a PSU for stable power supply. The FBG sensors installed in the concrete beam sample were connected to the data collection system with armored fiber cables. Besides, to secure the armored fiber cables in the open air, metal hangers and polyvinyl chloride (PVC) conduits were used to fasten the cables to the ground.

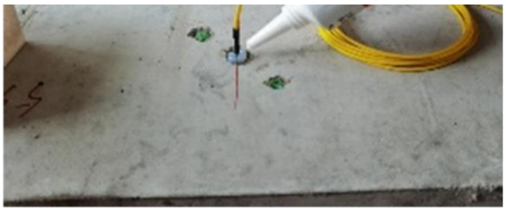

(a)

(b)

(c)

Figure 3-9 (a) Isolating and fixing FBG sensors (b) Waterproof PVC boxes to protect the FBG sensors (c) Concrete specimen placed in the exposure site

*3.2.3.5 Installation of a commercial sensing system*

To validate the performance of the embeddable FBG-based sensing system for monitoring relative humidity, a commercial sensing system (LumiCon) was installed in the same exposure site (see Figure 3-10). The commercial sensing system includes LumiSense-RH sensor cable, LumiNode and LumiHub Gateway. LumiSense-RH sensor is a flexible one-point temperature and humidity sensor cable designed to endure harsh conditions such as being embedded directly inside concrete structures. Specifications of the LumiSense-RH sensor cable are provided in Table 3-1. One end of the cable is the sensor and the other end of LumiSense sensor cable is connected to LumiNode. LumiNode is a wireless transmission device which sends data collected from the sensor cable directly to the LumiHub Gateway. Technical specifications of the LumiNode are detailed in Table 3-2. LumiHub Gateway is a gateway which receives the data sent from LumiHubs installed on site and sends the collected data to cloud server.

The steps of the installation of the commercial sensing system are as follows: Drilling: Four holes were drilled into the beam close to the PVC protection box installed for the protection of FBG sensors. Sensor Placement: commercial sensors were inserted into the cavities and sealed using epoxy adhesive to prevent seawater ingress.

LumiNodes were fixed in the wall near the beam (see Figure 3-10). LumiHub Gateway was placed in the same PMMA box and connected to the UPS from the FBG-based sensing system.

Table 3-1 LumiSense RH sensor specifications

| **Parameters** | | **Accuracy** | **Resolution** | **Range** | **Response time** | **Long term drift** | **Photo** |
|---|---|---|---|---|---|---|---|
| | Unit | ℃ | | | seconds | ℃/year | |
| Lumi Sense RH Pro sensor | Temperature | ±0.1 | 0.01 | -40 to 125 | <10 | <0.03 |  |
| | Unit | %RH | | | seconds | %RH/year | |
| | Humidity | ±1.5 (0 to 80%)<br>±2 (80% to 100%) | 0.01 | 0 to 100 | <10 | <0.25 | |

Table 3-2 LumiNode specifications

| **Parameters** | **Dimension** | **Operating temperature rate** | **Net weight** | **IP rating** | **Battery life** | **Photo** |
|---|---|---|---|---|---|---|
| Unit | cm | ℃ | g | - | month |  |
| Lumi Node | 10.8 × 10 × 8.3 | -20 to 60 | 520 | IP68 | 12 | |

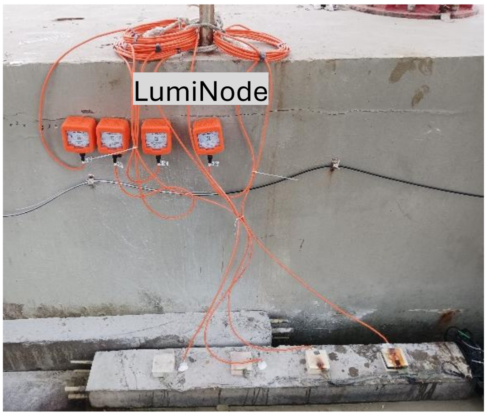


Figure 3-10 Commercial sensing system installed in the exposure site

## 3.3 Results and Discussion

### 3.3.1 Calibration of the FBG-based sensors for monitoring relative humidity

Figure 3-11 to Figure 3-18 shows the calibration results. From the result we can find that the FBG(T) and FBG(RH) had different sensitivity to temperature, and FBG(T) was insensitive to humidity changes. Thus, the relative humidity can be calculated with the shift of the relative peak wavelength from FBG(T) and FBG(RH). The equations were listed below:

( $\Delta\lambda_{FBG(T)n}$ was the wavelength shift from FBG(T) in FBG humidity sensor n, $\Delta\lambda_{FBG(H)n}$ was the wavelength shift from FBG(RH) in FBG humidity sensor n)

$$T = 25.06 + 120.48\Delta\lambda_{FBG(T)1} \quad (3\text{-}2)$$

$$H = 35.01 + 273.22(\Delta\lambda_{FBG(H)1} - 1.21\Delta\lambda_{FBG(T)1}) \quad (3\text{-}3)$$

$$T = 25.00 + 121.80\Delta\lambda_{FBG(T)2} \quad (3\text{-}4)$$

$$H = 35.01 + 229.36(\Delta\lambda_{FBG(H)2} - 1.28\Delta\lambda_{FBG(T)2}) \quad (3\text{-}5)$$

$$T = 25.06 + 121.51\Delta\lambda_{FBG(T)3} \quad (3\text{-}6)$$

$$H = 35.00 + 147.49(\Delta\lambda_{FBG(H)3} - 1.45\Delta\lambda_{FBG(T)3}) \quad (3\text{-}7)$$

$$T = 25.05 + 111.86\Delta\lambda_{FBG(T)4} \quad (3\text{-}8)$$

$$H = 35.01 + 232.56(\Delta\lambda_{FBG(H)4} - 1.23\Delta\lambda_{FBG(T)4}) \quad (3\text{-}9)$$

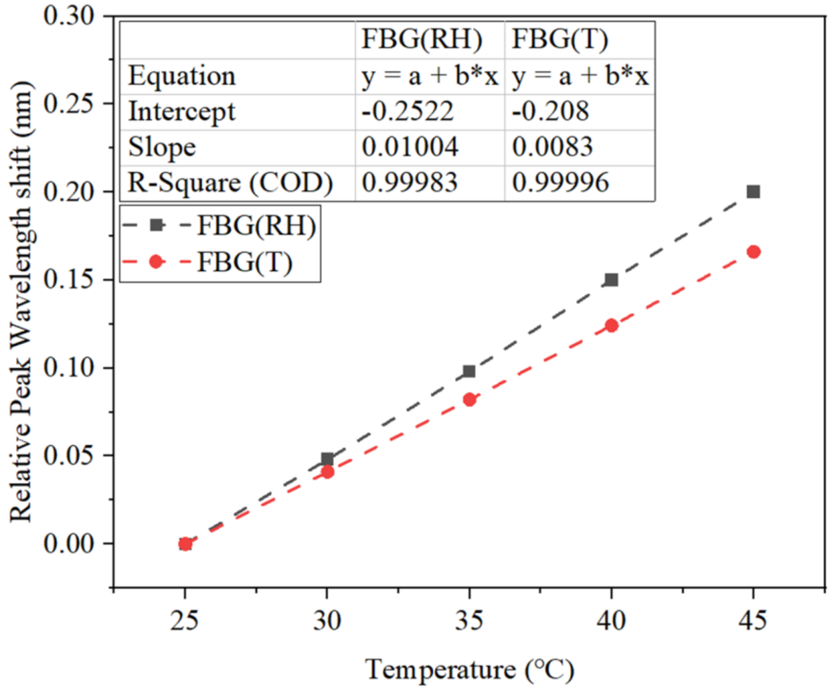


Figure 3-11 Temperature calculation results (relative humidity sensor 1)

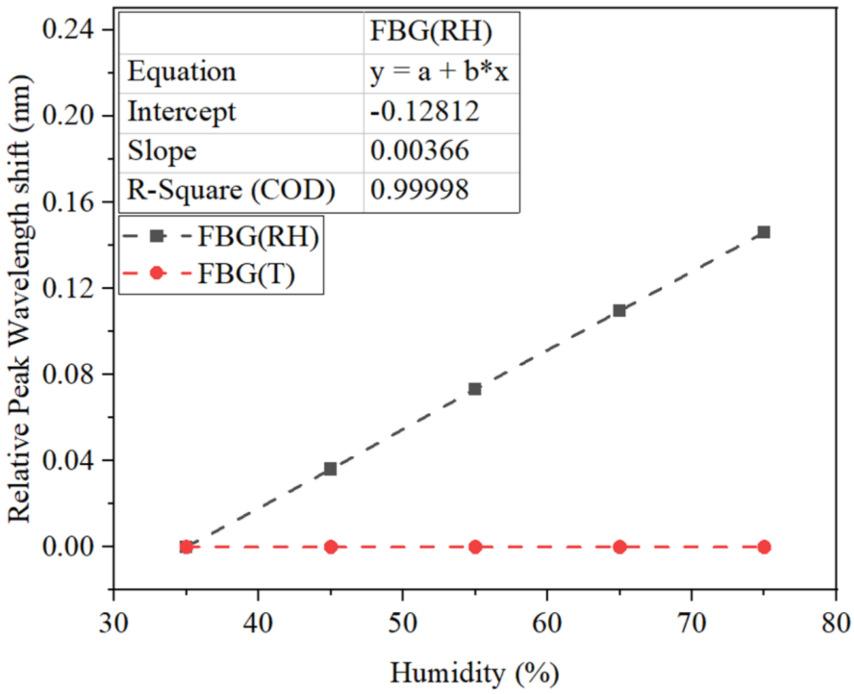


Figure 3-12 Humidity calculation results (relative humidity sensor 1)

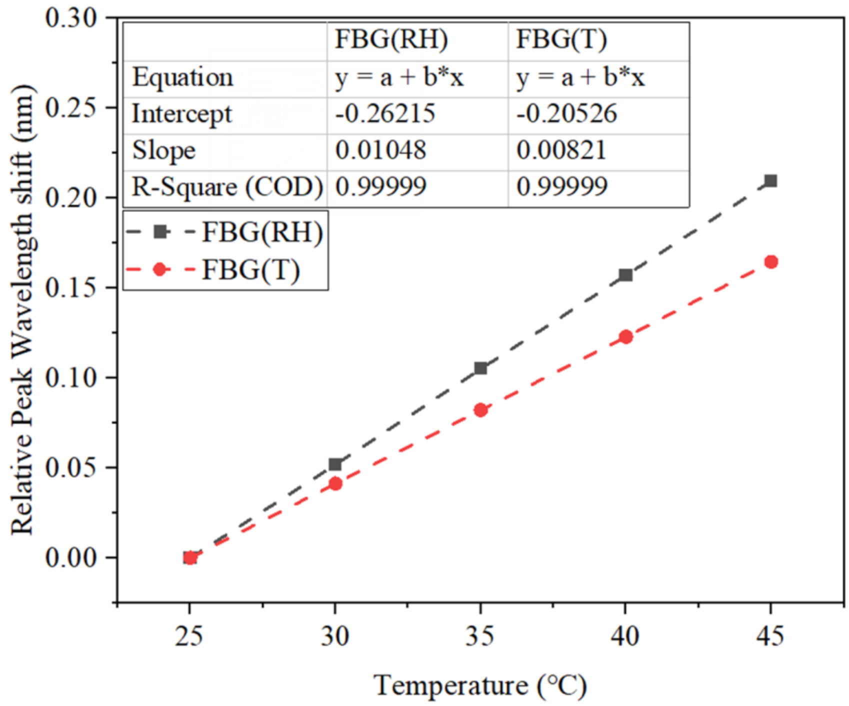


Figure 3-13 Temperature calibration results (relative humidity sensor 2)

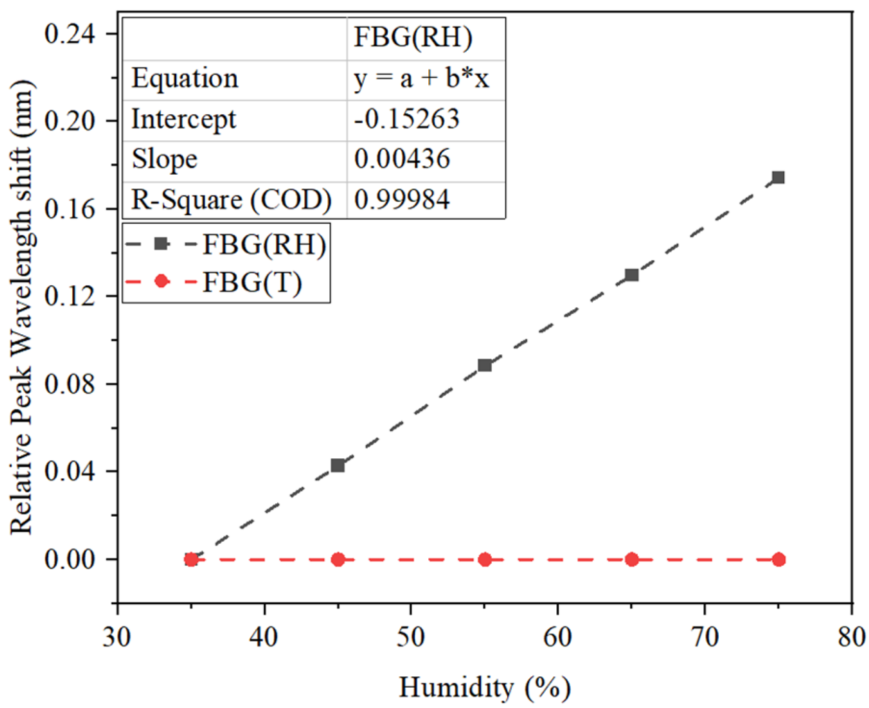


Figure 3-14 Humidity calibration results (relative humidity sensor 2)

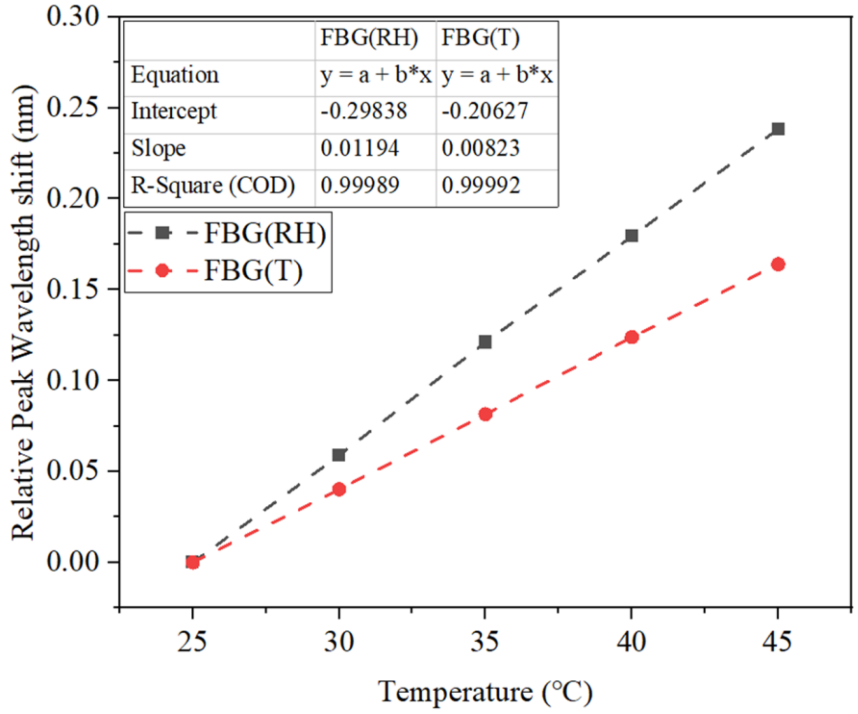


Figure 3-15 Temperature calibration results (relative humidity sensor 3)

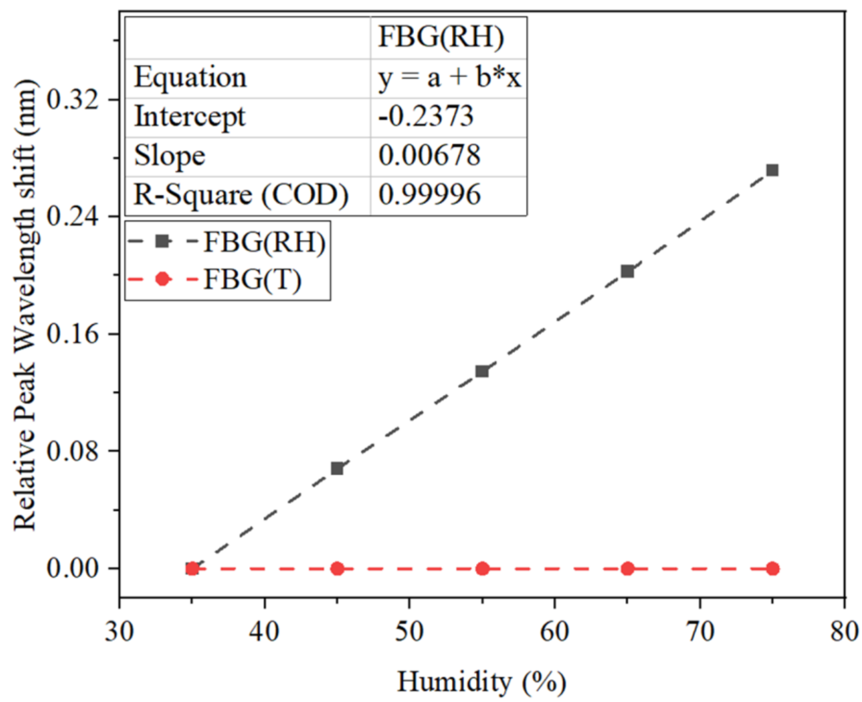


Figure 3-16 Humidity calibration results (relative humidity sensor 3)

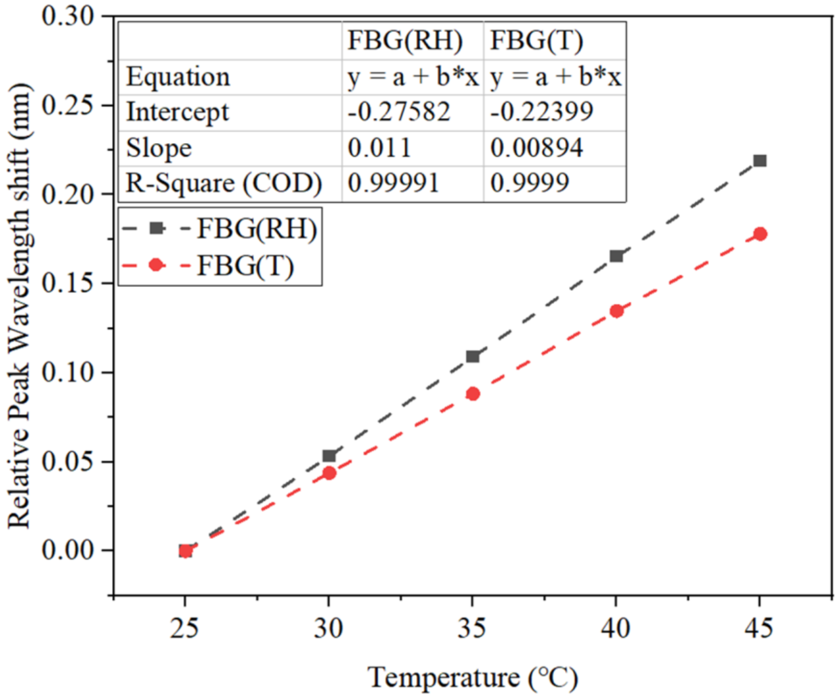


Figure 3-17 Temperature calibration results (relative humidity sensor 4)

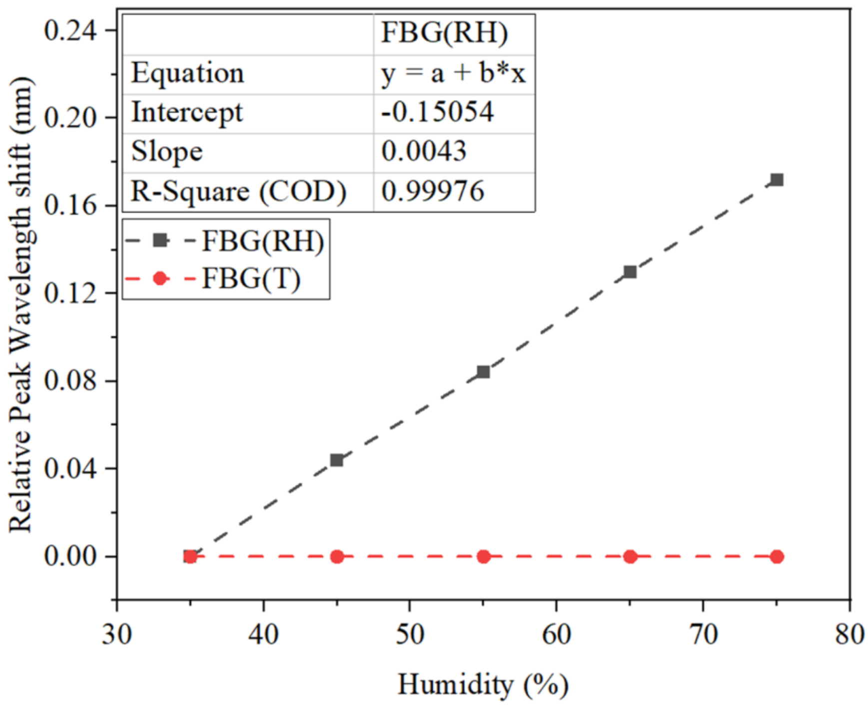


Figure 3-18 Humidity calibration results (relative humidity sensor 4)

The response time of the developed FBG-based sensor for monitoring relative humidity during the calibration was one minute.

## 3.3.2 Results of the long-term field tests of the embeddable FBG-based sensing system for monitoring relative humidity

### *3.3.2.1 Overview of FBG-based sensing system operation*

The FBG-based sensing system for monitoring relative humidity worked well for more than two years (February 2021 to March 2023). During this period, the data was uploaded to the cloud server automatically and the data could be accessed and downloaded with a website (see Figure 3-19). This field test shows the distinct advantages of FBG sensors in remote accessibility and operational convenience. FBG sensors can transmit high-precision data over long distances with minimal signal loss and this unique advantage enables the FBG-based sensing system to collect data from the sensors installed in extreme environmental conditions. This advantage eliminates the need for frequent onsite inspections and provides real-time, continuous monitoring of parameters concerned inside the concrete.

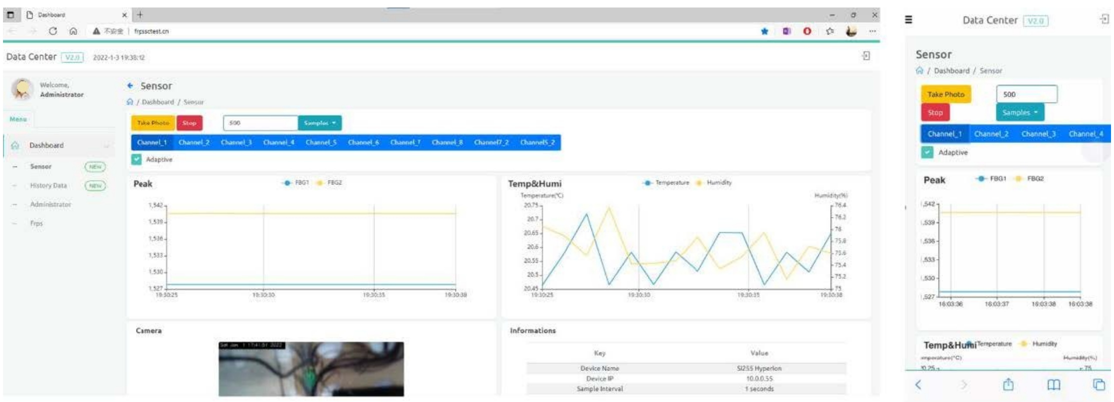


(a) (b)

Figure 3-19 Interface of the FBG-based sensing system for monitoring relative humidity: (a) PC interface (b) Mobile interface

#### *3.3.2.2 Data comparison with the commercial sensing system*

Figure 3-20 and Figure 3-21 shows the comparison of the data from FBG-based sensing system for monitoring relative humidity and commercial sensing system (LumiCon) installed in SWSSC beam sample. Relative humidity and temperature data were recorded in February 2023.

Temperature measurements from both sensing systems demonstrated strong agreement, with the FBG-based sensing system capturing marginally higher peak temperatures (Figure 3-20). However, in Figure 3-21, the FBG-derived relative humidity values exhibited a consistent deviation, registering approximately 20% lower than those from the LumiCon sensors.

This discrepancy may arise from methodological discrepancies in sensor installation protocols. The commercial sensors featured larger probes, (diameter 6mm, length 30mm) which was much larger than the size of the FBG-based sensor. In addition, the diameter of the cable is smaller than the commercial sensor probe (Figure 3-22). To install the sensor probe inside the beam, the hole drilled in the beam was larger than the cable. Thus it was hard to keep the sensor fully isolated with the waterproof epoxy sealant. Additionally, unlike the FBG sensors, the LumiCon probes lacked secondary protection from waterproof PVC boxes. These factors likely contributed to sustained humidity readings above 90% in the commercial system, potentially reflecting localized moisture ingress rather than true relative humidity inside the concrete beam.

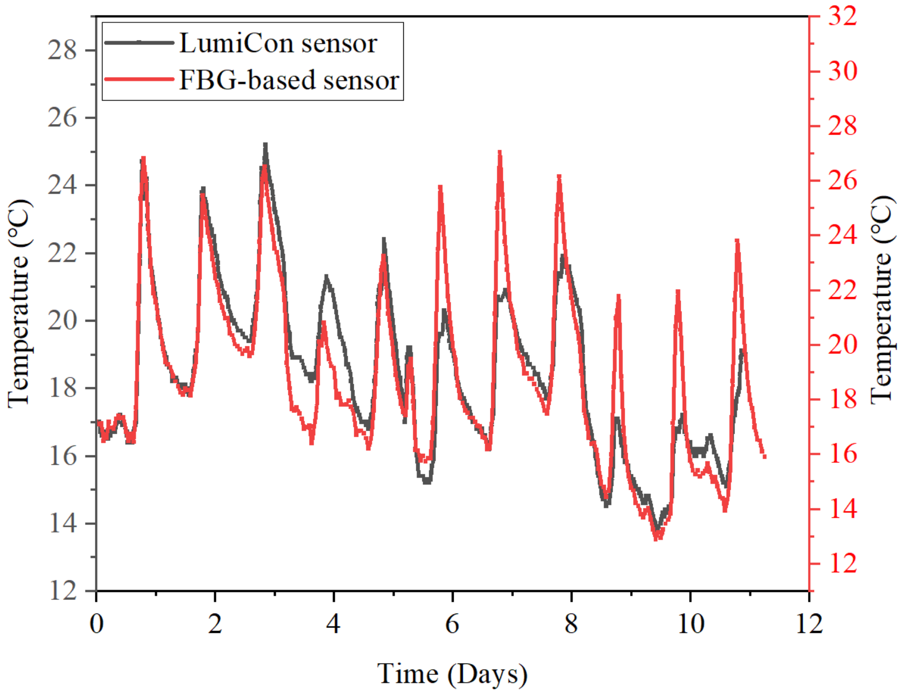


Figure 3-20 Comparison of temperature data from the commercial sensing system and the FBG-based sensing system

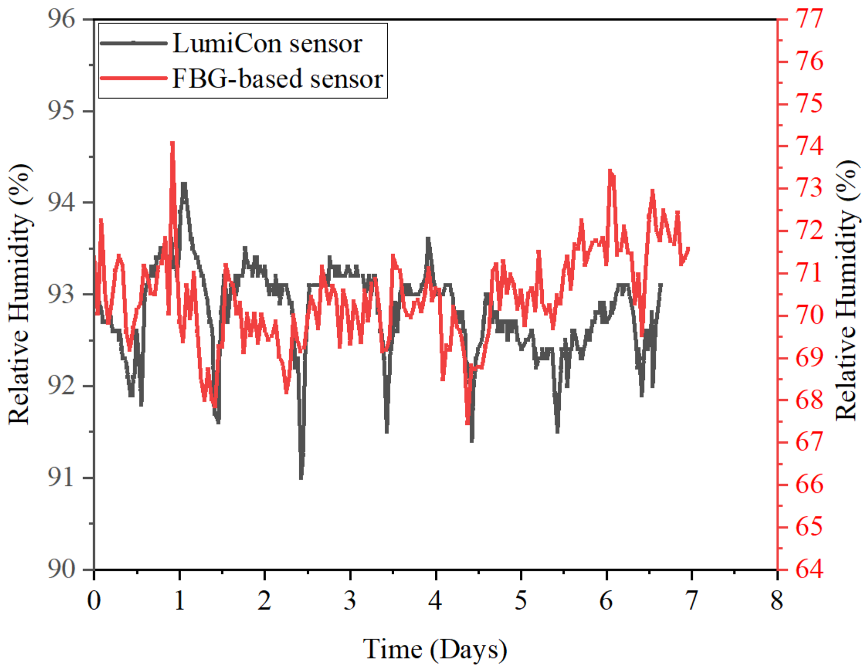


Figure 3-21 Comparison of relative humidity from the commercial sensing system and the FBG-based sensing system


Figure 3-22 LumiCon sensor probe (black) and cable (orange)

*3.3.2.3 Data collected from the FBG-based sensing system during extreme climate change*

The embeddable FBG-based sensing system for monitoring relative humidity worked well under extreme climate change. Climate changes will cause changes in temperature and relative humidity inside the concrete beam, and the sensing system can monitor these changes. Tropical storms and cold fronts are two common weather conditions in the local climate. Two sets of the temperature and humidity recorded by the sensing system during a tropical storm and a cold front are shown in the following paragraph.

(1) Relative humidity and temperature collected during the tropical depression and tropical storm in August 2021

On the night of 2 August, an area of low pressure over the northern part of the South China Sea became a tropical depression and kept moving eastwards slowly across the northern part of the South China Sea. The tropical depression transferred to a tropical storm with heavy rains on the morning of 4 August.

On 2 August, when the tropical depression was developing, the weather was hot, and the temperature recorded by the system reached to a peak at 36 ℃ (see Figure 3-23). From 3 August to 5 August, when there were occasional heavy showers and squally thunderstorms, the humidity recorded by the system had an upward trend. The relative humidity and temperature collected by the embeddable FBG-based sensing system for monitoring relative humidity was consistent with climate change brought by the tropical depression and tropical storm.

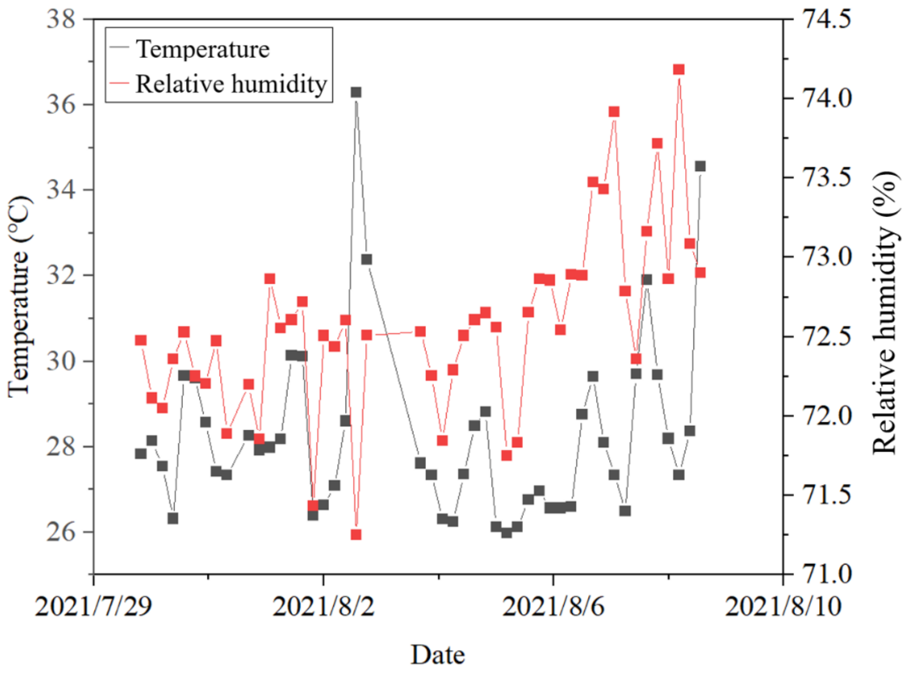


Figure 3-23 Relative humidity and temperature collected during the tropical depression in August 2021

(2) Relative humidity and temperature collected during the cold front in November 2021

A cold front moved across the exposure site on the morning of 8 November. With winds coming from the north and a few rain patches, temperatures fell significantly on the morning of 8 November. Under the influence of the associated dry northeast monsoon, the weather turned dry.

On 8 November the temperature dropped down from 31℃ to 20 ℃ and the relative humidity dropped down from 75% to 69.5% (see Figure 3-24). The relative humidity and temperature collected by the embeddable FBG-based sensing system for monitoring relative humidity was consistent with climate change brought by the cold front.

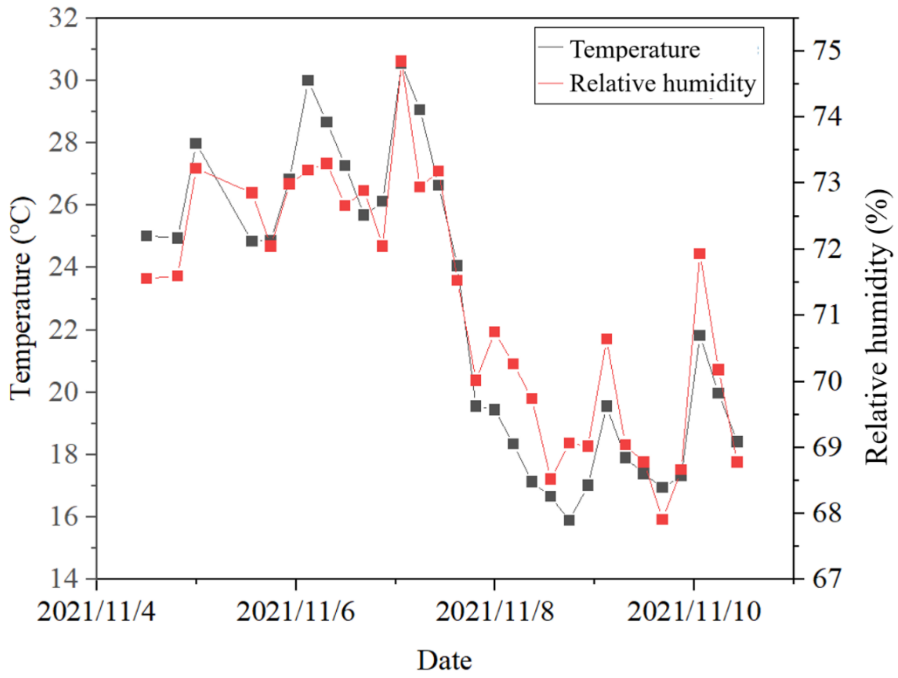


Figure 3-24 Relative humidity and temperature collected during the cold front in November 2021

## 3.4 Conclusions

This chapter presents the development of an embeddable FBG-based sensing system for monitoring relative humidity inside the concrete and validation of the sensing system with long-term field tests in marine environments.

The FBG-based relative humidity sensor leverages dual FBGs, with one polyimide-coated FBG for humidity sensing and an uncoated FBG for temperature compensation. Then, the embeddable FBG-based sensing system for monitoring relative humidity, comprising sensor probe, armored fiber optic cables, an automatic data collection, and an automatic data transmission system, was installed in an exposure site for long-term field tests. The sensing system demonstrated robust performance over a two-year period during the field tests even under tropical storms and cold fronts.

Besides, comparative analysis with a commercial sensing system revealed a consistent temperature and a consistent 20% lower humidity reading from the FBG-based sensing system, attributed to differences in sensor installation and protection methods.

To successfully apply FBG-based sensing system for monitoring relative humidity inside concrete, several innovative work has been carried out. First is innovative packaging. A perforated polyether-ether ketone (PEEK) tube was installed outside the FBG probe to ensure the FBG sensors only being affected by the stress caused by the shrinkage or swelling of the polyimide coating. In addition, during installation, PVC waterproof boxes were used to provide an additional waterproof layer and protect the FBG cable from wind and other influences. Besides, the distributed installation of sensors and demodulator is another innovation to support the successful operation of equipment. This allows the demodulator to operate stably in suitable environments.

These findings highlight the advantages of FBG-based sensing system for monitoring chemical parameters, such as compact size, chemical resistance, and distributed sensing, which are critical to apply FBG-based sensing system in challenging marine environments. The system's ability to provide continuous, real-time data with minimal onsite intervention aligns with the growing demand for cost-effective, durable monitoring of chemical parameters inside the concrete.

# CHAPTER 4. MACHINE LEARNING AIDED DATA ANALYSIS OF LONG-TERM FIELD TESTS OF FBG-BASED SENSING SYSTEM FOR MONITORING RELATIVE HUMIDITY INSIDE CONCRETE

## 4.1 Introduction

Machine learning gains more attention in the fiber optic sensing system data analysis nowadays. The study carried out by researchers like Kandel (Khandel et al. 2021), Li (Li et al. 2023), and Castellon (Fernandez Castellon et al. 2021) shows the great potential of applying machine learning in the fiber optic sensing system data analysis.

Gaussian Process excels in modelling complex nonlinear relationships which can be applied as a useful tool to predict the parameters concerned based on historical data from the sensor. It provides a probabilistic approach to forecasting, where predictions are made with an estimation of uncertainty. Due to its flexibility and robustness, Gaussian Process is widely applied in fields ranging from robotics to environmental science, where precise modelling of uncertain systems is crucial. It is a useful tool to predict the parameters concerned based on historical data from the sensor. In field applications, installed sensors will be offline during maintenance work. For the consistency of sensor data during maintenance work, in this chapter, a Gaussian Process model is trained with the historical environmental relative humidity, historical environmental temperature and historical measured relative humidity from the long-term field test of the embeddable FBG-based sensing system for monitoring relative humidity inside concrete to predict the relative humidity inside the concrete beam sample for the next few days.

## 4.2 Gaussian Process Model Training and Data Set

### 4.2.1 Introduction of Gaussian Process

Gaussian Process represents a powerful statistical modelling technique often used for regression and classification tasks in machine learning. Gaussian Processes have been demonstrated as a highly effective non-parametric Bayesian modelling method due to their ability to perform precise Bayesian analysis using straightforward matrix operations while delivering strong performance. A Gaussian Process consists of a set of random variables, and when a finite number of variables are drawn from the process, they collectively adhere to a multivariate Gaussian distribution with the appropriate mean vector and covariance matrix. When referring to an unknown mapping $g: x \to \mathbb{R}$ represented by a Gaussian Process, denoted in:

$$(x) \sim \mathcal{GP}(m(x), k(x, x^{'}; \boldsymbol{\theta})) \tag{4-1}$$

The Gaussian Process is fully characterized by the mean function $m(x)$ and the covariance function $k(x, x'; \boldsymbol{\theta})$. Typically, for simplicity, the prior mean function is set to zero, while the covariance function $k(x, x'; \boldsymbol{\theta})$ is defined by a positive definite kernel that is parameterized by $\boldsymbol{\theta}$.

If we have a set of labelled pairs $(x_i, y_i)$ where i ranges from $i = 1, 2, \ldots, n$ obtained from the unknown mapping $g: x \to \mathbb{R}$ vectors can be represented $\hat{\mathbf{x}} \in \mathbb{R}^n$ and $\hat{\mathbf{y}} \in \mathbb{R}^n$ as $(x_1, x_2, \ldots, x_n)^{\mathrm{T}}$ and $(y_1, y_2, \ldots, y_n)^{\mathrm{T}}$, respectively, for the sake of brevity. In more realistic modelling scenarios, the observations are affected by noise and are associated with both function values and a noise term. In other words, $\hat{y} = g(x) + \varepsilon$, where $\varepsilon$ represents independent and identically distributed Gaussian noise with a mean of 0 and $\sigma_n$ (standard deviation). The parameter $\sigma_n$ specifies the noise level of the measurements. Assuming that $g$ is a Gaussian Process, any finite set of variables drawn from $g$ will follow multi-variate Gaussian distribution. Consequently, the multivariate Gaussian distribution of the measured data $\hat{\mathbf{y}}$ at sample locations $\hat{\mathbf{x}}$ and the function values $\hat{\mathbf{g}}_*$ at test locations $\hat{\mathbf{x}}_*$ can be written using:

$$\begin{bmatrix} \hat{\mathbf{g}}_* \\ \hat{\mathbf{y}} \end{bmatrix} \sim \mathcal{N}\left(\mathbf{0}, \begin{bmatrix} \mathbf{K}(\hat{\mathbf{x}}_*, \hat{\mathbf{x}}_*) & \mathbf{K}(\hat{\mathbf{x}}_*, \hat{\mathbf{x}}) \\ \mathbf{K}(\hat{\mathbf{x}}, \hat{\mathbf{x}}_*) & \mathbf{K}(\hat{\mathbf{x}}, \hat{\mathbf{x}}) + \sigma_n^2 \mathbf{I} \end{bmatrix}\right) \tag{4-2}$$

where the matrices $\mathbf{K}$ are derived from the specified covariance function. By applying Bayes' theorem, we can construct the posterior distribution of function values $\hat{\mathbf{g}}_*$ given measured data $\hat{\mathbf{y}}$ as following:

$$p\left(\hat{\mathbf{g}}_* \middle| \hat{\mathbf{y}}; \hat{\mathbf{x}}, \hat{\mathbf{x}}_*, \boldsymbol{\theta}, \sigma_n\right) = \frac{p(\hat{\mathbf{y}}, \hat{\mathbf{g}}_*; \hat{\mathbf{x}}, \hat{\mathbf{x}}_*, \boldsymbol{\theta}, \sigma_n)}{\int p(\hat{\mathbf{y}}, \hat{\mathbf{g}}_*; \hat{\mathbf{x}}, \hat{\mathbf{x}}_*, \boldsymbol{\theta}, \sigma_n)\, \mathrm{d}\hat{\mathbf{g}}_*} \tag{4-3}$$

The probability function $p(\hat{\mathbf{y}}, \hat{\mathbf{g}}_*; \hat{\mathbf{x}}, \hat{\mathbf{x}}_*, \boldsymbol{\theta}, \sigma_n)$ in the numerator is straightforward to derive because $\hat{\mathbf{g}}_*$ and $\hat{\mathbf{y}}$ jointly adhere to a multivariate Gaussian distribution, resulting in:

$$p(\hat{\mathbf{y}}, \hat{\mathbf{g}}_*; \hat{\mathbf{x}}, \hat{\mathbf{x}}_*, \boldsymbol{\theta}, \sigma_n) = \frac{1}{(2\pi)^{n+n_*} |\hat{\boldsymbol{\Sigma}}|^{\frac{1}{2}}} \exp\left(-\frac{1}{2} \begin{bmatrix} \hat{\mathbf{g}}_* \\ \hat{\mathbf{y}} \end{bmatrix}^{\mathrm{T}} \hat{\boldsymbol{\Sigma}}^{-1} \begin{bmatrix} \hat{\mathbf{g}}_* \\ \hat{\mathbf{y}} \end{bmatrix}\right) \tag{4-4}$$

where $\widehat{\boldsymbol{\Sigma}}$ represents the prior covariance matrix in equation (4-3), and $n_*$ denotes the number of test locations. Considering that the denominators in equation (4-4) and equation (4-5) are constant factors proportional to each other and independent of $\widehat{\mathbf{g}}_*$, and the inverse of $\widehat{\boldsymbol{\Sigma}}$ can be expressed by the corresponding sub-matrices (i.e., $\mathbf{K}(\widehat{\mathbf{x}}_*, \widehat{\mathbf{x}}_*)$, $\mathbf{K}(\widehat{\mathbf{x}}_*, \widehat{\mathbf{x}})$, $\mathbf{K}(\widehat{\mathbf{x}}, \widehat{\mathbf{x}}_*)$, and $\mathbf{K}(\widehat{\mathbf{x}}, \widehat{\mathbf{x}}) + \sigma_n^2\mathbf{I}$), equation can be rephrased as:

$$p\left(\widehat{\mathbf{g}}_* \middle| \widehat{\mathbf{y}}; \widehat{\mathbf{x}}, \widehat{\mathbf{x}}_*, \boldsymbol{\theta}, \sigma_n\right) = \frac{1}{z} \exp\left(-\frac{1}{2}\left[\widehat{\mathbf{g}}_* - \overline{\mathbf{g}}_*\right]^{\mathrm{T}} \mathrm{cov}\left(\widehat{\mathbf{g}}_*\right)^{-1}\left[\widehat{\mathbf{g}}_* - \overline{\mathbf{g}}_*\right]\right) \tag{4-5}$$

where the constant $z$ is related to the parameters $\boldsymbol{\theta}$ and $\sigma_n$; the mean vector $\overline{\mathbf{g}}_*$ and covariance matrix $\mathrm{cov}(\widehat{\mathbf{g}}_*)$ are respectively given by:

$$\overline{\mathbf{g}}_* = \mathbf{K}(\widehat{\mathbf{x}}_*, \widehat{\mathbf{x}})\, \widetilde{\mathbf{K}}^{-1}\mathbf{y} \tag{4-6}$$

$$\mathrm{cov}\left(\widehat{\mathbf{g}}_*\right) = \mathbf{K}(\widehat{\mathbf{x}}_*, \widehat{\mathbf{x}}_*) - \mathbf{K}(\widehat{\mathbf{x}}_*, \widehat{\mathbf{x}})\widetilde{\mathbf{K}}^{-1}\mathbf{K}(\widehat{\mathbf{x}}, \widehat{\mathbf{x}}_*) \tag{4-7}$$

### 4.2.2 Data set for Gaussian Process model training

The data set includes the relative humidity and temperature data obtained from the embeddable FBG-based sensing system for monitoring relative humidity and the data from automatic weather buoy from Hong Kong Observatory.

Measured humidity is from the embeddable FBG-based sensing system for monitoring relative humidity installed in the exposure site.

Environmental relative humidity and temperature is recorded from Automatic Weather Buoy No.2 (Hong Kong International Airport, West) installed by Hong Kong Observatory. Hong Kong Observatory is an official government authority responsible for monitoring and forecasting weather. They have installed automated meteorological stations designed to track wind patterns, both dry and wet-bulb temperature readings, dew point levels, humidity percentages, barometric pressure, precipitation levels, sunlight exposure, ultraviolet radiation intensity, the Hong Kong Heat Index, and atmospheric clarity.

The location of the Buo is Latitude N $22°17'28''$ and Longitude E $113°52'56''$. This automatic weather buoy is selected because its location is close to the exposure site where the FBG-based relative humidity sensor is installed, and it measures the relative humidity in the marine environment. The data set includes relative humidity and temperature obtained from January 2022 to June 2023.

### 4.2.3 Gaussian Process model to predict relative humidity inside the concrete beam sample

A Gaussian Process model is initially trained to map environmental relative humidity and temperature to the relative humidity inside the beam, enabling accurate predictions of internal conditions. Figure 4-1 shows the process of relative humidity prediction with GP model, data spanning 15 days on environmental relative humidity and temperature from the automatic weather buoy station, along with relative humidity collected from the FBG-based sensing system, were used to train the Gaussian Process model. The subsequent 15 days of environmental relative humidity and temperature from the automatic weather buoy station were employed to predict the relative humidity inside the concrete beam. Then the predicted relative humidity and measured relative humidity were compared to evaluate the model's performance.

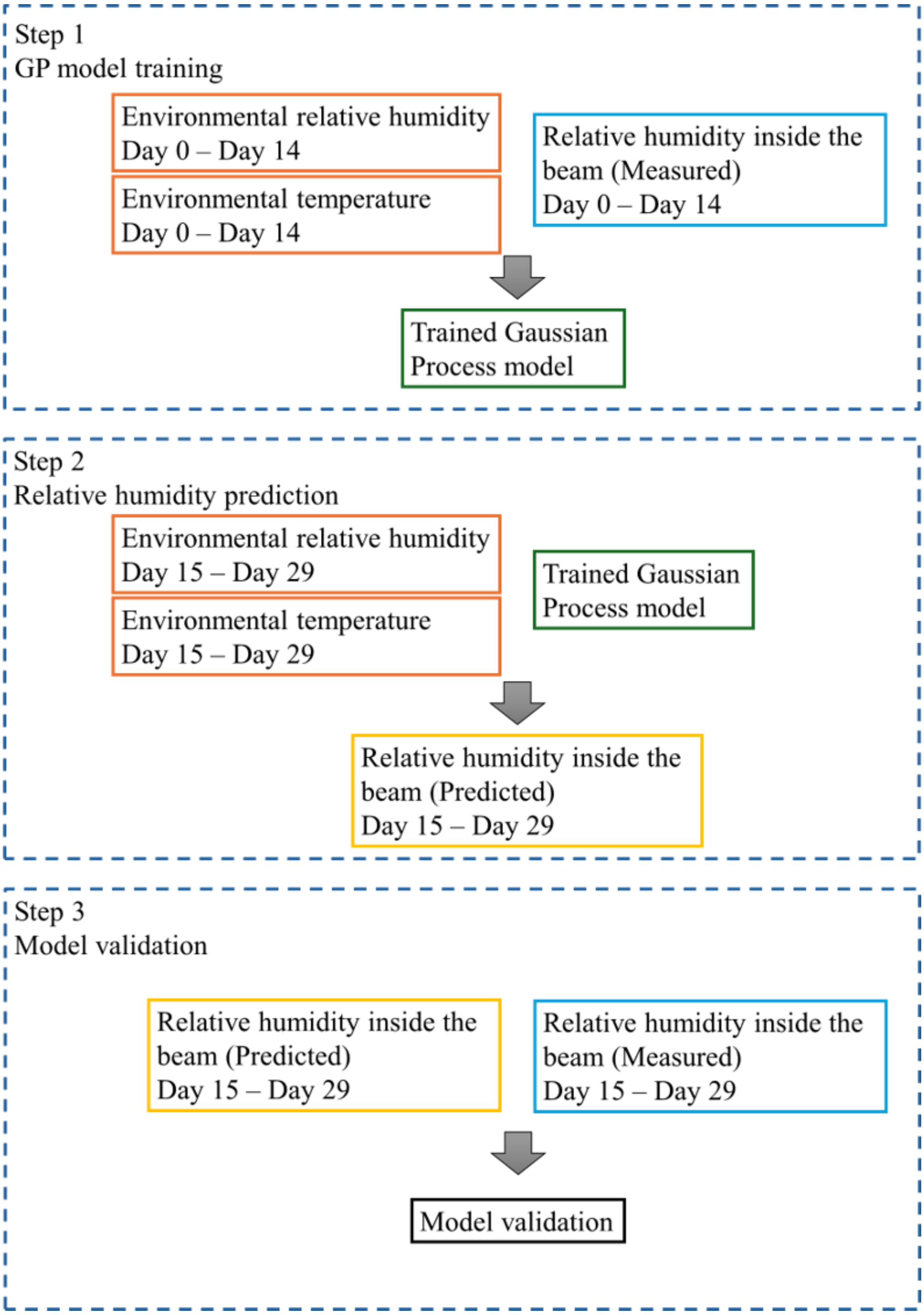


Figure 4-1 Process of relative humidity prediction with GP model

## 4.3 Results and Discussion

The subsequent 15 days of measured relative humidity from FBG-based sensing system and predicted relative humidity with Gaussian Process model is shown below.

Measured relative humidity was collected from the Channel 1 in the FBG-based sensing system. Predicted relative humidity was generated by the Gaussian Process model trained by the data from January 1, 2022, to January 15, 2022. We can find that most measured relative humidity was included in the predicted 2 $\boldsymbol{\sigma}$ confidence interval (see Figure 4-2).

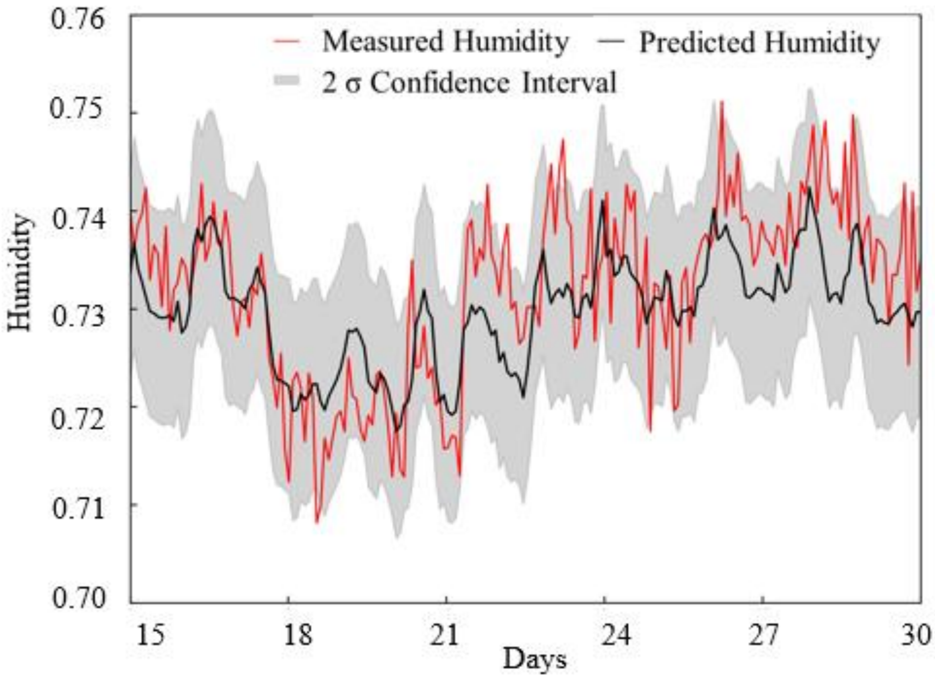


Figure 4-2 Comparison of measured relative humidity and predicted relative humidity (Channel 1 January)

Then, a different channel from the FBG sensor system is chosen. The measured relative humidity was collected from the Channel 4 in the FBG-based sensing system. Predicted relative humidity was generated by the Gaussian Process model trained by the data from January 1, 2022, to January 15, 2022. We can find that most measured relative humidity are included in the predicted 2 $\boldsymbol{\sigma}$ confidence interval (see Figure 4-3).

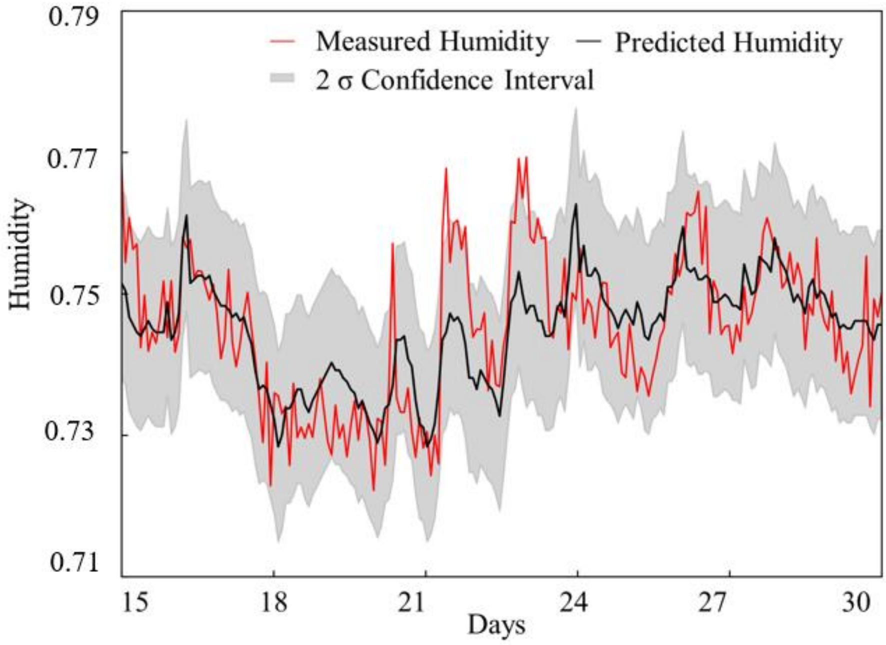


Figure 4-3 Comparison of measured relative humidity and predicted relative humidity (Channel 4 January)

Besides, a different month was chosen. The Gaussian Process model was trained by the data from August 1, 2022, to August 15, 2022. We can find that most measured relative humidity was included in the predicted 2 $\boldsymbol{\sigma}$ confidence interval and the Gaussian Process model predicted the huge drop of the relative humidity on August 20 (see Figure 4-4).

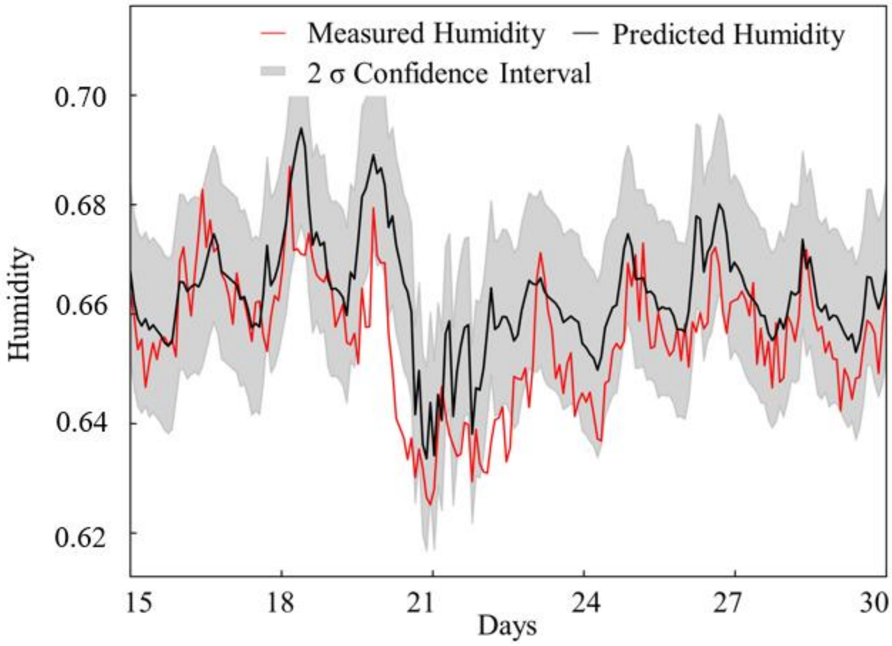


Figure 4-4 Comparison of measured relative humidity and predicted relative humidity (Channel 1 August)

## 4.4 Conclusions

GP excels in modelling complex nonlinear relationships. In field applications, installed sensors will be offline during maintenance work. This study demonstrates the potential of GP models to address this gap. A GP model was trained using relative humidity data from the embeddable FBG-based sensing system for monitoring relative humidity and ambient relative humidity and temperature data sourced from and Automatic Weather Buoy No. 2 (Hong Kong International Airport, West), operated by the Hong Kong Observatory.

The results indicated that the GP model provided a viable method for estimating in-beam relative humidity using external meteorological data. The GP model's probabilistic framework provided predictions with quantified uncertainty (90% confidence levels), which consistently encapsulated the majority of measured relative humidity across multiple channels and seasonal conditions. Notably, the model captured abrupt relative humidity changes, such as the sharp decline observed in August 2022, underscoring its robustness in modeling nonlinear relationships under varying environmental conditions.

At the same time, this GP model has some limitations. First, each sensor needs to train its own GP model based on its historical data, rather than using the same model. In addition, a long prediction interval can also increase the error in the model's predictions. For example, predicting results one year ahead can result in significant errors.

Overall, this study highlights the potential of machine learning, particularly Gaussian Process, in fiber optic sensing system data analysis. This capability is particularly valuable for field applications for reliable predictions during sensor maintenance or outages.

# CHAPTER 5. DEVELOPMENT OF AN EMBEDDABLE FLUORESCENCE-BASED SENSOR FOR MONITORING CHLORIDE INSIDE CONCRETE

## 5.1 Introduction

Coastal concrete structures are increasingly influenced by chloride penetration from the marine environment. This phenomenon can compromise the protective passive film on steel reinforcement, accelerate corrosion, and significantly shorten the service life of concrete infrastructure. Monitoring chloride ions inside concrete structure can warn rebar corrosion in advance, thereby ensuring the safety of the concrete structure.

In recent years, fiber optic sensing system has garnered significant attention for monitoring chemical parameters inside concrete structure due to its distinct advantages including ability to monitor parameters remotely, ability to achieve real-time monitoring, small size, immune to EMI, resistance to water and corrosion, and ability to be multiplexed.

Fluorescence-based sensors operate on the principle of measuring variations in the intensity of excited and emitted fluorescence signals. Fluorescence is the light emitted by an atom or molecule after the absorption of electromagnetic energy. The fluorescence arises from the transition of the excited species from its first excited electronic singlet level to its ground electronic level. Quenching refers to the decrease of the fluorescence intensity of a sample. The quenching process can be described using the Stern-Volmer equation:

$$\frac{I_0}{I} = 1 + K_s[Q] \tag{5-1}$$

In the equation, $I_0$ is the initial fluorescence intensity in the absence of a specific ion. $I$ is the fluorescence intensity in the presence of a specific ion. $K_S$ is the Stern–Volmer constant. [Q] is ion concentration. With this equation, the interaction between fluorescence intensity and analytes can be established.

Based on Stern-Volmer equation, in this chapter, an embeddable fluorescence-based sensor for monitoring chloride inside the concrete was developed. Then the performance of the sensor was evaluated through a series of tests, including tests in chloride solutions, in concrete simulation solutions with different pH values, in solutions containing diverse ions for selectivity assessment, in mortar specimens, and in high humidity environmental chamber.

## 5.2 Experimental Design

### 5.2.1 Development of an embeddable fluorescence-based sensor for monitoring chloride inside concrete

*5.2.1.1 Design of the fluorescence-based sensor for monitoring chloride*

In the schematic of the fluorescence-based sensor for monitoring chloride, (see Figure 5-1) the laser from laser source, emitting the fluorescence of the material inside the sensor probe through a Y- type multimode fiber. Nylon film and the glass pieces are used to protect the fluorescent polymer inside the sensor housing. The other end of the Y-type fiber is connected to the spectrometer. Fluorescence intensity exhibits a direct correlation with chloride concentration, enabling quantitative measurement through spectral data captured by the spectrometer.

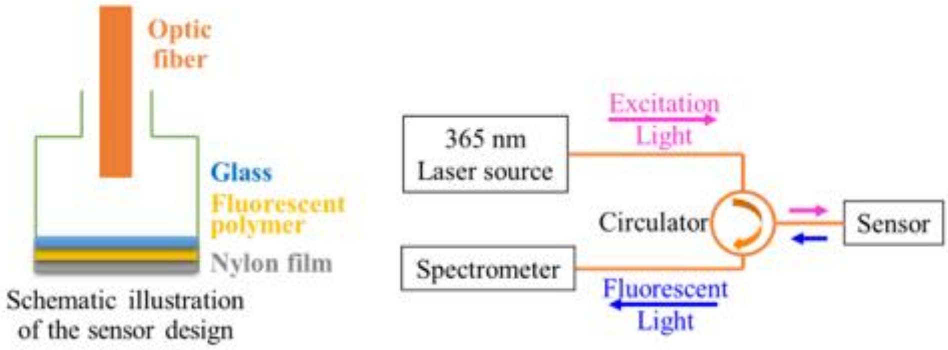


Figure 5-1 Schematic of fluorescence-based sensor for monitoring chloride

*5.2.1.2 Selection of chloride sensitive fluorescent material*

In this study quinine sulphate is selected as the sensing material. Quinine was first isolated in 1820 from the bark of a cinchona tree, which is native to Peru, and its molecular formula was determined by Strecker in 1854. The class of chemical compounds to which it belongs is thus called the cinchona alkaloids. Figure 5-2 shows the structure of quinine. Quinine has been used extensively in fluorescence studies, due to its stability in aqueous solutions, stable at low pH, and broad, structureless absorption and emission. Its utility in fluorescence quenching investigations, particularly by halides via nonfluorescent complex formation between the quinine and halide ions (Verity et al. 1996), has been well-documented. Quinine sulphate is a quinoline-derived chloride indicator with dual excitation wavelengths (250 nm and 350 nm), and emission peaks (450–500 nm) (Jayaraman et al. 2000). Thus, in this study, quinine sulphate was chosen as the fluorescent indicator for chloride monitoring.

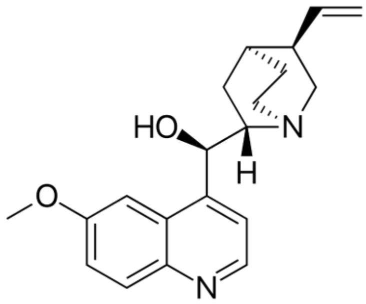


Figure 5-2 Structure of Quinine

*5.2.1.3 Preparation of chloride-sensitive fluorescent film*

For better fixation of fluorescent material in the sensor probe, in this work, a utilized sol-gel technology to embed quinine sulphate effectively within a solid matrix. The sol-gel technology applied in this study comprised a volumetric ratio of tetraethyl orthosilicate (TEOS) to anhydrous ethanol and hydrochloric acid (0.01 M) of 4.9:8:1.6, respectively. The quinine sulphate solution was $4 \times 10^{-3}$M and supplemented with formamide at a volumetric ratio of 15%. The sol-gel process is listed below:

Step 1: Preparation of quinine sulphate solution. The solution was prepared by mixing 2055 μL of tetraethyl orthosilicate, 3285 μL of anhydrous ethanol, 500 μL of 0.01 M hydrochloric acid, 800 μL of $5 \times 10^{-2}$M quinine sulphate solution, and 1260 μL of formamide. At room temperature, a magnetic stirrer was used to stir the solution for two hours.

Step 2: Dry the solution on a quartz piece. After 24 hours of resting, with weakened fluidity of the solution, the solution was spin-coated on a quartz piece. The speed was set at 600 rpms, and the spin-coating progress took thirty seconds. Then the s0l was cured for one hour at 50 ℃.

Since the total volume of the prepared solution was 10 mL, the hydrochloric acid solution was low enough to be ignored.

*5.2.1.4 Preparation of sensor housing with 3D printing*

The sensor housing is fabricated with 3D printing technology. 3D printing technology is a transformative digital fabrication technology which can serve as a valuable tool for producing customized equipment and functional components for engineering applications. This innovative approach enables the creation of intricate prototypes through a layer-by-layer additive process, contrasting with traditional subtractive manufacturing methods that remove material from bulk stock (Noorani 2018). The defining feature of 3D printing lies in its ability to construct physical objects sequentially, depositing material one layer at a time. This precision facilitates the fabrication of embeddable sensor housings that conform precisely to the geometry of complex structures (Manzanares Palenzuela et al. 2018). Owing to its reproducibility, user accessibility, and adaptability, 3D printing is particularly suited for fabricating sensor housing suitable for variably shaped concrete structures and integrating them seamlessly into sensing system for monitoring chemical parameters.

The 3D printing process typically involves the use of liquid, powdered, or solid materials to fabricate objects. The workflow comprises five key stages (Noorani 2018):

Design: In this stage, a digital model of the object is created using computer-aided design (CAD) software. For SHM applications, this stage often involves optimizing geometries to embed sensors within structural components or designing lightweight, high-strength housing resistant to environmental degradation.

Conversion: The CAD file is exported into stereolithography (STL) format, which approximates the 3D geometry using interconnected triangular facets. Each facet is defined by vertex coordinates and the surface normal.

Slicing: The STL file is segmented into 2D cross-sectional layers using specialized software. Parameters such as orientation, scale, and layer thickness are adjusted based on printer specifications.

Fabrication: The 3D printer constructs the object layer by layer. Modern systems often operate autonomously once they are initiated.

Post-Processing: The prototype is removed from the printer, cleaned, and subjected to finishing procedures. These may include post-curing of photopolymers, sintering of powdered materials, removal of support structures, and surface treatments (e.g., sanding, sealing, or painting) to achieve desired functional or aesthetic properties. For monitoring chemical parameters inside concrete, post-processing may also involve calibrating embedded sensors or applying protective coatings to enhance durability in harsh environments.

A Sub-Miniature Version A (SMA) connector was printed in the upper part of the sensor housing. The lower part was an O shape holder, holding the quartz pieces with sensing film. The probe's bottom allows direct contact between the environment and the sensing film (Figure 5-3). All parts are protected by waterproof glue.

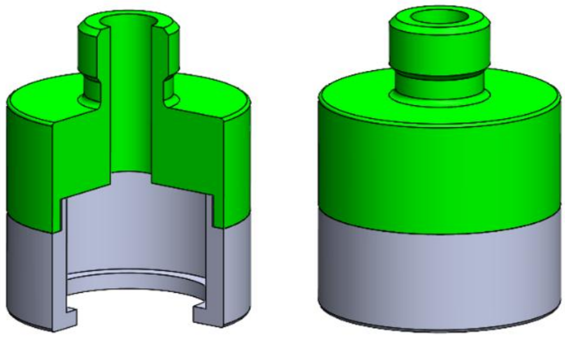

Figure 5-3 Sensor housing design

## 5.2.2 Tests in chloride solutions

The response of the developed sensors to chloride solutions was tested as follows: (1) Put the developed fluorescence-based chloride sensors into different concentrations of NaCl solution. The concentration gradient was set to 0.01 M, with a starting concentration at 0 M. (2) Record the fluorescence intensity from the spectrometer. (3) Analysis the data with computer.

## 5.2.3 Tests in concrete simulation solutions with different pH values

To explore the performance of the developed sensors in concrete, tests in concrete simulation solutions with different pH values were carried out in this chapter.

$Ca(OH)_2$ powder and $NaHCO_3$ standard solution was applied in these tests to configure concrete simulation solutions. The first step was preparing supersaturated $Ca(OH)_2$ by adding excess $Ca(OH)_2$ powder to deionized water. Then left the supersaturated solution to stand after 24 hours. The upper layer of the supersaturated solution was extracted as the concrete simulation solution. The pH value of the saturated

$Ca(OH)_2$ solution was 12.6. By adding $NaHCO_3$ at a concentration of 1M drop by drop, the pH value of the simulation solution was adjusted to pH values of 11.6, 10.6, 9.6, and 8.6.

### 5.2.4 Ion selectivity tests

Ion selectivity is a unique advantage of fluorescence-based sensors. To validate the ion selectivity, in this experiment, ions including $SO_4^{2-}, NO_3^-, HPO_4^{2-}, CO_3^{2-}, SiO_3^{2-}, Na^+, Ca^{2+}$ and $Mg^{2+}$, were selected. The ratio of fluorescence burst $\frac{I_0 - I}{I}$ was used to define the degree of influence of the added ions on the fluorescence intensity of quinine sulphate. $I_0$ is the initial fluorescence intensity and I is the fluorescence intensity after putting the sensor probe into the ion solution. A control experiment was conducted using deionized water.

The concentration of the interfering ions in the solution was 100 μg/mL, and the concentration of chloride ions was 10 μg/mL.

### 5.2.5 Tests in cement mortar specimens

The internal environment of the concrete structure is complex. In this experiment, tests are carried out to study the response of the developed fluorescence-based chloride sensors inside the cement mortar specimens to figure out whether the sensor can survive when being embedded in concrete, to test the long-term performance of quinine sulphate Sol-gel membrane inside the sensor probe, and to study the impact of different water-cement ratios on the chloride penetration in cement.

*5.2.5.1 Preparation of cement mortar samples*

The sensors used in this experiment were the fiber optic fluorescence-based sensors for monitoring chloride developed in Chapter 5.2.1. Cement mortar specimens of different heights and different water-cement ratios were prepared to study the effects of different water-cement ratios on chloride ion corrosion of concrete structures and sensor performance. Sensors were installed on the top of cement mortar specimens (see Figure 5-4) with different heights and different water/cement ratios (0.3, 0.4, 0.5). Monitoring depts were the depts from the sensor probe bottom to the specimen bottom, and the monitoring depts were 2 mm, 4 mm, 8 mm,15 mm, 20 mm. The specimens were 30 mm long by 30 mm wide. Control groups without sensors were prepared for chloride measurement as well. A conventional method was applied to gain chloride concentration. All specimens were cured for 28 days. Figure 5-5 shows the mortar specimens after demolding. All the specimens were sealed with epoxy resin except the bottom. Epoxy resin layers ensure unidirectional penetration of the chloride ions.

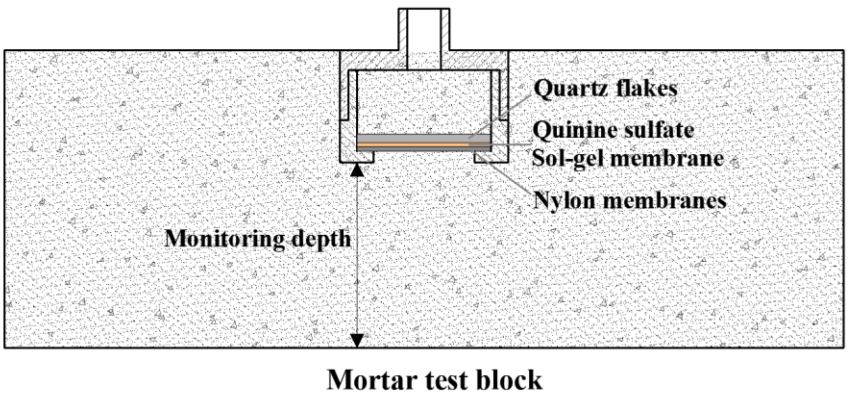


Figure 5-4 Schematic of mortar specimens with embedded fluorescence-based sensors for monitoring chloride

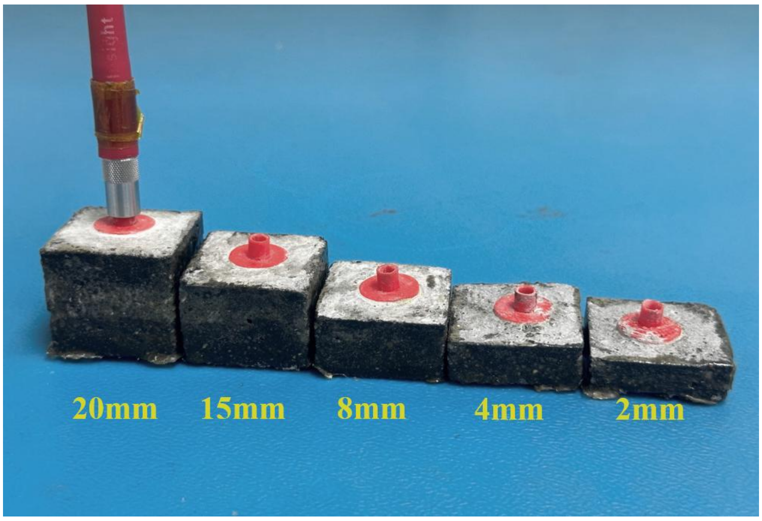

Figure 5-5 Mortar specimens after demolding

*5.2.5.2 Experimental setup*

The natural penetration method is one of the most common methods in the study of chloride ion corrosion of concrete structures. This method is simple to operate and easy to simulate the environment. Considering the size of the test specimens, the corrosion depth, and the test cycle, the natural penetration method was used in this study. In this test, all mortar specimens were placed in the same chloride solution with a constant temperature of 25°.

To ensure consistent nature penetration, a test stand was designed and manufactured with 3D printing technology to ensure stable contact conditions of all test specimens with the chloride solution.

Figure 5-6 shows the mortar specimens in the test stand. The test blocks were placed in each slot of the test stand to be suspended above the sodium chloride solution. Only the bottom of the test specimens was in contact with the solution. The sides of the test specimens were sealed with epoxy resin to avoid chloride penetration. The sodium chloride solution was set to 3%. During the test, the entire device was in a sealed state and was only opened when carrying out fluorescence intensity monitoring tests. During the experiment, in order to prevent the water level from falling below the erosion surface of the test block, the experimental container was regularly replenished with 3% sodium chloride solution. Three sets of mortar blocks with different monitoring depths were prepared.

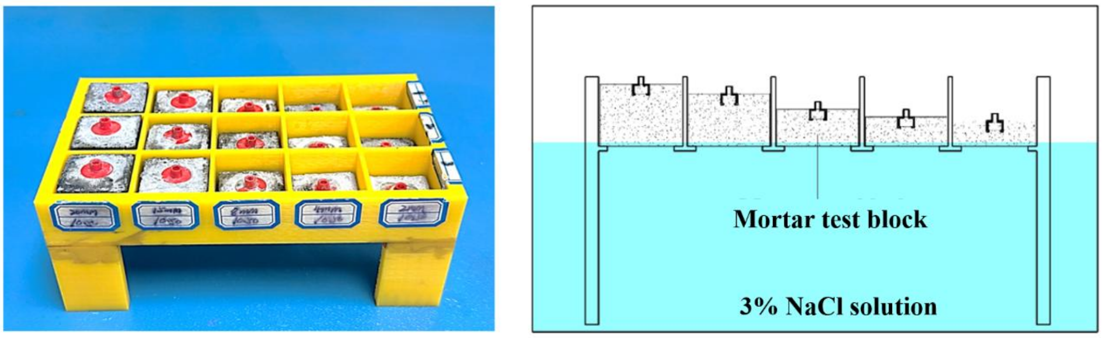


Figure 5-6 Mortar specimens in the test stand

*5.2.5.3 Data collection*

The fluorescence intensity of the sensor embedded inside the mortar specimens was monitored and recorded. The chloride ion concentration was calculated by the equation in previous experiment.

After the mortar specimens being placed inside the test stand, the fluorescence intensity of the sensors embedded in each test block was recorded and the initial fluorescence intensity recorded was set as the $I_0$. The test was carried out for 30 days. During the test, all blocks were immersed in 3% sodium chloride solution. Uninterrupted testing was carried out for the first 7 days of the test, during which, fluorescence spectra of test blocks with different water-cement ratios and different monitoring depths was recorded every day. After 7 days, the fluorescence intensity was collected on the 10th, 15th, 20th, 25th, and 30th days of the test.

For controlled groups, the chloride ion concentration of specimens without sensors was tested by potentiometric titration. Destructive experiments were carried out on the 10th, 20th and 30th days, and the test blocks were ground layer by layer using a layered grinder along the eroded end surface. The powder at depths of 2~3, 4~5, 8~9, 15~16 and 20~21 mm was taken. Potentiometric titration method was applied to gain the chloride ion content in the powder.

### 5.2.6 Tests in high humidity chamber

The extreme environmental conditions on-site challenge sensor's durability and functionality. This study examines the developed sensors when being embedded within concrete beams and placed in a high humidity environmental chamber. In these tests, the sensors were embedded inside FRP reinforced SWSSC beams (dimensions: 1600 mm × 190 mm × 140 mm) (Figure 5-7), and the beams were placed inside an environmental chamber (see Figure 5-7).

(a) (b)

Figure 5-7 (a) Environmental chamber and the beams (b) Fluorescence-based sensors for monitoring chloride embedded in FRP reinforced SWSSC beams

The sensors were fixed near the FRP bar before casting. The fixed sensors and FRP bar size were shown in Figure 5-8. Stirrup diameter was 6 mm, clear cover to stirrups was 15 mm, and depths of the sensor were set at 65mm, 95mm, and 125mm to avoid contacting each other.

The temperature inside the environmental chamber was set at 20 ℃. The relative humidity inside the environmental chamber was set at 40% at first. After 9 months, the relative humidity inside the environmental chamber was set at 100%.

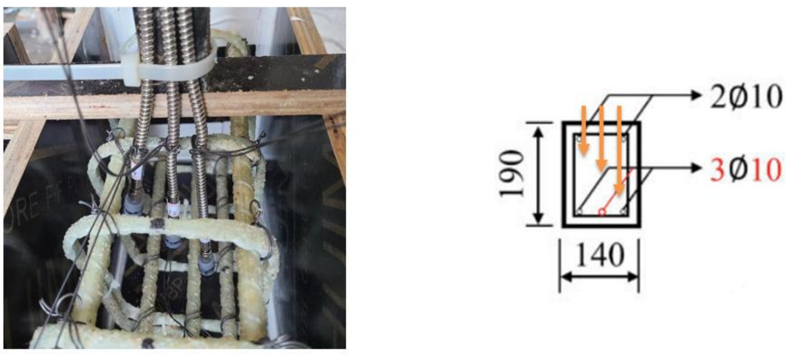


(a) (b)

Figure 5-8 (a) Fixed sensors (b) FRP bar size and sensor location

## 5.3 Results and Discussion

### 5.3.1 Response of the fluorescence-based sensor for monitoring chloride in chloride solutions

The experimental data demonstrates a consistent reduction in quinine sulphate's fluorescence emission as chloride ion concentrations rise, with observable effects initiating at NaCl levels as low as 0.01 M (see Figure 5-9). The quenching of quinine sulphate was saturated when the test concentration reached 0.07 M, due to the limited amount of quinine sulphate in the sensing material.

A linear regression analysis of the calibration dataset performed using the Stern–Volmer law, established the correlation between chloride concentration and fluorescence attenuation. The calibration curve (see Figure 5-10) shows the inverse proportionality of quinine sulphate's luminescent response to chloride content, and the corresponding calibration equation is:

$$\frac{I_0}{I} = 1 + 17.646[Cl^-] \quad (5\text{-}2)$$

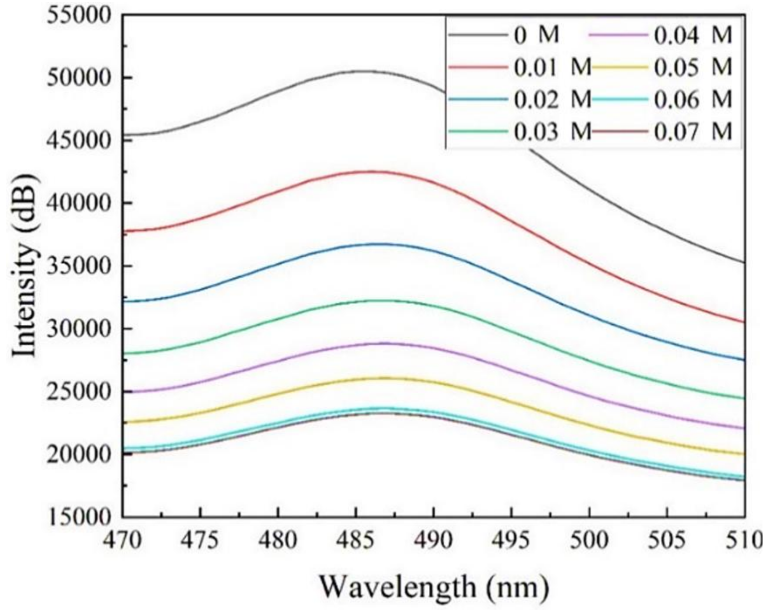


Figure 5-9 Fluorescent intensity of quinine sulphate under different NaCl concentration

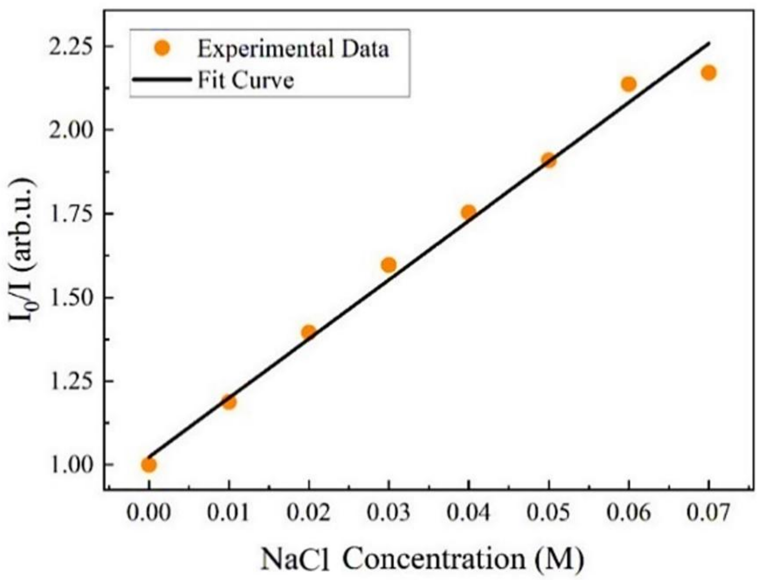


Figure 5-10 Calibration curve of $I_0/I$ to chloride concentration

### 5.3.2 Response of the fluorescence-based sensor for monitoring chloride in concrete simulation solution with different pH values

The test data were linearly fitted with different chloride concentrations and fluorescence intensities according to the Stern–Volmer equation. Figure 5-11 shows the K values and standard curve of the sensor in the concrete simulation at different pH values. The standard equations at each pH are as follows:

$$\frac{I_0}{I} = 1 + 17.506[Cl^-]\ pH = 8.6 \tag{5-3}$$

$$\frac{I_0}{I} = 1 + 17.459[Cl^-]\ pH = 9.6 \tag{5-4}$$

$$\frac{I_0}{I} = 1 + 17.444[Cl^-]\ pH = 10.6 \tag{5-5}$$

$$\frac{I_0}{I} = 1 + 17.306[Cl^-]\ pH = 11.6 \tag{5-6}$$

$$\frac{I_0}{I} = 1 + 17.149[Cl^-]\ pH = 12.6 \tag{5-7}$$

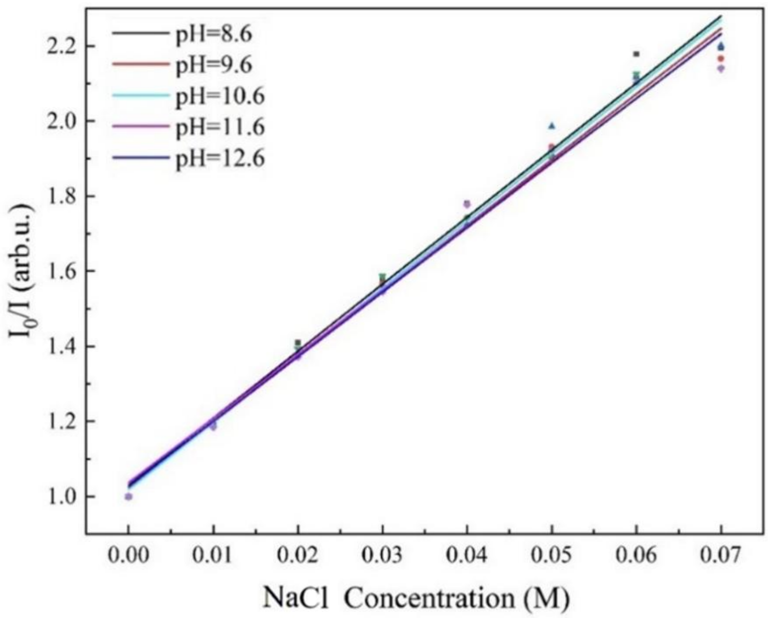


Figure 5-11 Response of fluorescence-based sensor for monitoring chloride in concrete simulation solutions with different pH values

The sensor exhibited consistent detection performance, with its response coefficient (k-value) showing minimal variation across measurements. This operational stability closely matched the original calibration benchmark of k = 17.646, confirming measurement reproducibility. The system's design enables effective chloride ion quantification in simulated concrete pore solutions, demonstrating functional reliability across alkaline conditions ranging from pH 8.6 to 12.6.

### 5.3.3 Results of ion selectivity tests

Figure 5-12 shows results of the ion selectivity tests of the developed fluorescence-based sensor for monitoring chloride. The fluorescence burst ratios of $SO_4^{2-}$, $NO_3^-$, $HPO_4^{2-}$, $SO_4^{2-}$, $NO_3^-$, $HPO_4^{2-}$, $CO_3^{2-}$, $SiO_3^{2-}$, $Na^+$, $Ca^{2+}$and $Mg^{2+}$ were 0.0247, 0.0114, 0.0123, 0.0217, 0.0079, 0.0108, -0.0161, 0.0141 and 0.0072 for the blank group. These values are much smaller than the fluorescence burst ratio of 0.1413 for $Cl^-$. The experimental design accounted for fluorescence attenuation caused by solvent-induced dilution in the control group (deionized water), which exhibited a minimal quenching coefficient of 0.0072. To evaluate interference effects, competing ions $SO_4^{2-}, NO_3^-, HPO_4^{2-}, CO_3^{2-}, SiO_3^{2-}, Na^+, Ca^{2+}$ and $Mg^{2+}$ were introduced at concentrations tenfold higher than chloride ions. Analytical results confirmed the negligible influence from these species on the $Cl^-$. specific fluorescence quenching mechanism of quinine sulphate. These findings underscore the sensor's exceptional selectivity for chloride detection and its capacity to maintain accuracy in complex ionic matrices. The embeddable fiber optic chloride sensor thus demonstrates both high specificity for $Cl^-$ and robust anti-interference performance under tested conditions.

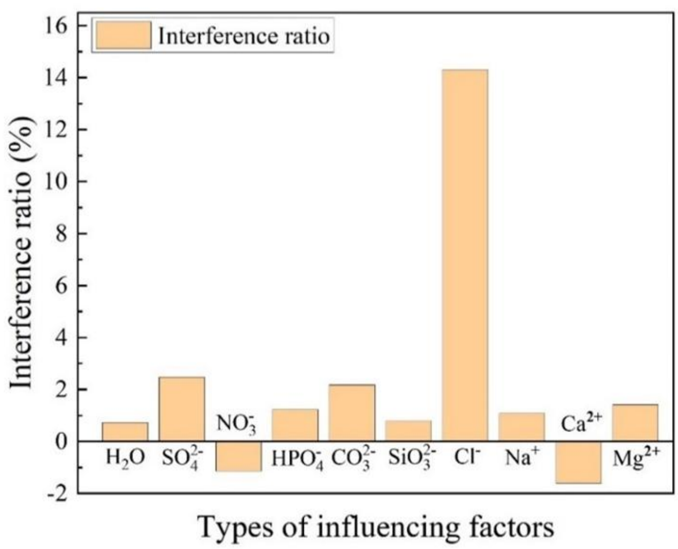


Figure 5-12 Results of ion selectivity tests

### 5.3.4 Response of the fluorescence-based sensor for monitoring chloride in cement mortar specimens

*5.3.4.1 Response of the fluorescence-based sensor for monitoring chloride in specimens with different heights and different water/cement ratio*

As illustrated in Chapter 5.2.5.2, the sensors were embedded at the top the specimens of different heights, thus the bottom of the sensor to the bottom of the specimen has different depts. The penetration rate at 2 mm and 4 mm depths was faster compared with the rate at the other depths. After the 20th day, the chloride concentration was reduced (see Figure 5-13, Figure 5-14 and Figure 5-15). The rise in the concentration of chloride ions at different depths correlates with the increase in the water/cement ratio.

The following mechanism may have contributed to the above results. During the chloride ion penetration process, a portion of the free chloride ions diffuses into concrete along with the pore fluid, while the other portion of the free chloride ions bind to the hydration products in the concrete. This phenomenon is called the chloride ion binding effect. In fact, due to the high chloride ion concentration difference in the early stage, free chloride ions penetrated rapidly in shallow areas at depths of 2 mm and 4 mm. For a specific concrete specimen, there is a maximum chloride ion binding capacity. Under this limit, the higher the chloride ion concentration in the pore solution, the more opportunities for chloride ions to enter the binding sites, and the higher the chloride ion binding strength. Thus, until the 20th day, there was a decrease in the chloride ion concentration. With the increase in depth, the penetration rate decreased significantly. At a depth of 8 mm, the chloride ion concentration decreased earlier than that in the shallow depth area. At a depth of 15 mm and 20 mm, because the chloride ion concentration was very low and the chloride ion binding strength was very low, the chloride ion concentration continued to increase slowly (Yuan et al. 2009; Dhir et al. 1994). It can be seen that the sensor can sense the changes in chloride ion concentration inside the concrete structure and monitor the chloride ion concentration in real time.

Cementitious materials demonstrate a proportional relationship between their water-cement ratio and both chloride migration depth and accumulation. Reduced water-cement ratios diminish key pore structure metrics including maximum and critical pore dimensions. Thus, improving the material's ability to inhibit chloride ingress (see Figure 5-13, Figure 5-14, and Figure 5-15). As the water-cement ratio of the test block increases, the chloride ion concentration at the same depth increases, indicating that the sensor can still monitor the chloride ion concentration in concrete structures with different water-cement ratios and sense the changes in chloride ion concentration.

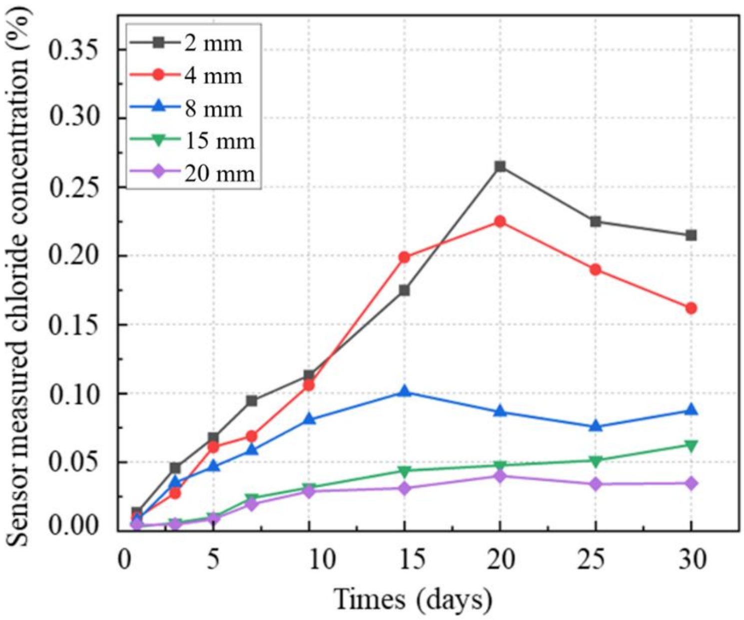


Figure 5-13 Sensor-monitored chloride concentrations (w/c ratio: 0.3)

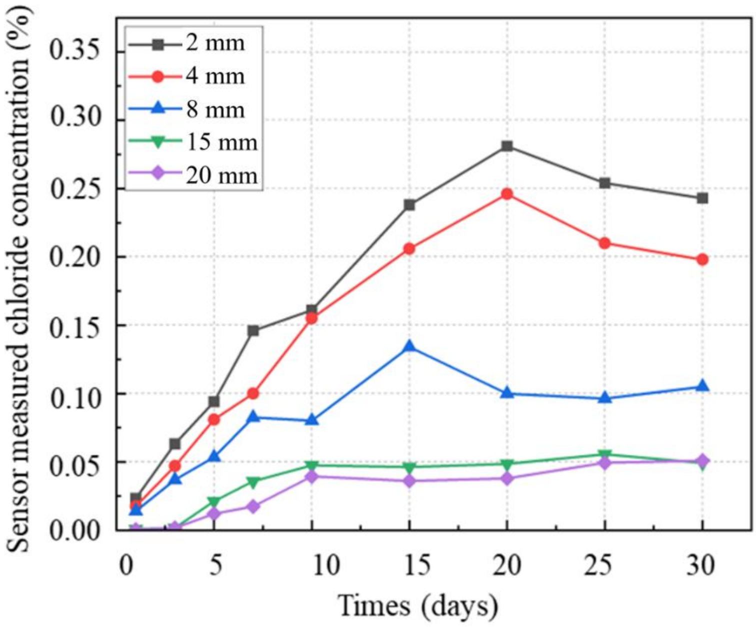


Figure 5-14 Sensor-monitored chloride concentrations (w/c ratio: 0.4)

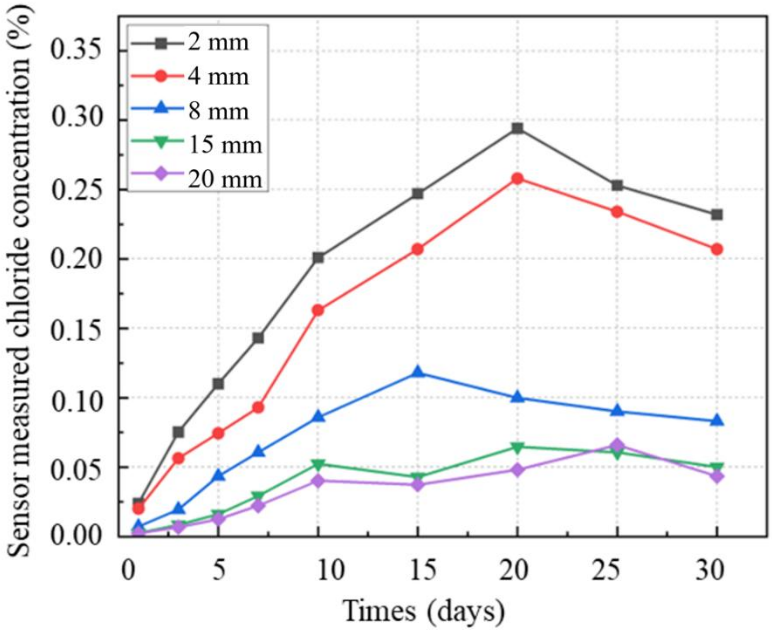


Figure 5-15 Sensor-monitored chloride concentrations (w/c ratio: 0.5)

*5.3.4.2 Comparison of results from developed sensors to results from the control groups*

From the comparison of results from developed sensors to results from the control groups at 10th day, 20th day and 30th day with different water/cement ratios, sensor-measured chloride levels typically register lower values compared to those obtained through potentiometric titration, with the disparity between free and total chloride concentrations diminishing progressively with greater penetration depth (see from Figure 5-16 to Figure 5-24). This divergence stems from methodological differences. Potentiometric titration quantifies total chloride content in control samples, whereas the fluorescence-based sensor specifically detects unbound chloride ions. During cement hydration processes, mobile chloride ions chemically interact with hydration products, forming bound chloride complexes. As chloride migration progresses through the material matrix, the progressive depletion of unbound chlorides creates measurable discrepancies between detection methods.

Near-surface regions exhibit elevated chloride accumulation, enabling greater ionic interaction with reactive binding sites in the cementitious matrix. This enhanced surface-level reactivity produces significant variance between free and total chloride measurements. With increasing depth, reduced chloride availability limits ion-binding opportunities and correspondingly decreases method divergence.

The observed depth-dependent concentration gradients illustrate the competitive equilibrium between chloride mobility and immobilization mechanisms within the concrete microstructure. These findings emphasize the importance of detection methodology selection based on whether assessing active corrosion potential (free ions) or cumulative salt ingress (total content). The sensor's capacity to isolate free chloride concentrations confirms its utility in evaluating real-time corrosion risks.

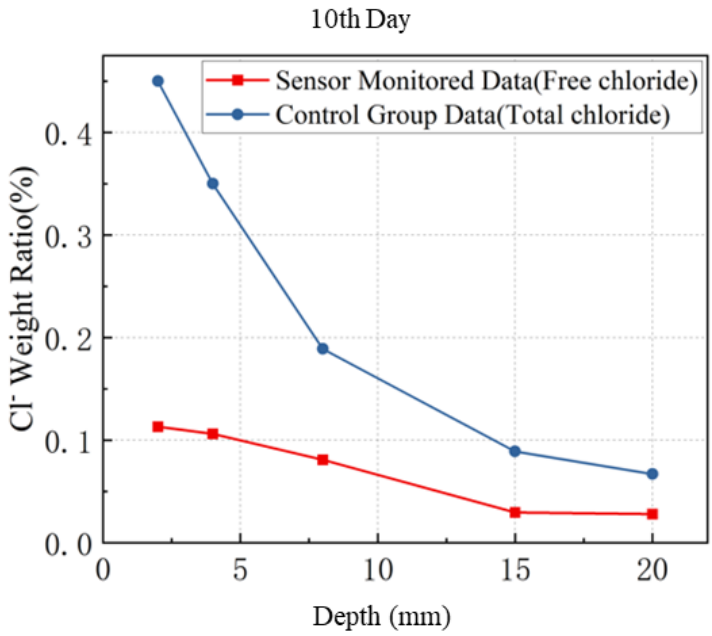


Figure 5-16 Results comparison of sensor-monitored to control groups (w/c ratio: 0.3 10th Day)

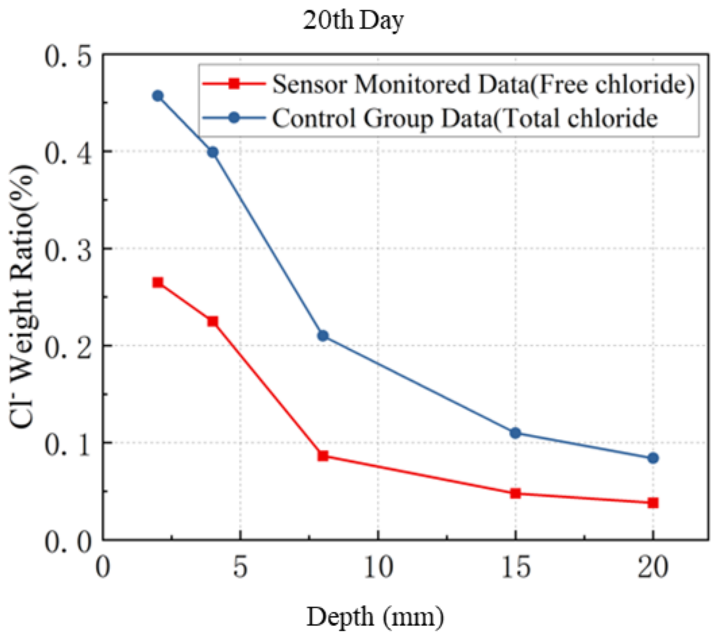


Figure 5-17 Results comparison of sensor-monitored to control groups (w/c ratio: 0.3 20th Day)

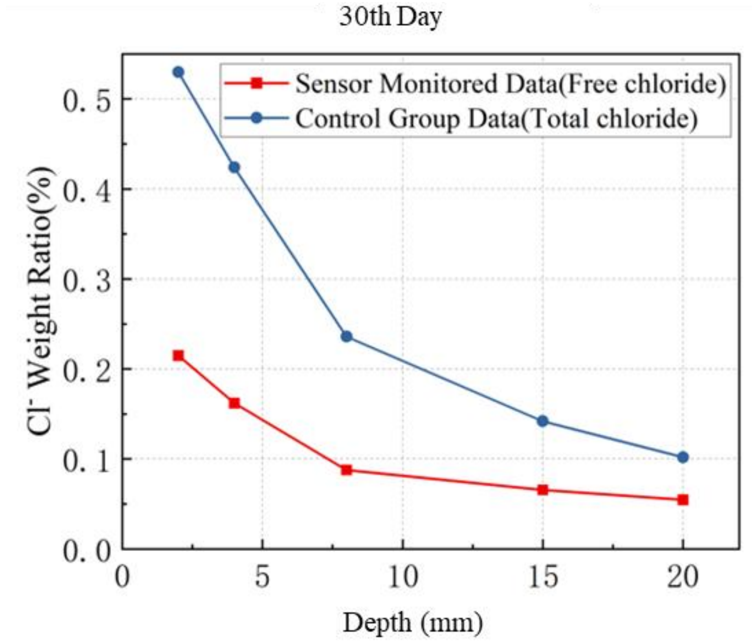


Figure 5-18 Results comparison of sensor-monitored to control groups (w/c ratio: 0.3 30th Day)

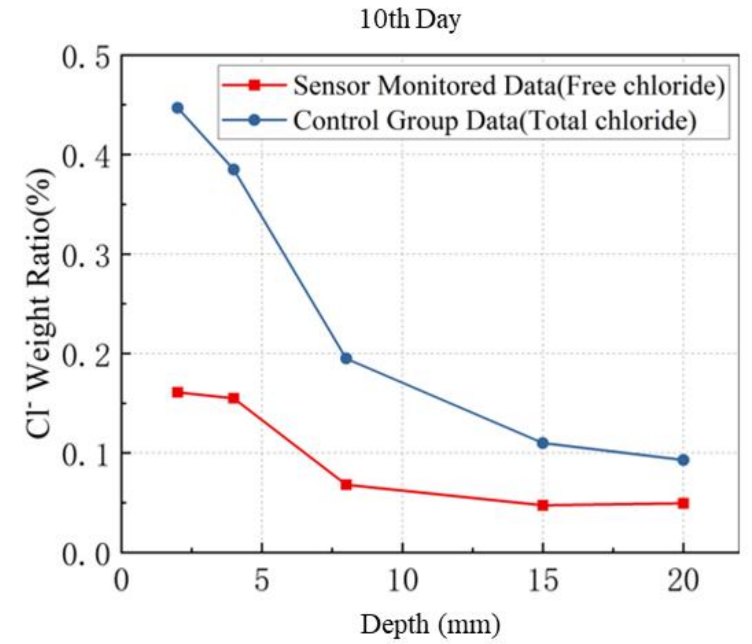


Figure 5-19 Results comparison of sensor-monitored to control groups (w/c ratio: 0.4 10th Day)

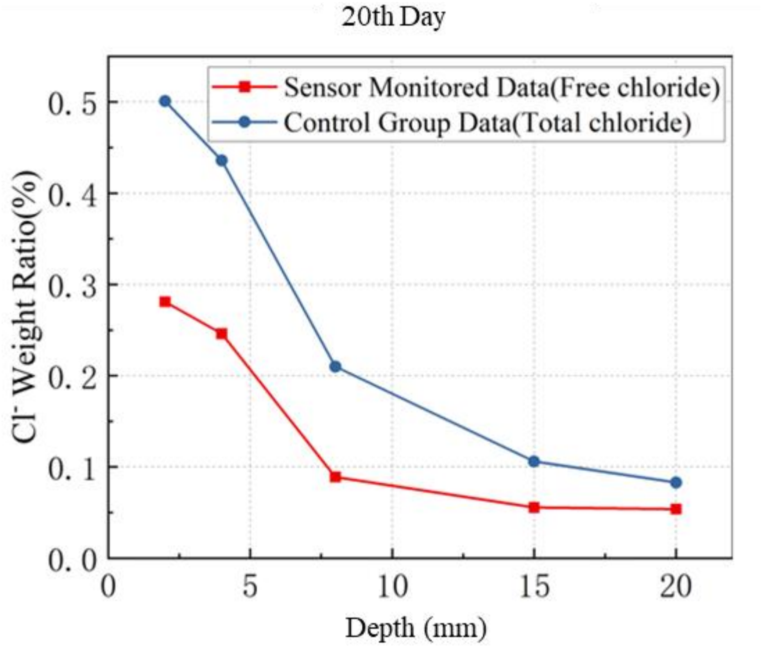


Figure 5-20 Results comparison of sensor-monitored to control groups (w/c ratio: 0.4 20th Day)

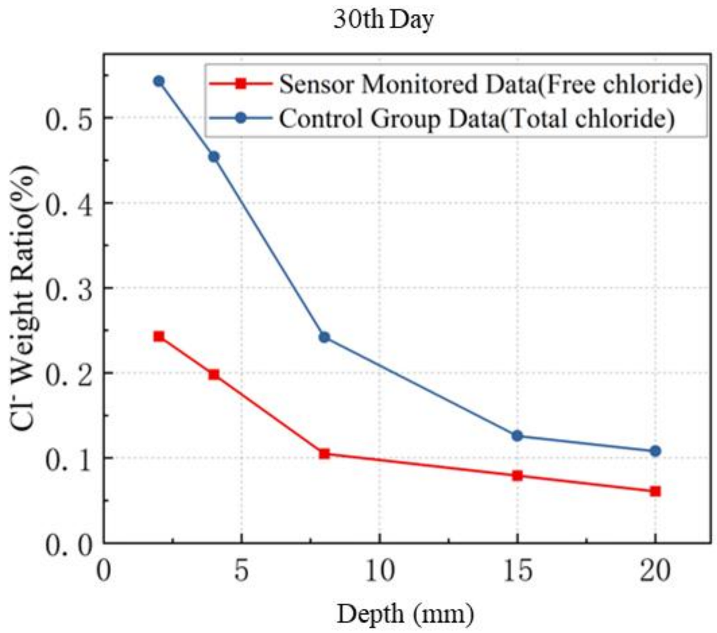


Figure 5-21 Results comparison of sensor-monitored to control groups (w/c ratio: 0.4 30th Day)

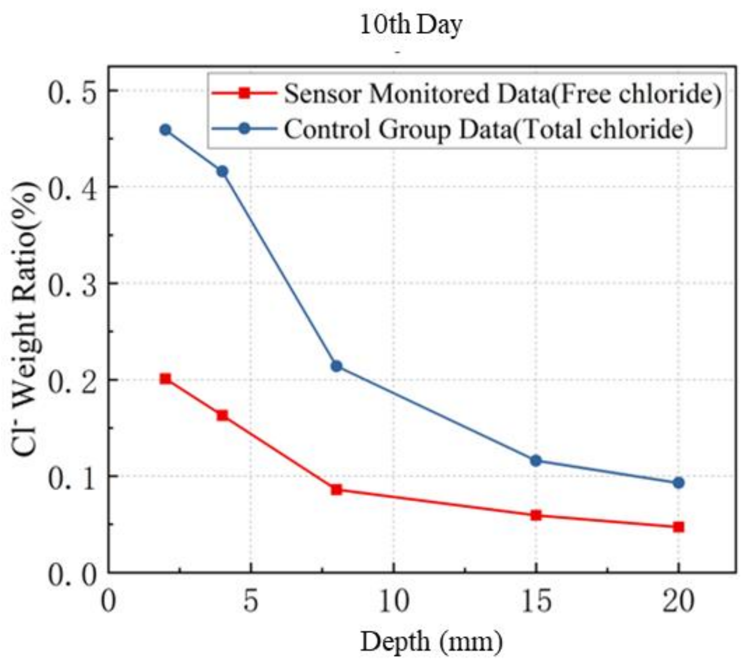


Figure 5-22 Results comparison of sensor-monitored to control groups (w/c ratio: 0.5

10th Day)

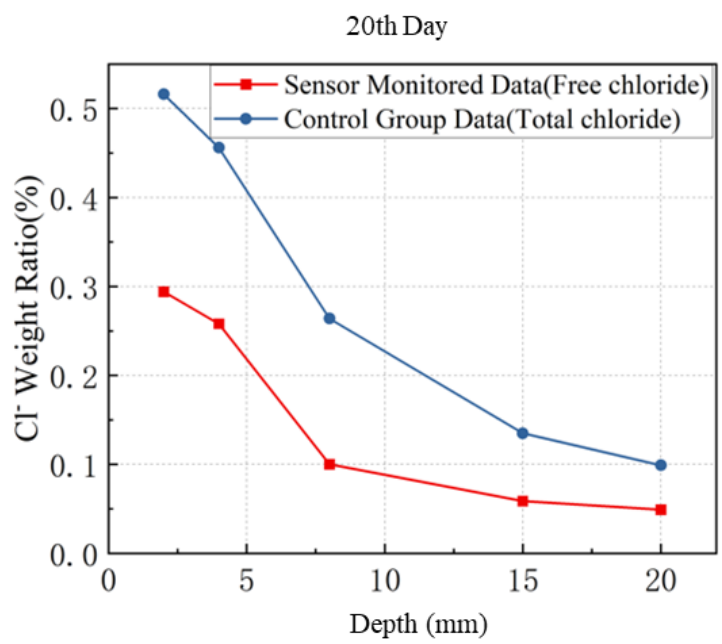


Figure 5-23 Results comparison of sensor-monitored to control groups (w/c ratio: 0.5

20th Day)

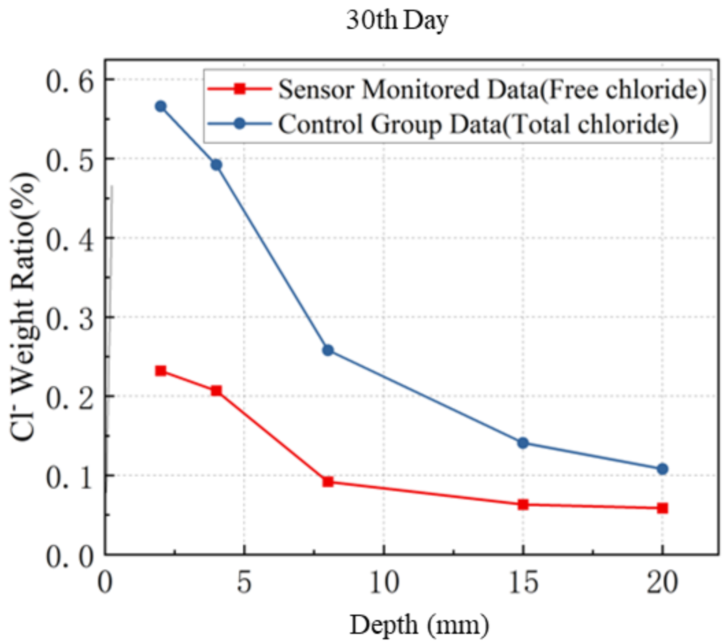


Figure 5-24 Results comparison of sensor-monitored to control groups (w/c ratio: 0.5 30th Day)

*5.3.4.3 Sensitive depths of the fluorescence-based sensor for monitoring chloride*

The actual depth of chloride erosion was determined by using potentiometric titration for different depths of the same test specimen when the sensor sensed the presence of chloride ions. Taking the monitoring depth of 2 mm as an example, when the sensor embedded at 2 mm sensed chloride ions, the depths of sensor were set as $d_t = 2mm$, and the actual depth of chloride erosion was measured by potentiometric titration with grinded powder from different depths of the blank specimens with same size and water/cement ratio.

Actual depths obtained with potentiometric titration method were taken to be the reference value $d_0$. The depths of sensor were set as $d_t$. The difference between the two depths ($P_d = |d_t - d_0|$) can be used as a reference of sensitive depths. From Table 5-1 it can be found that the sensor's sensitive depths were better than 3 mm.

Table 5-1 Sensitive depths of fluorescence-based sensor for monitoring chloride in mortar specimens

| $d_t$ (mm) | $d_0$ (mm) | $P_d = \lvert d_t - d_0 \rvert$ (mm) |
|---|---|---|
| 2 | 3.3 | 1.3 |
| 4 | 3.3 | 0.7 |
| 8 | 6.3 | 1.7 |
| 15 | 16.7 | 1.7 |
| 20 | 17.3 | 2.7 |

#### *5.3.4.4 Chloride concentration sensing accuracy*

The chloride concentration inside the specimens with 30 days natural penetration obtained from the developed sensor is set as $C_m$ which is the free chloride concentration monitored. The results from the specimens with 30 days natural penetration using potentiometric titration method are set as $C_p$. The chloride concentration from potentiometric titration is total chloride concentration and total chloride concentration $C_p$ includes free chloride $C_f$ and bound chloride $C_b$. In the previous research carried out by Feng and Mohanmmed (Feng et al. 2012; Mohammed et al. 2003), in natural penetration test, the relationship between free chloride $C_f$ and bound chloride $C_b$ meets Langmuir isotherm:

$$C_b = \frac{1.11C_f}{1 + 23.6C_f} \tag{5-8}$$

Thus the free chloride $C_f$ can be calculated with:

$$23.6C_f^2 + (2.11 - 23.6C_p)C_f - C_p = 0 \tag{5-9}$$

The monitoring results of the specimens with different water/cement ratios showed that the sensing accuracy for chloride concentration was better than 80% when the depth is larger than 20 mm. (see Figure 5-25, Figure 5-26 and Figure 5-27).

Table 5-2 Monitoring results of the specimens with water/cement ratios: 0.3

| **Depth(mm)** | $C_m$**(%)** | $C_p$**(%)** | $C_f$**(%)** | **Accuracy** $C_m/C_f$ **(%)** |
|---|---|---|---|---|
| 2 | 0.22 | 0.53 | 0.49 | 44.17 |
| 4 | 0.16 | 0.42 | 0.37 | 44.04 |
| 8 | 0.09 | 0.24 | 0.18 | 47.41 |
| 15 | 0.07 | 0.14 | 0.10 | 65.68 |
| 20 | 0.05 | 0.10 | 0.07 | 82.36 |

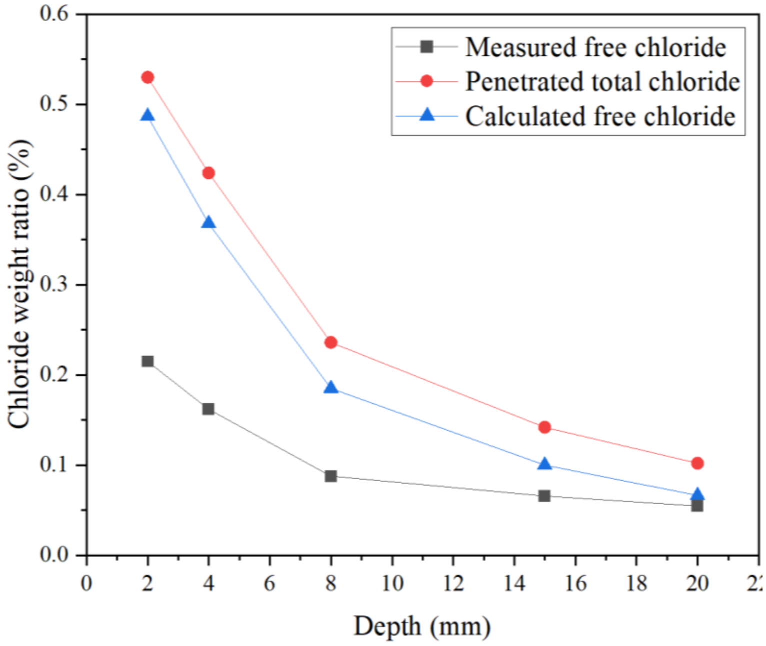


Figure 5-25 Monitoring results of the specimens with water/cement ratios: 0.3

Table 5-3 Monitoring results of the specimens with water/cement ratios: 0.4

| Depth(mm) | $C_m$(%) | $C_p$(%) | $C_f$(%) | Accuracy $C_m/C_f$ (%) |
|---|---|---|---|---|
| 2 | 0.24 | 0.54 | 0.50 | 48.62 |
| 4 | 0.21 | 0.45 | 0.40 | 52.23 |
| 8 | 0.09 | 0.24 | 0.19 | 48.34 |
| 15 | 0.06 | 0.13 | 0.09 | 72.57 |
| 20 | 0.06 | 0.11 | 0.07 | 82.39 |

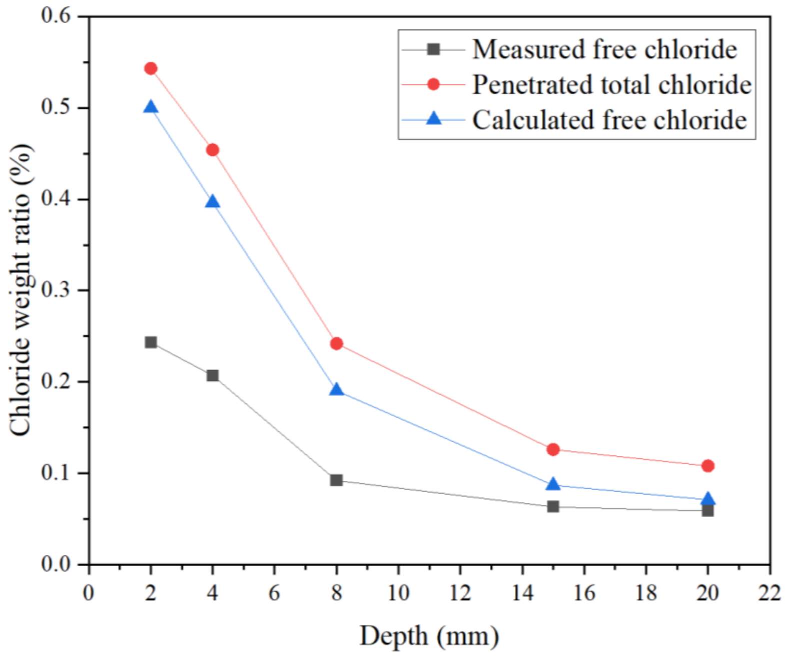


Figure 5-26 Monitoring results of the specimens with water/cement ratios: 0.4

Table 5-4 Monitoring results of the specimens with water/cement ratios: 0.5

| Depth(mm) | $C_m$(%) | $C_p$(%) | $C_f$(%) | Accuracy $C_m/C_f$ (%) |
|---|---|---|---|---|
| 2 | 0.23 | 0.57 | 0.52 | 44.40 |
| 4 | 0.20 | 0.49 | 0.43 | 45.78 |
| 8 | 0.11 | 0.26 | 0.20 | 51.30 |
| 15 | 0.08 | 0.14 | 0.10 | 79.70 |
| 20 | 0.06 | 0.11 | 0.07 | 85.77 |

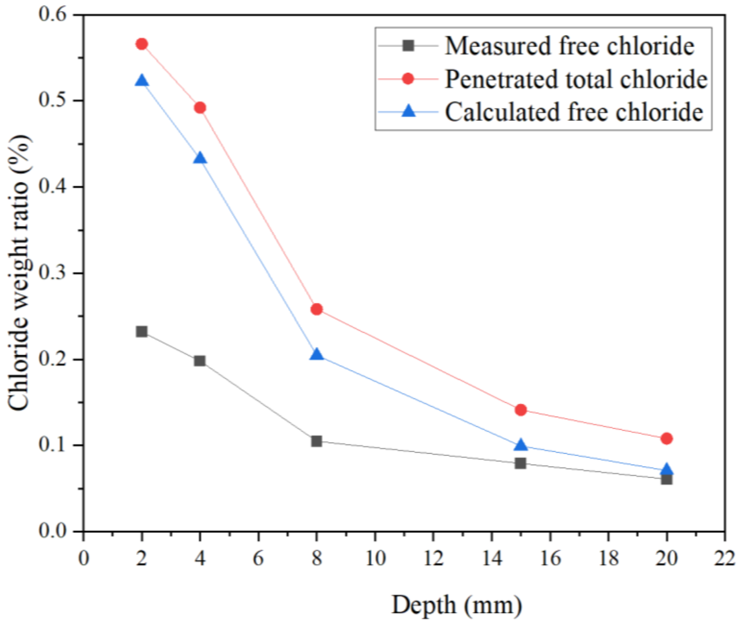


Figure 5-27 Monitoring results of the specimens with water/cement ratios: 0.5

### 5.3.5 Response of the fluorescence-based sensor for monitoring chloride in high humidity chamber

Figure 5-28 shows the response of the fluorescence-based sensor for monitoring chloride in high humidity chamber. The relative humidity inside the chamber was set at 40% during the first 9 months. From the results, we can find that the fluorescence intensity of the sensor initially increased by 5% during the first 3 months of observation and then decreased back to the initial fluorescence intensity after 9 months.

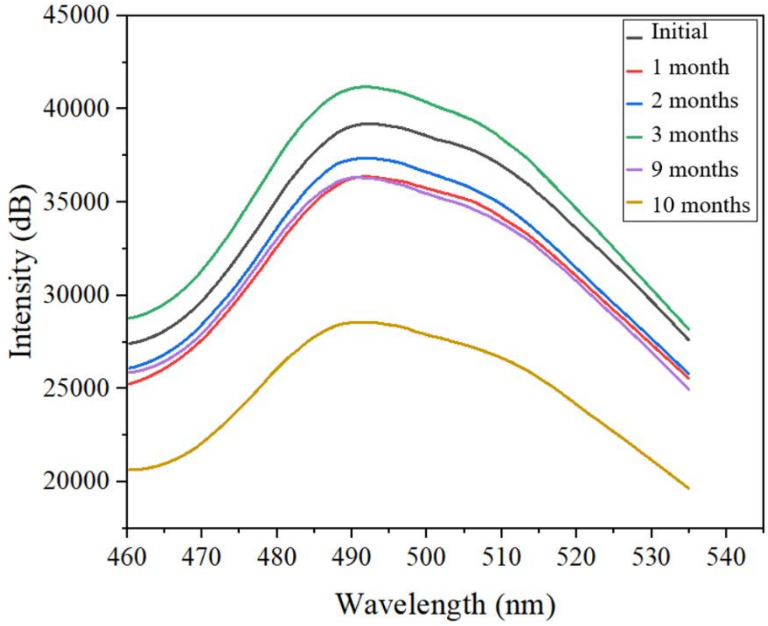


Figure 5-28 Results of sensor durability in accelerating chamber

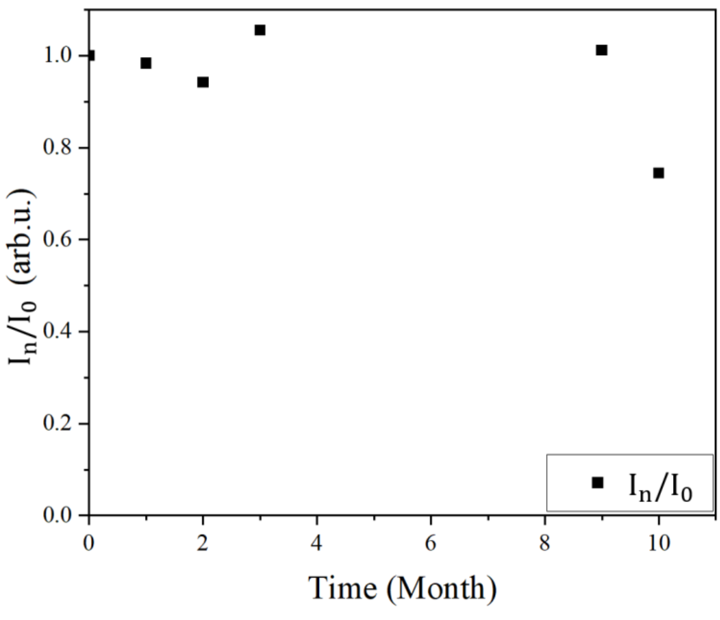


Figure 5-29 Intensity changes during the tests in high humidity chamber

The relative humidity inside the chamber was set at 100% after 9 months. From the results we can find that the fluorescence intensity of the sensor after 10 months decreases by 25% compared to the fluorescence intensity measured after 9 months (see

Figure 5-29). From the results, after a one-month high humidity accelerated experiment, a 25% decrease in the fluorescent intensity of the sensor was observed, which may be due to the continued high humidity causing part of the fluorescent substance in the sensor to dissolve. In addition, degradation was observed on the surface of the armored optical fiber cable (see Figure 5-30). Although the signal from the sensor can be transmitted by the armored optical fiber cable normally, it shows that in field applications, the armored optical fiber cable needs to be better protected to avoid possible excessive degradation.

(a) (b)

Figure 5-30 (a) Armored optical fiber cable photographed before the accelerated experiment (b) Armored optical fiber cable photographed after the accelerated experiment

## 5.4 Conclusions

In this chapter, a novel embeddable fluorescence-based sensor for monitoring chloride inside the concrete was developed, employing quinine sulphate as the fluorescent sensing element, in the previous research, which was rarely applied to monitor chemical parameters inside the concrete. Besides, a utilized sol-gel technology to embed quinine sulphate effectively within a solid matrix which ensure the quinine sulphate to be stably fixed on the glass pieces and maintain stable contact with the environment. Meanwhile, the sensor probes were developed using 3D printing which enables personalized customization and rapid production. These innovative efforts make the fluorescence-based sensors to monitor chloride inside concrete possible.

The response of the sensor was systematically evaluated through a series of experiments, including concrete simulation solutions, ionic interference tests, and natural chloride penetration studies. These experiments investigate the sensor's response and its potential for integration into monitoring chemical parameters inside the concrete.

The fluorescence intensity of quinine sulphate proportionally correlates with the concentration of free chloride ions and the relationship is in accordance with the Stern-Volmer law. This relationship is crucial for sensor calibration. The experimental results demonstrate that the sensitivity of the investigated fluorescence-based chloride sensors achieved 80%.

The sensor exhibited remarkable stability across the pH range (8.6-12.6) characteristic of concrete environments, underscoring its robustness under alkaline conditions. Furthermore, it displayed high selectivity for chloride ions, with minimal interference from competing anions (e.g., sulphate, nitrate, carbonate), a prerequisite for reliable operation in the chemically complex matrix of concrete.

Besides, the fluorescence-based sensor works well under normal temperature and normal relative humidity after being embedded inside the beam for 10 months. But the fluorescence intensity dropped by 25% after one-month accelerating test in the environmental chamber. In addition, degradation was observed on the surface of the armored optical fiber cable, this shows that, to use the fiber optic fluorescence-based sensor on site, the armored optical fiber cable needs to be better protected to avoid possible excessive degradation.

Collectively, these findings validate the fiber optic fluorescence-based sensor as a promising tool for real-time chloride monitoring in concrete structures. Its combination of pH resilience and ionic selectivity positions it as a viable candidate for long-term structural health monitoring, particularly in marine environments where chloride ingress poses significant durability risks.

# CHAPTER 6. DEVELOPMENT OF AN EMBEDDABLE FLUORESCENCE-BASED SENSING SYSTEM FOR MONITORING CHLORIDE AND SULPHATE INSIDE CONCRETE AND FIELD VALIDATION

## 6.1 Introduction

The durability of concrete structure is very important to the service life of infrastructure, and sulphate ion is one of the most critical factors affecting the durability of concrete structures which might cause softening and decay of the concrete matrix or expansive cracking, and other disruption associated with the formation of ettringite, and other reaction products (Hewlett and Lea 1998). Exposure to external sulphate-rich environments adversely impacts the structural performance of concrete, diminishing its long-term safety. Consequently, monitoring sulphate ion concentrations within concrete structures is essential to ensure both safety and durability.

Current non-destructive testing (NDT) methods for sulphate ion detection, such as magic angle spinning nuclear magnetic resonance spectroscopy (Peyvandi et al. 2015) and embedded piezoelectric transducers (Zou et al. 2019), face limitations in field applicability and cost-effectiveness (Liu et al. 2022). These challenges highlight the need for alternative sensing technologies. Fiber optic sensing systems gain more interest as alternative sensing technology, due to their capability to operate in risky environment, greater sensitivity, approaches for combining sensing and immunity to electromagnetic interferences.

In this chapter, an embeddable fluorescence-based sensor for monitoring sulphate inside the concrete is investigated. Then introduces an embeddable fluorescence-based sensing system for monitoring chloride and sulphate inside the concrete. The performance of fluorescence-based sensors for monitoring chloride and sulphate was studied with experiment in laboratory. Besides, a test was conducted to validate the fluorescence-based sensing system in the field.

## 6.2 Experimental Design

### 6.2.1 Development of an embeddable fluorescence-based sensor for monitoring sulphate inside concrete

*6.2.1.1 Selection of sulphate-sensitive fluorescent material*

Fluorescence-based sensors enable direct measurement of environmental chemical parameters by detecting changes in fluorescence intensity corresponding to analyte concentrations. In this chapter, a sulphate-sensitive fluorescent material was synthesized.

Morin (3,5,7,2′,4′-pentahydroxyflavone) is a well-known biologically active natural antioxidant existing widely in fruits, vegetables, and many herbs. Figure 6-1 shows the structure of morin, and it has two aromatic rings (A and B) linked by an oxygen- containing heterocycle (C). Due to suitable arrangement of the hydroxyl groups in the molecule, morin easily forms complexes by chelating metal ions (Panhwar et al. 2010). For this reason, morin is widely used as an effective reagent for extraction and spectrophotometric determination of some metal ions. (Pęgier et al. 2021).

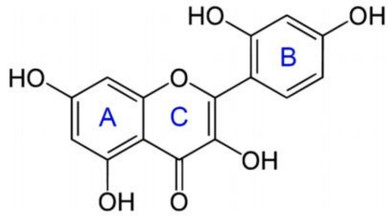


Figure 6-1 Molecular structure of morin (Pęgier et al. 2021)

According to Li (Li et al. 1990), scandium ions formats complexes with morin. After the formation, the lowest singlet excited state of organic ligand. Morin will change from n, $\pi_1^*$ to π, $\pi_1^*$ through intersystem crossing. The molecular structure will change from non-rigid to rigid, which makes the organic ligand of morin change from no fluorescence or weak fluorescence to strong fluorescence. The ionic interactions between sulphate anions and $Sc^{3+}$ demonstrate superior bond strength compared to the coordination interactions in $Sc^{3+}$-morin complexes. This competitive binding enables sulphate ions to displace morin ligands from the coordination sphere, inducing structural disintegration of the luminescent complex. The resultant disruption of the fluorophore's electronic configuration manifests as measurable fluorescence attenuation (HE 2020). Thus, the scandium-morin fluorescent complex is selected as the sensing element used in fluorescence-based sulphate sensor.

*6.2.1.2 Optimization of scandium-morin concentration ratio*

FS5 Spectrofluorometer from Edinburgh Instruments (see Figure 6-2) is applied to study the influence from the concentration ratio of scandium solution and morin solution. The FS5 Spectrofluorometer can gain optimal excitation and emission wavelengths. Excitation-emission map of scandium-morin fluorescent complex shows that the mixture of scandium ion solution and morin solution has strong fluorescence (see Figure 6-3). The optimal excitation wavelength is 449 nm, and the optimal emission wavelength is 510 nm.

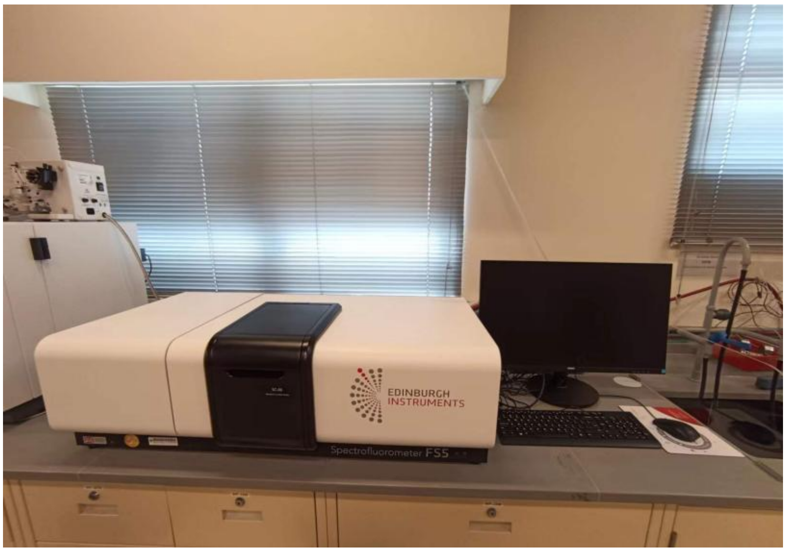


Figure 6-2 FS5 Spectrofluorometer from Edinburgh Instruments

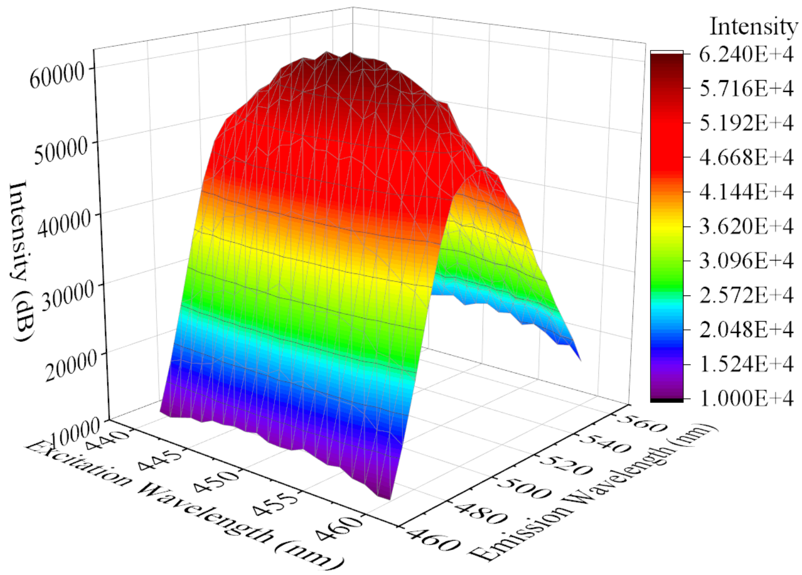


Figure 6-3 Excitation-emission map of scandium-morin fluorescent complex

Then six samples with different concentration ratio of scandium and morin (Table 6-1) were tested to find the influence of concentration ratio of scandium and morin to the intensity of the emitted light. The scandium solution was 0.0139 mol/L and the morin solution was 0.0033 mol/L. Samples were put inside the quartz tube in the FS5 Spectrofluorometer. Then FS5 Spectrofluorometer was used to take excitation-emission maps of 6 samples with different concentration ratio.

Table 6-1 Six samples prepared for scandium/morin ratio optimization

| Sample number | 1 | 2 | 3 | 4 | 5 | 6 |
|---|---|---|---|---|---|---|
| Water/μL | 1372 | 1343 | 1282 | 1099 | 733 | 366 |
| Scandium solution/μL | 92 | 122 | 183 | 366 | 733 | 1099 |
| Morin solution/μL | 2040 | 2040 | 2040 | 2040 | 2040 | 2040 |
| Sc: Morin molar ratio | 1:4 | 1:3 | 1:2 | 1:1 | 2:1 | 3:1 |

*6.2.1.3 Preparation of scandium-morin fluorescent complex*

The setups of the preparation of scandium-morin fluorescent complex were as follows:

Stage 1: Scandium Precursor Synthesis. Scandium oxide (0.0959 g) and hydrochloric acid (50mL, 3 mol/L) were stirred in a 200 mL beaker with a thermostatic magnetic stirrer at 60℃ for 24 hours (see Figure 6-4). The cooled solution was transferred to a standard volumetric flask and adjusted to a final volume of 100 mL with deionized water.

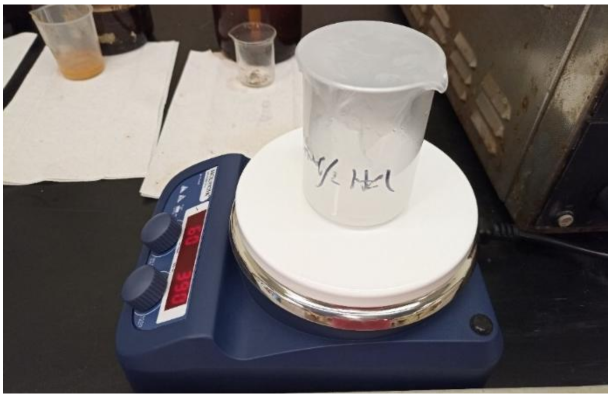

Figure 6-4 Preparation of scandium solution

Stage 2: Morin Fluorophore Preparation. An ethanolic morin stock solution (1 mg/mL) was prepared by dissolving 0.1 g of morin hydrate in 100 mL of anhydrous ethanol under ambient conditions, followed by vortex mixing until complete dissolution.

Stage 3: Sc-Morin Coordination Complex Assembly. The fluorescent Sc-morin adduct was synthesized through a controlled stoichiometric combination of the scandium precursor and morin solutions (see Figure 6-5). This hybridization process leverages $Sc^{3+}$'s affinity for morin's hydroxyl and carbonyl groups, forming a photoactive complex via metal-ligand coordination.

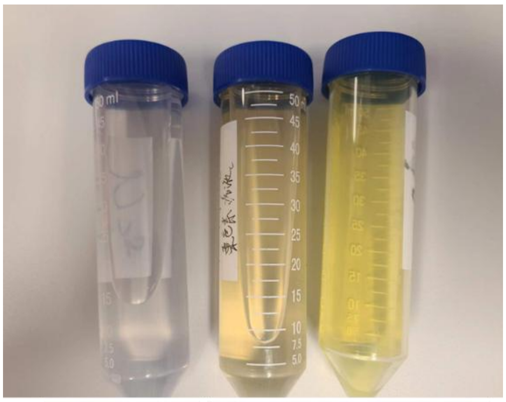

(a) (b) (c)

Figure 6-5 (a) Scandium solution, (b) Morin solution. (c) Scandium-morin fluorescent complex

*6.2.1.4 Preparation of sulphate-sensitive film*

For fixation of fluorescent material in the sensor probe, after preparation of scandium-morin fluorescent complex, sulphate sensing film was fabricated with the following steps:

Stage 1: Polymer Matrix Formulation. A cellulose acetate (0.54 g) base was homogenized with acetone (30 mL) in a sealed glass vial under continuous agitation until complete dissolution.

Stage 2: Fluorophore Integration. The polymeric solution was doped with 6.2 mL of $Sc^{3+}$-morin complex suspension, creating a photosensitive composite matrix through controlled miscibility.

Stage 3: Substrate Preparation. Glass piece substrates underwent sequential ultrasonic cleaning in acetone baths (3 cycles, 10 min each) to remove particulate contaminants, followed by nitrogen stream drying.

Stage 4: Film Deposition. Cleaned substrates received 80 μL aliquots of the Sc-morin polymer composite with pipette.

Stage 5: Curing. Solvent evaporation was accelerated under ventilated conditions (fume hood, 25°C). Four iterative deposition-curing cycles were executed to achieve optimal film thickness and fluorophore density (see Figure 6-6).


(a)

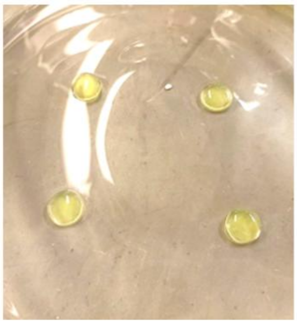
(b)


(c)

Figure 6-6 (a) Mixture of scandium-morin fluorescent complex solution and cellulose acetate solution, (b) Glass pieces substrate with solution on the surface (c) Glass pieces substrate with sensing film

*6.2.1.5 Fabrication of sensor housing with 3D printing*

Figure 6-7 shows sensor housing, and it was fabricated with 3D printing technology. It can connect to one end of the Y-type coupler fiber directly.

Figure 6-7 3D printed sensor housing

*6.2.1.6 Schematic of the fluorescence-based sensor for monitoring sulphate inside concrete*

Figure 6-8 shows the schematic of the fluorescence-based sensor for monitoring sulphate inside concrete. The laser from a 10.08 mW LED will emit laser at a center wavelength of 375 nm. Then the laser is coupled through a Y- type multimode VIS/NIR fiber with BX Jacket (Ocean Insight). The other end of the fiber coupler is connected to the sensor probe with a SMA connector. With the change of sulphate concentration, light emitted from the sensing element changes at the same time and the emitted light will be guided through the other branch of the fiber coupler to a spectrometer. The output of the spectrometer will be displayed on a computer screen.

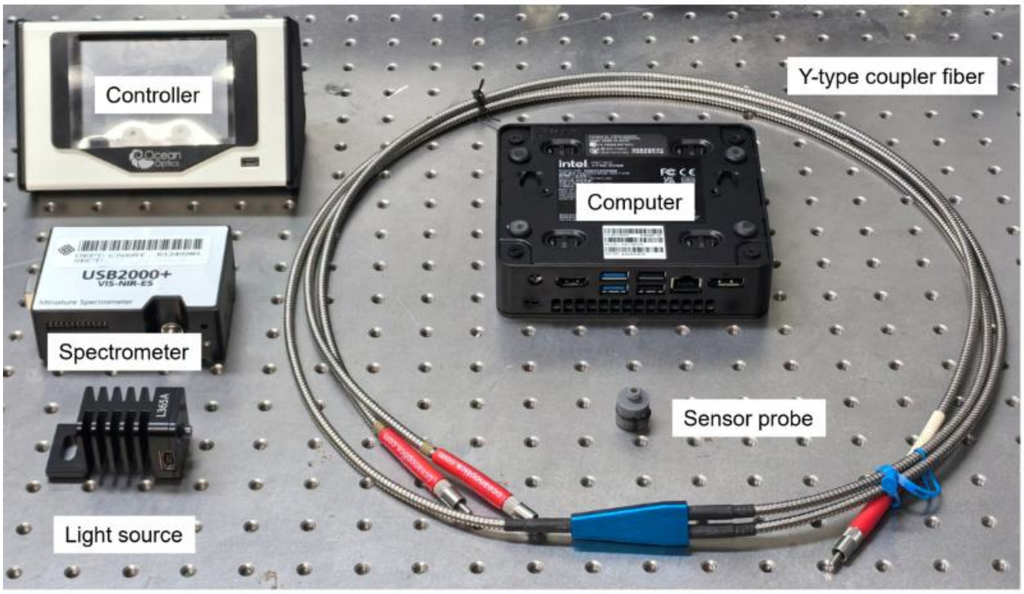


Figure 6-8 Schematic of the fluorescence-based sensor for monitoring sulphate inside concrete

## 6.2.2 Tests in sulphate solutions

After the preparation of scandium-morin fluorescent complex, its response in sulphate solution was tested. The schematic of the tests in sulphate solutions was the same as Chapter. 6.2.1.6. The sensing probe was changed to an empty probe with glass piece at the bottom. This probe was used to protect the fiber cable. The response tests were carried out as follows: (1) Put the empty probe inside 2 mL of prepared scandium-morin fluorescent complex. (2) Record the result from the spectrometer as fluorescence intensity 0 ($I_0$). (3) Add 100 μL 0.05mol/L sulphate solution with pipette. (4) Record the result from the spectrometer as fluorescence intensity n ($I_n$). (5) Repeat Step (3) and Step (4) 10 times. (6) Analyze the data with a computer.

After investigating the response of the scandium-morin fluorescent complex to sulphate and the preparation of the sulphate sensing film, the response of the fluorescence-based sensor for monitoring sulphate in the sulphate solutions was tested. The response tests were carried out as follows: (1) Put the sensor probe with sulphate sensing film inside 2 mL of deionized water. (2) Record the result from the spectrometer as fluorescence $\mathrm{I_0}$. (3) Add 100 μL 0.05mol/L sulphate solution with pipette. (4) Record the result from the spectrometer as fluorescence $\mathrm{I_n}$. (5) Repeat Step (3) and Step (4) 10 times. (6) Analyze the data with a computer.

### 6.2.3 Development of an embeddable fluorescence-based sensor for monitoring chloride and sulphate inside concrete

Built upon the developed fluorescence-based sensor for monitoring chloride and fluorescence-based sensor for monitoring sulphate, a fluorescence-based sensor for monitoring chloride and sulphate was developed.

The design of the fluorescence-based sensor for monitoring chloride and sulphate is the same with the design of fluorescence-based sensor introduced in previous chapter.

To monitor sulphate and chloride simultaneously, a new sensing element preparation process is applied. After cleaning quartz pieces with acetone and dry the pieces using compressed air. An isolation layer is added on the surface of the cleaned quartz pieces to prevent chloride sensitive complex and sulphate sensitive complex from contacting. Figure 6-9 shows the sensing element for monitoring chloride and sulphate.

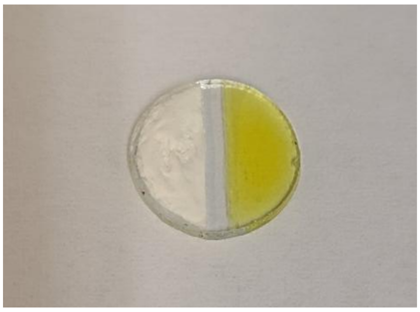

Figure 6-9 Sensing element for chloride and sulphate monitoring on quartz pieces

This design can reduce the package size and number of armored fiber cables in the on-site monitoring of chemical parameters. Furthermore, this design can improve accuracy through intercalibration from two different sensing elements.

### 6.2.4 Tests in chloride and sulphate solutions

The fluorescence-based sensor for monitoring chloride and sulphate was tested in chloride and sulphate solutions with different concentrations. The chloride and sulphate concentrations were shown in Table 6-2. The response tests were carried out as follows: (1) Put the sensor probe inside 2 mL of deionized water. (2) Record the result from the spectrometer as fluorescence $I_0$. (3) Put the sensor probe to 2 mL of specimen number 1. (4) Record the result from the spectrometer as fluorescence $I_1$. (5) Repeat Step (1) to Step (4) in different specimens. (6) Analyze the data with a computer.

Table 6-2 Sulphate and chloride concentrations

| Specimen number | Chloride concentration(mol/L) | Sulphate concentration(mol/L) |
|---|---|---|
| 1 | 0.214 | 0.025 |
| 2 | 0.128 | 0.075 |
| 3 | 0.043 | 0.125 |

### 6.2.5 Commission of field tests to validate the embeddable fluorescence-based sensing system for monitoring chloride and sulphate inside concrete

In previous research, it is rare to apply the fluorescence-based sensing system for monitoring chemical parameters inside concrete. Most fluorescence-based sensors are used as biosensors, for example, Cai (Cai et al. 2015) developed a rapid fluorescence sensor to detect Glutathione based on carbon dots-$MnO_2$ nanocomposites, Liu (Liu et al. 2018) uses bovine serum albumin functionalized as fluorescence material to detect Glutathione, and Xiao (Xiao et al. 2020) introduced a fluorescence probe based on carbon dots and $YVO_4: Dy^{3+}$ to detect alkaline phosphatase.

In Chapter.5, the fluorescence-based sensor for monitoring chloride was tested in cement mortar specimens and the results showed that the fluorescence-based sensor can monitor the changes of chemical parameters. To further study the possibility of field application of fluorescence-based sensing system for monitoring chloride and sulphate, a commission of the sensing system was carried out in a wave wall project.

#### *6.2.5.1 Development of a fluorescence-based sensing system for monitoring chloride and sulphate inside concrete*

The fluorescence-based sensing system for monitoring chloride and sulphate inside concrete includes five parts, fluorescence-based sensor probe, a connect system, an automatic data collection system, an automatic transmission system and a support system.

Fluorescence-based sensor probe: The fluorescence-based sensor probe consists of 3D printed housing, a glass piece to protect the end of optical fiber cable, fluorescence material, and a nylon film to protect the fluorescence material.

Connect system: A multimode armored fiber optic cable with core diameter at 1500 μm and standard flange are used in this system to connect the sensor probe and one end of the Y-type coupler fiber in the automatic data collection system.

Automatic data collection system: The automatic data collection system includes laser source, laser controller, spectrometer, Y-type coupler fiber and a computer.

Automatic transmission system: The automatic transmission system includes a wireless adapter inside the computer and a 4G LTE Customer Premises Equipment (CPE) router.

Support system: The support system includes an outdoor waterproof metal box, a PSU and a solar panel.

These five systems can achieve four key functions include:

Data Processing: The spectrometer obtains fluorescence intensity from the fluorescence-based sensors. The software installed in the computer collects data from the spectrometer.

Cloud Connectivity: The computer can access the LTE network from the LTE CPE router and the software will upload the data to a cloud server. The cloud server can be accessed remotely with a website.

Power Management: UPS and the solar panel ensure continuous and stable power supply to the computer and laser source.

Environmental Protection: The outdoor waterproof metal box protects other equipment during field tests. Besides, installed CCTV can be accessed remotely via a website.

*6.2.5.2 Introduction of field test site*

The field test was carried out in Lei Yue Mun. It is a costal enhancement work, and it is a 60-meters wave wall built with FRP concrete. Figure 6-10 shows the proposed location of the wave wall. A typical section of the wave wall is close to an L shape (see Figure 6-11). The test site is adjacent to Victoria Harbor which provides a real-world marine environment like salinity. Besides, this site is in the suburbs, and it poses challenges for power supply, equipment protection, and stable network access, allowing the experiment conducted here to accumulate experience for future industrial applications.

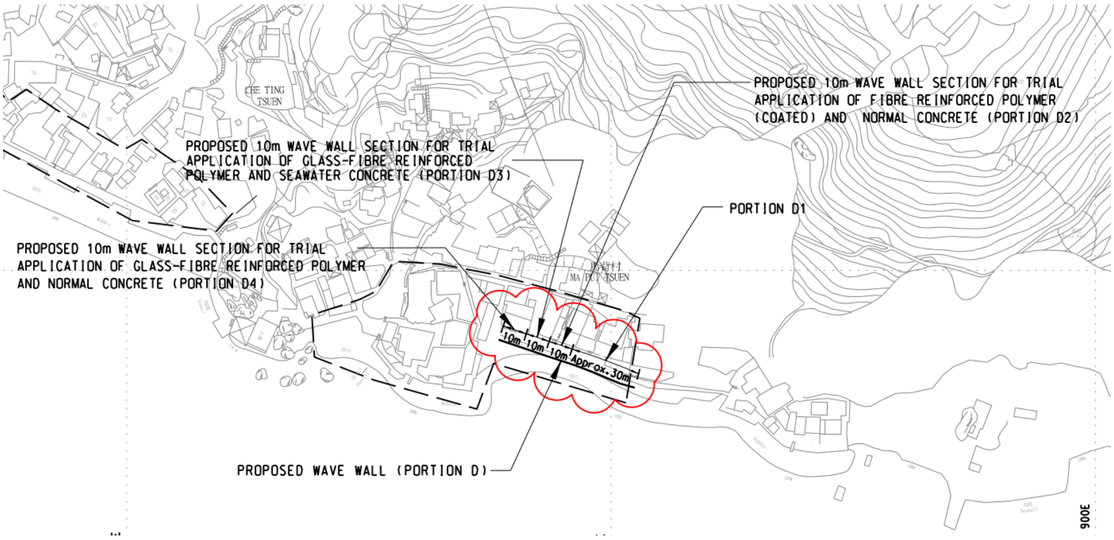


Figure 6-10 Proposed wave wall in Lei Yue Mun

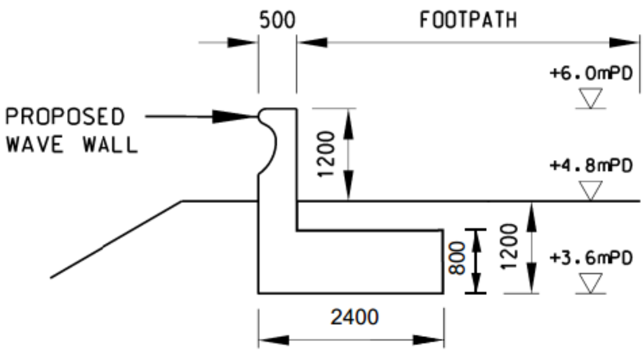


Figure 6-11 Typical section of wave wall

*6.2.5.3 Commission of field test of the fluorescence-based sensing system for monitoring chloride and sulphate in concrete*

The fluorescence-based sensing system for monitoring chloride and sulphate inside concrete was installed in the wave wall. The steps of the installation of the fluorescence-based sensor were as follows: (1) Drilling: Precise holes were drilled into the beam to accommodate the sensor (see Figure 6-12). (2) Sensor Placement: The debris was cleaned out in the hole. Then fluorescence-based sensor was inserted into cavities carefully. (3) Protection Measures: Quick hardening cement was packed into the gap between the sensor probe and the hole wall to fix the sensor probe and isolate the internal environment of the hole (see Figure 6-13).

Figure 6-12 Hole drilling in the wave wall

Figure 6-13 Sensor probe fixed with quick hardening cement

Then the connect system, the automatic data collection system, the automatic transmission system, and UPS were placed in the outdoor waterproof metal box (see Figure 6-14). The solar panel was connected to the UPS for continuous power supply.

Figure 6-14 The fluorescence-based sensing system for monitoring chloride and sulphate in the outdoor waterproof metal box and solar panel

Then, outdoor waterproof metal box was installed with expansion screw (see Figure 6-15).

(a) (b)

Figure 6-15 (a) Back of outdoor waterproof metal box (b) Installed outdoor waterproof metal box

## 6.3 Results and Discussion

### 6.3.1 Results of optimization of scandium-morin concentration ratio

From Figure 6-16 to Figure 6-21 shows the results. From the results, we can find that the peak value of the intensity increased when the molar ratio increased from 1:4 to 2:1 and the peak value of the intensity in the excitation-emission maps dropped when the molar ratio increased from 2:1 to 3:1. Thus molar ratio of 2:1 was chosen in the following tests due to the highest peak intensity in the excitation-emission maps.

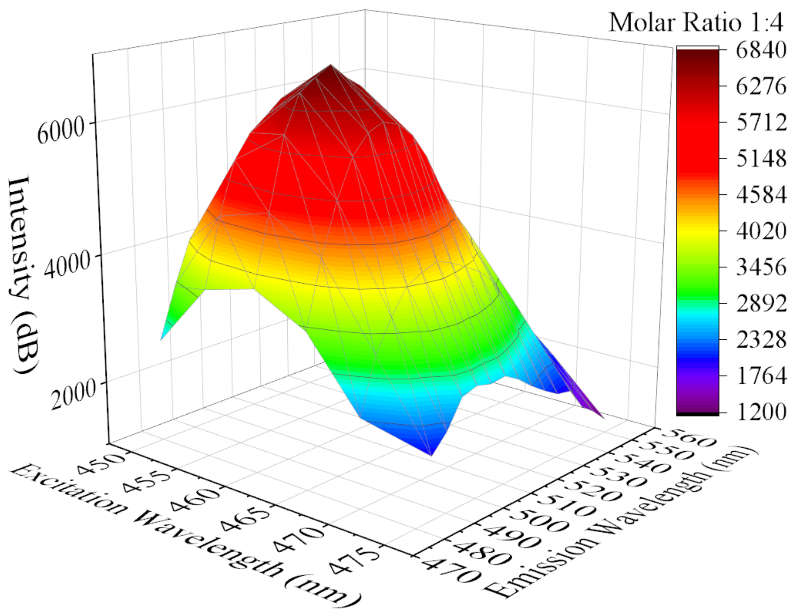


Figure 6-16 Excitation-emission map (molar ratio 1:4)

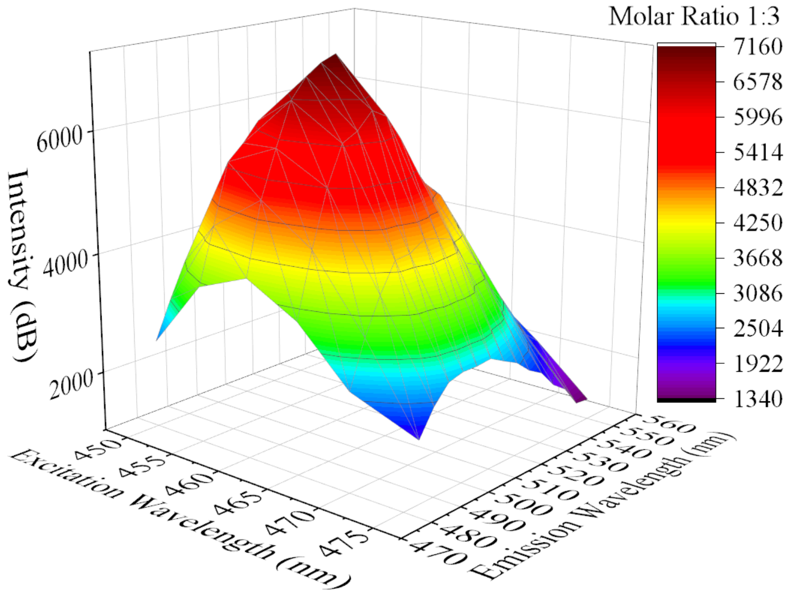


Figure 6-17 Excitation-emission map (molar ratio 1:3)

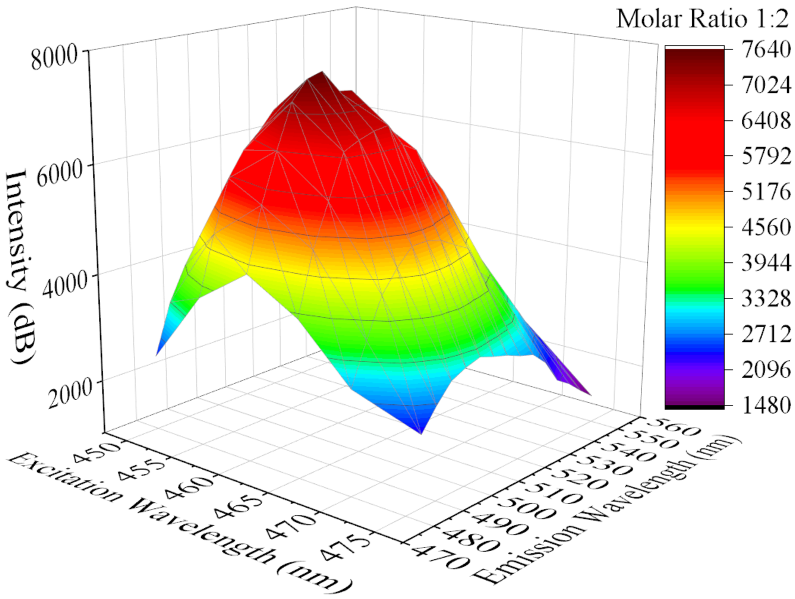


Figure 6-18 Excitation-emission map (molar ratio 1:2)

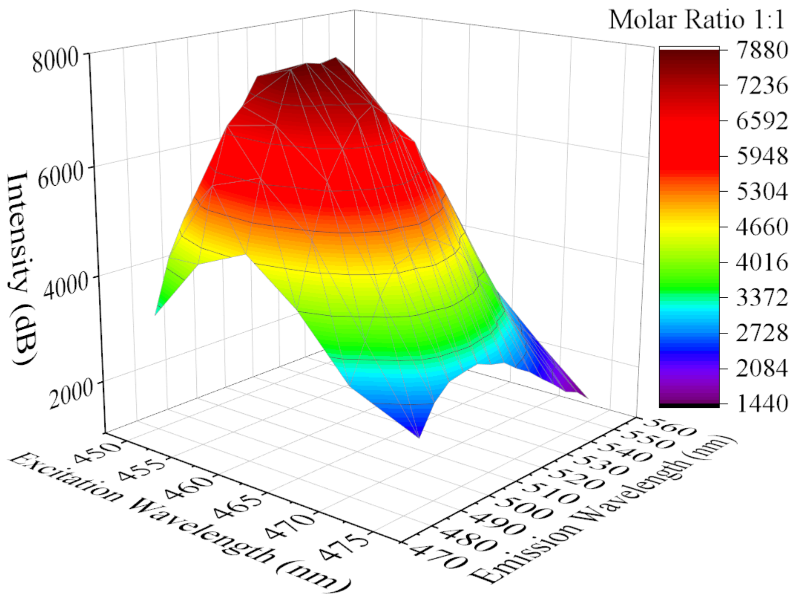


Figure 6-19 Excitation-emission map (molar ratio 1:1)

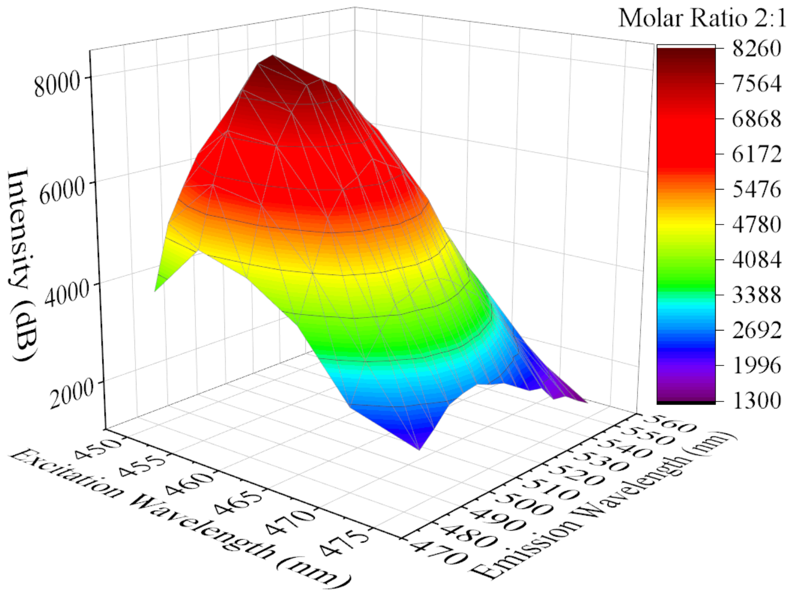


Figure 6-20 Excitation-emission map (molar ratio 2:1)

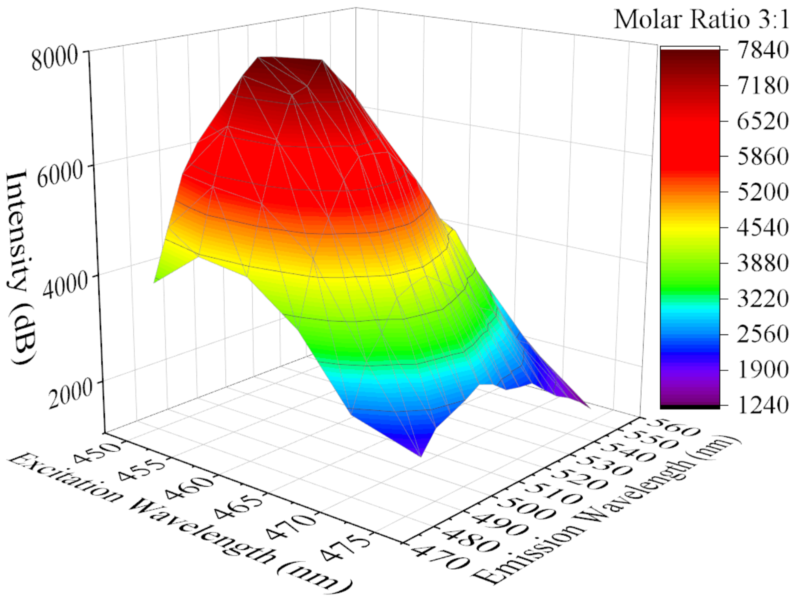


Figure 6-21 Excitation-emission map (molar ratio 3:1)

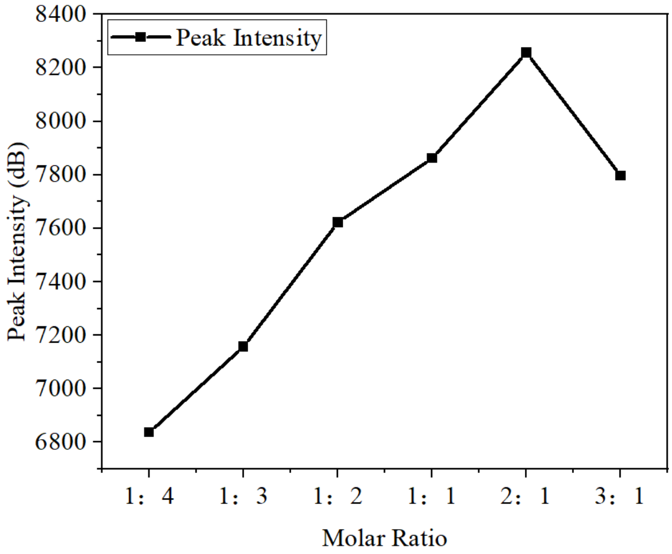


Figure 6-22 Peak value of the intensity in excitation-emission maps

### 6.3.2 Response of the scandium-morin complex in sulphate solutions

Figure 6-23 and Figure 6-24 shows the response of scandium-morin complex in sulphate solutions. The sulphate sensing complex was sensitive to sulphate ion and the fluorescent intensity of the sulphate sensing complex dropped down with the increase of sulphate concentration. The fluorescence intensity of the developed fluorescence-based sulphate sensor proportionally correlated with the sulphate ion concentration in different sulphate ion solutions in accordance with the Stern-Volmer law. The relationship between $I_0/I_n$ and sulphate concentration was shown below:

$$\frac{I_0}{I_n} = 0.69698 + 167.22[SO_4{}^{2-}] \tag{6-1}$$

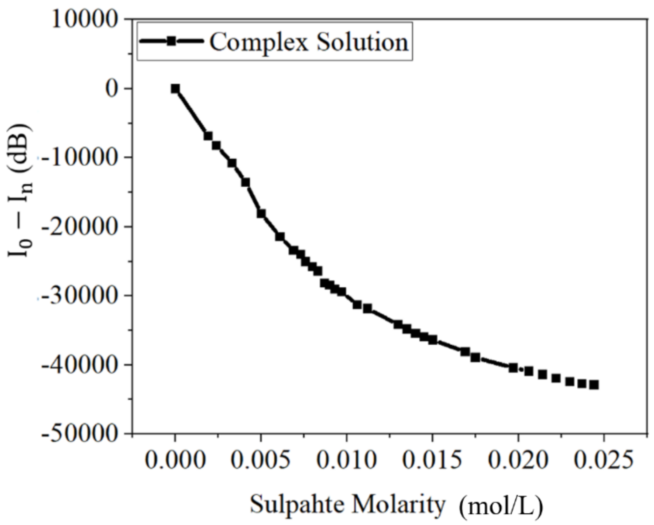


Figure 6-23 Results of the scandium-morin fluorescent complex to the sulphate

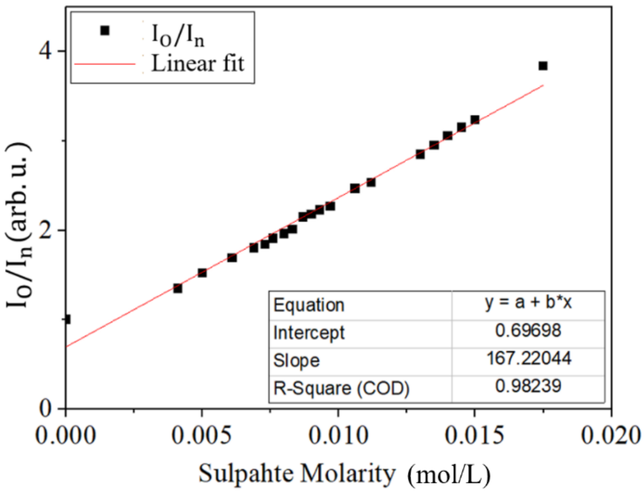


Figure 6-24 Linear fit of $I_0$/ $I_n$ to sulphate molarity (scandium-morin fluorescent complex)

### 6.3.3 Response of the fluorescence-based sensor for monitoring sulphate in sulphate solutions

Figure 6-25, Figure 6-26, and Figure 6-27 shows the response of the fluorescence-based sensor for monitoring sulphate in the sulphate solutions. The intensity of the sensor decreased with increasing sulphate molarity. The ratio of $I_0$ and $I_n$ had a linear relationship when the sulphate molarity was below 0.01 mol/L. The relationship between $I_0/I_n$ was shown below:

$$\frac{I_0}{I_n} = 0.99632 + 16.66927[SO_4{}^{2-}] \tag{6-2}$$

The sulphate concentration in sea water is around 0.03 mol/L. The peak intensity of the fluorescence-based sensor for monitoring sulphate will drop down significantly, if seawater erosion occurs within the marine concrete.

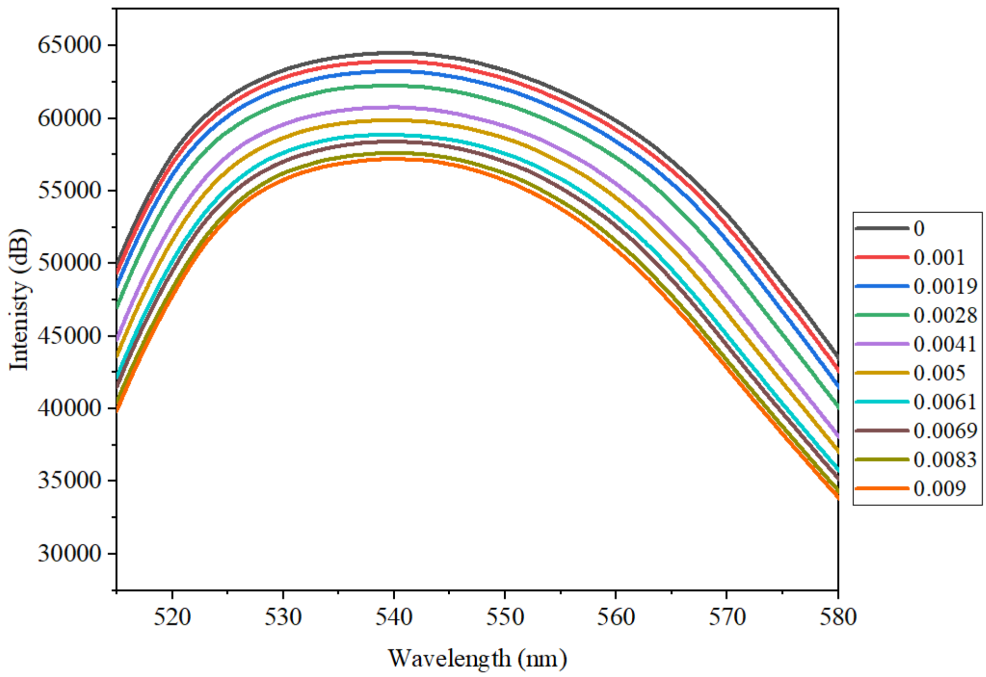


Figure 6-25 Response of the fluorescence-based sensor for monitoring sulphate in the sulphate solutions

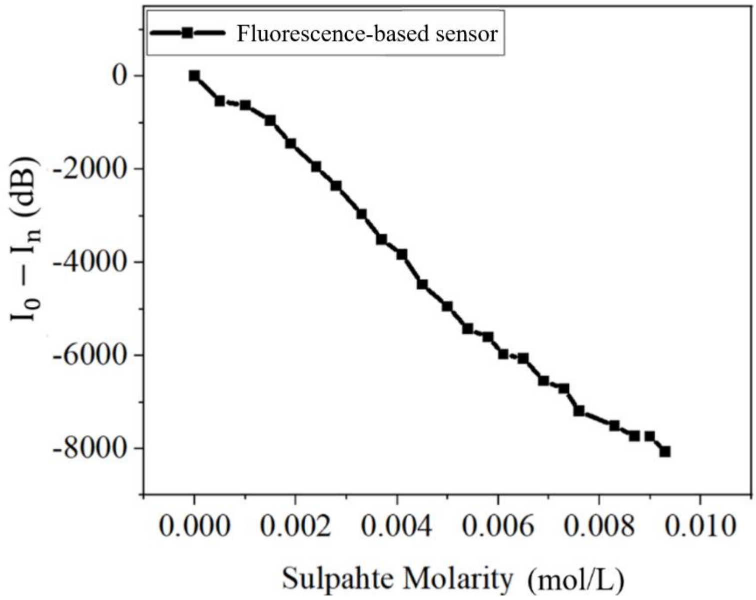


Figure 6-26 Results of the fluorescence-based sensor for monitoring sulphate in the sulphate solutions

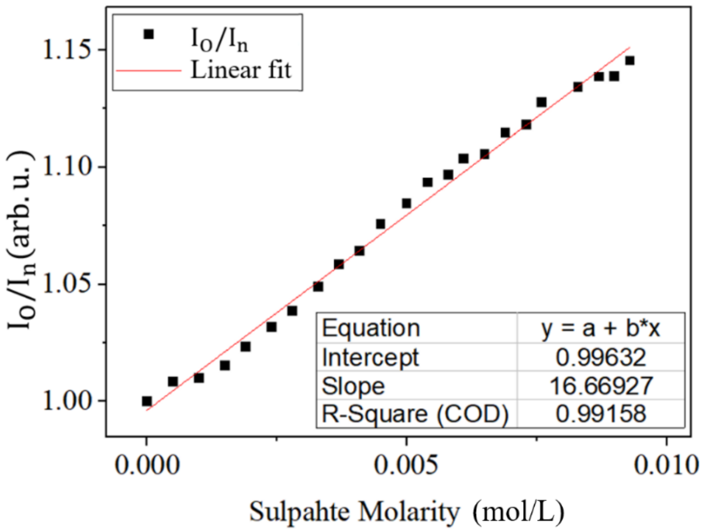


Figure 6-27 Linear fit of $I_0$ / $I_n$ to sulphate molarity (fluorescence-based sensor)

### 6.3.4 Response of the fluorescence-based sensor for monitoring chloride and sulphate in chloride and sulphate solutions

In Figure 6-28, Figure 6-29, and Figure 6-30, we can find that the fluorescence-based sensor for monitoring chloride and sulphate had two peaks. One peak was at

438.397 nm and the other was at 509.161 nm. Compared with the sensors developed in the previous chapter, the chloride sensitive peak and sulphate sensitive peak both had a left shift.

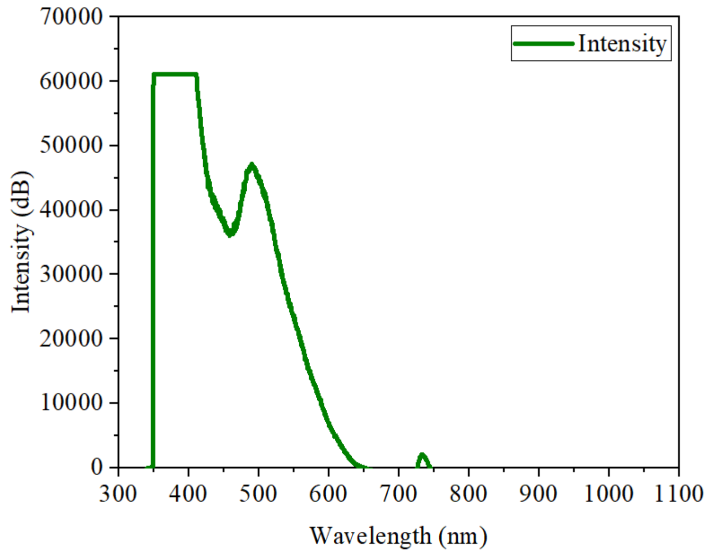


Figure 6-28 Fluorescence intensity of fluorescence-based sensor for monitoring chloride

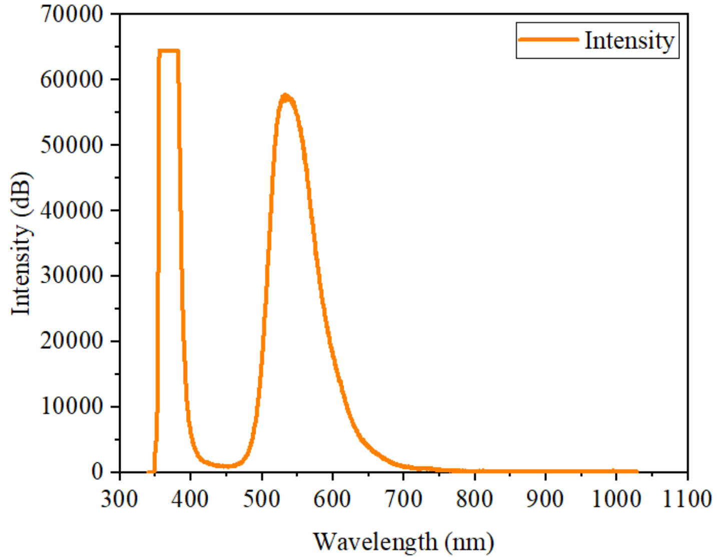


Figure 6-29 Fluorescence intensity of fluorescence-based sensor for monitoring sulphate

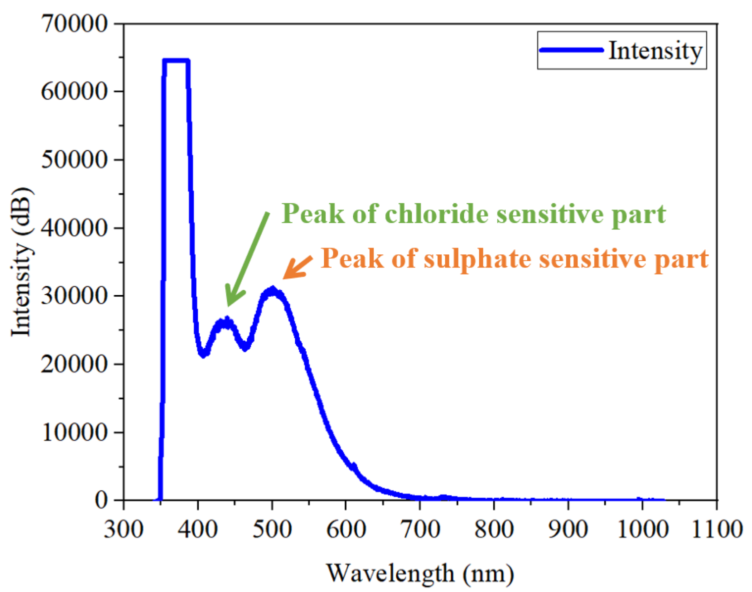


Figure 6-30 Fluorescence intensity of fluorescence-based sensor for monitoring chloride and sulphate

Figure 6-31 shows one result of the fluorescence-based sensor for monitoring chloride and sulphate in chloride and sulphate solution. $I_0$ is the initial fluorescence intensity and $I_1$ is the subsequent fluorescence intensity. We can find that two peaks of the fluorescence intensity both dropped down in the chloride and sulphate solution.

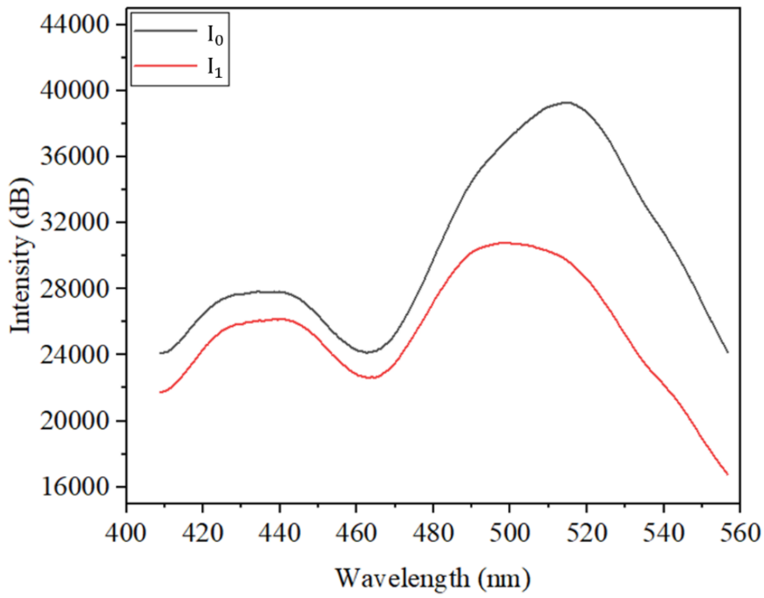


Figure 6-31 One result of the developed sensor in chloride and sulphate solution

In Figure 6-32, we can find that $I_0/I_1$ changed with different concentrations of chloride and sulphate. $I_0/I_1$ at 438.397 nm and at 509.161 nm changed with chloride concentration and sulphate concentration separately. The relationship of $I_0/I_1$ to chloride concentration and sulphate were shown below:

$$I_0/I_1 = 1.04556 + 0.46793[Cl^-]\ (438.397\ nm) \quad (6\text{-}3)$$

$$I_0/I_1 = 1.19659 + 0.64361\left[SO_4{}^{2-}\right]\ (509.161\ nm) \quad (6\text{-}4)$$

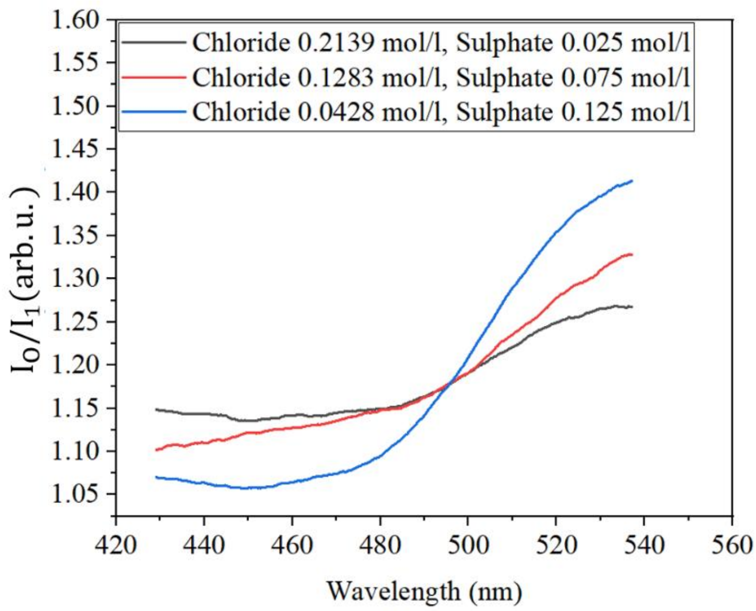


Figure 6-32 $I_0/I_1$ under different concentrations of chloride and sulphate

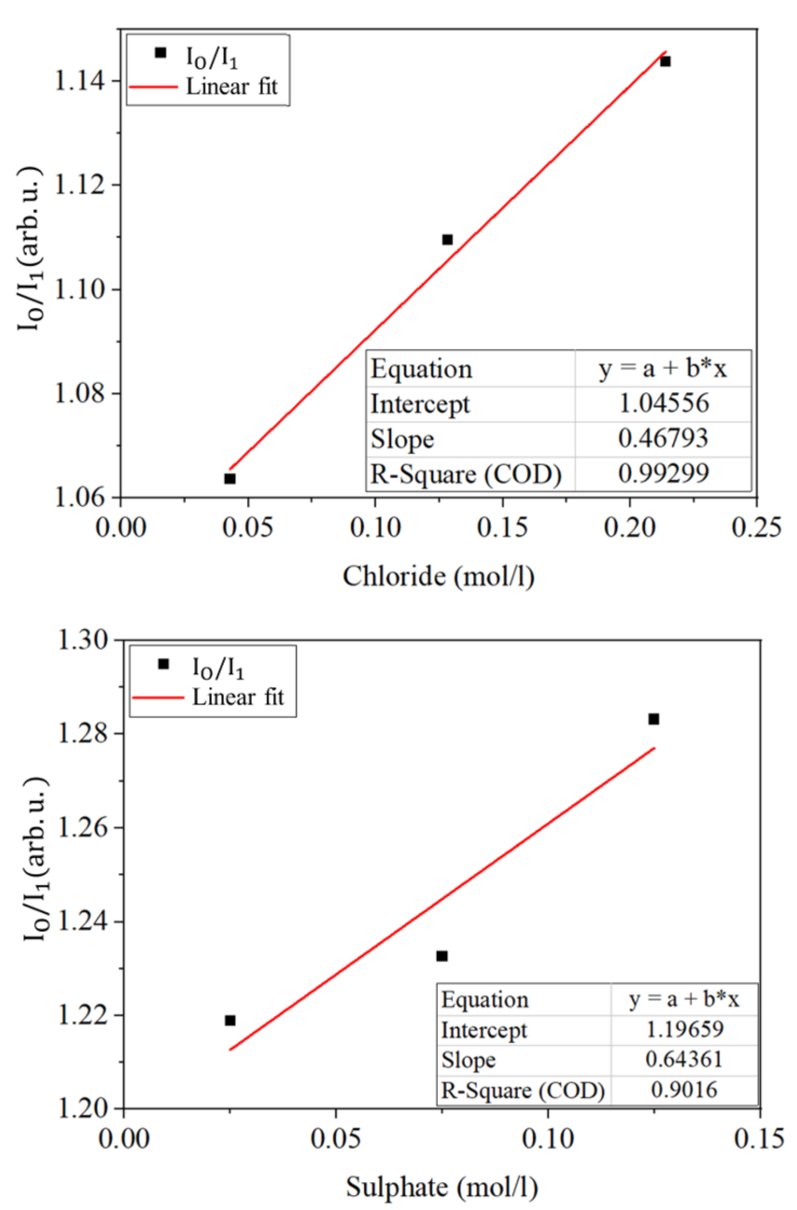


Figure 6-33 $I_0/I_1$ at 438.397 nm to chloride concentration and at 509.161 nm to sulphate concentration

### 6.3.5 Results of the commission of field tests of the embeddable fluorescence-based sensing system for monitoring chloride and sulphate

The commission of field tests last for one month. During the commission of the field test, the fluorescence-based sensing system for monitoring chloride and sulphate worked well and uploaded the data to the cloud server automatically at one hour interval. From the results we can find that the intensity of the fluorescence-based sensor for monitoring chloride and sulphate had two peaks, and both peaks had a slow downward trend during the commission (see Figure 6-34, Figure 6-35, and Figure 6-36). The intensity fluctuation of chloride sensitive peak was larger than that of sulphate sensitive peak. The results showed the developed fluorescence-based sensor worked properly after being embedded inside the concrete. The sensing system can collect and upload the data to cloud server automatically. The commission showed great possibility of applying fluorescence-based sensing system for monitoring chloride and sulphate in the field.

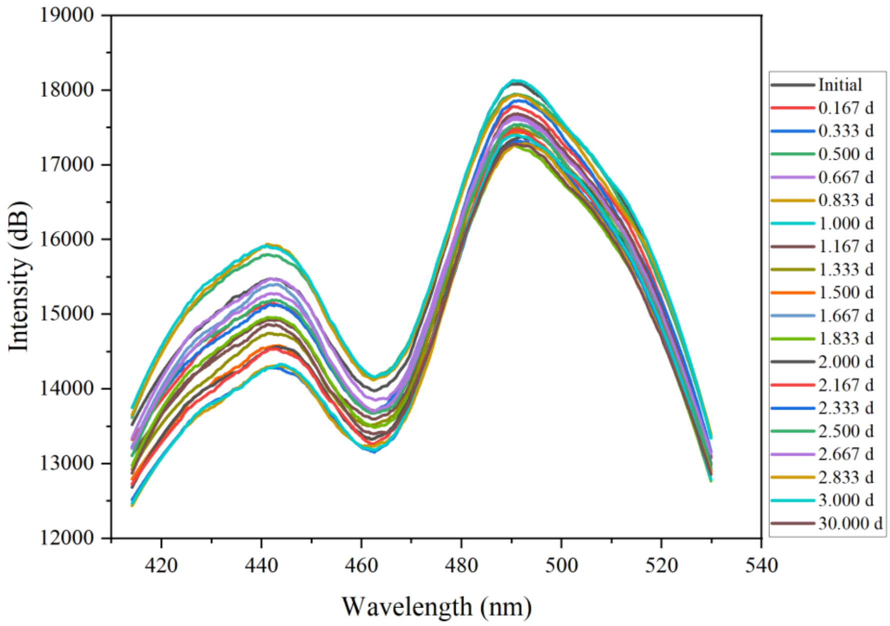


Figure 6-34 Results of the commission of field tests of the embeddable fluorescence-based sensing system for monitoring chloride and sulphate

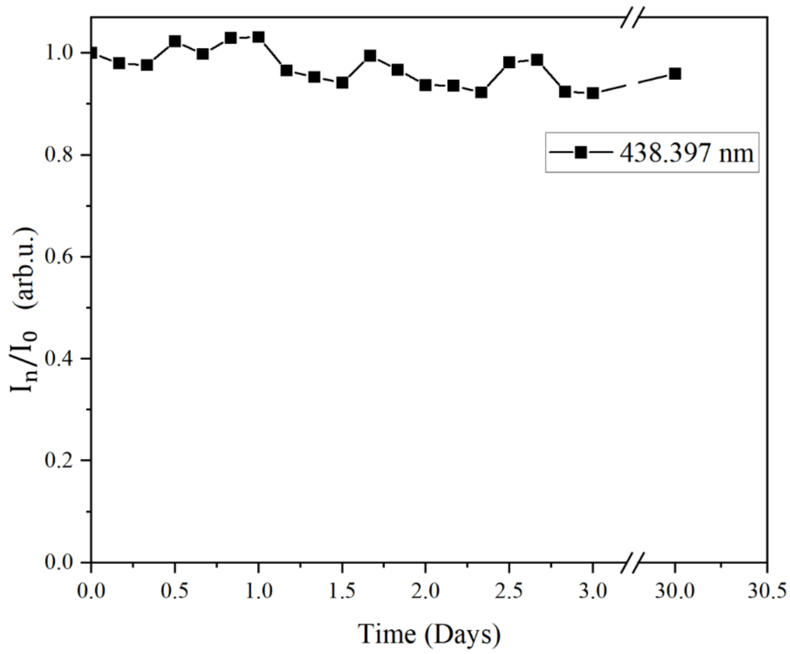


Figure 6-35 Intensity changes at 438.387 nm during the commission of the field test

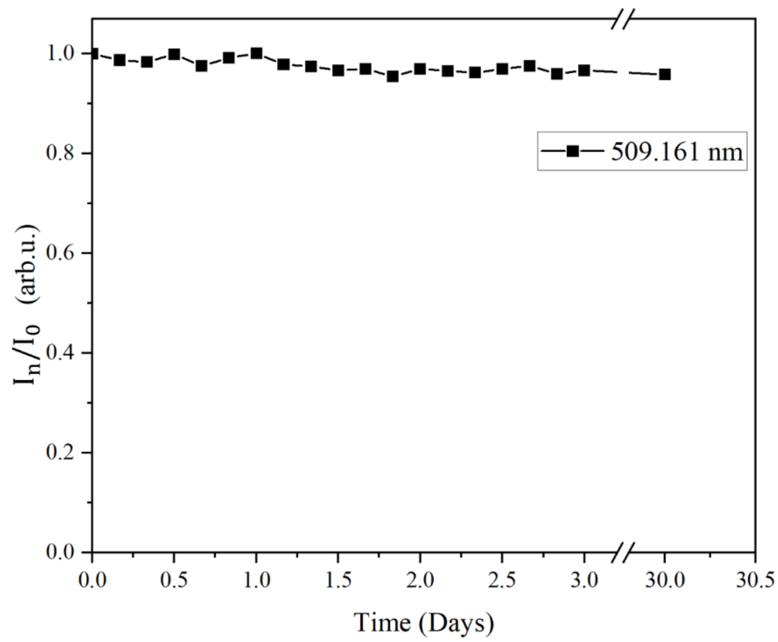


Figure 6-36 Intensity changes at 509.161 nm during the commission of the field test

## 6.4 Conclusions

In this chapter, a novel fluorescence-based sensor for monitoring sulphate and fluorescence-based sensing system for monitoring chloride and sulphate inside concrete were developed. The fluorescence-based sensor for monitoring sulphate employs the scandium-morin complex as the fluorescent sensing element. The fluorescence-based sensing system for monitoring chloride and sulphate employs dual sensing elements.

As for the fluorescence-based sensor for monitoring sulphate, the fluorescence intensity of scandium-morin complex proportionally correlates with the concentration of sulphate and the relationship is in accordance with the Stern-Volmer law.

Then an embeddable fluorescence-based sensing system for monitoring chloride and sulphate was built upon the chloride sensor and sulphate sensor. The sensing system had two peaks, one sensitive to chloride and the other sensitive to sulphate. To validate the performance of the sensing system in the field, a commission of field tests was carried out in a wave wall at Lei Yue Mun. The chloride sensitive peak and sulphate sensitive peak had a slow downward trend during the commission. The intensity fluctuation of chloride sensitive peak was larger than that of sulphate sensitive peak. The results showed that the sensing system worked properly after being embedded in the concrete, collected and uploaded the data to cloud server automatically during the commission. The developed embeddable fluorescence-based sensing system for monitoring chloride and sulphate shows great potential in the on-site application of monitoring chemical parameters.

Besides, this study showed the unique advantage of fiber optic sensing system, multiplexing capabilities. Multi-parameter sensors have various advantages like mitigating inaccuracies inherent in single-sensor systems by enabling cross-validation, costing less for maintenance and unlocking insights into variable interactions. For example, one sensor probe can monitor two parameters simultaneously, with this sensor probe, the package size and the number of armored fiber cable can be reduced in the on-site monitoring of chemical parameters. Thus saving the cost of sensing system. Furthermore, this sensor can improve accuracy through intercalibration from two different sensing elements.The development of this sensor capable of simultaneously monitoring chloride and sulphate ions simplifies deployment, lowers operational costs, increases accuracy.

# CHAPTER 7. CONCLUSIONS AND FUTURE WORK

## 7.1 Summary

Chemical parameters like relative humidity, chloride, and sulphate will accelerate deterioration. Monitoring the chemical parameters inside the concrete is critical to detect deterioration, assess the remaining service life, minimize maintenance costs, and prevent major accidents. Field application of fiber optic sensing system for monitoring chemical parameters inside concrete is rare and the relationship between the signals from fiber optic sensing system and chemical parameters is complex. To address these gaps, this thesis explores the field application of embeddable fiber optic sensing systems for monitoring chemical parameters inside concrete including FBG-based sensing system and fluorescence-based sensing system and applies a GP model to analyze the data collected from the long-term field test of fiber optic sensing system. The major tasks completed in this thesis can be summarized as follows:

Develop an FBG-based sensing system for monitoring relative humidity inside the concrete structure. Install the developed embeddable FBG-based sensing system for monitoring relative humidity inside concrete in a concrete beam sample placed in an exposure site to validate the performance of the developed sensing system (Chapter 3).

Train a Gaussian Process model with data collected from the long-term field test of the FBG-based sensing system for monitoring relative humidity installed in the exposure site and data collected from the automatic weather buoy to predict the relative humidity inside the concrete beam sample (Chapter 4).

Develop a fluorescence-based chloride sensor. Test the performance of the developed sensor in chloride solutions, solutions containing diverse ions for selectivity assessment, concrete simulation solutions with different pH values, mortar specimens, and high humidity chamber (Chapter 5).

Develop an embeddable fluorescence-based sensing system for monitoring chloride and sulphate inside concrete. Install the developed fluorescence-based sensing system in the field to validate the performance (Chapter 6).

## 7.2 Conclusions

The major findings and conclusions are summarized as follows:

**Task 1**: Development of an embeddable FBG-based sensing system for monitoring relative humidity inside concrete and field validation

- The FBG-based sensor with one polyimide-coated grating for humidity sensing and an uncoated grating for temperature compensation is able to monitor relative humidity after being embedded inside the concrete beam sample, which shows great potential of the field application of FBG-based sensors in chemical parameters monitoring inside concrete.
- The sensing system, comprising sensor probes, armored fiber optic cables, an automatic data collection, and an automatic data transmission system, demonstrated robust performance over a two-year period field test at the

HZMB exposure site. The results show that the application of FBG-based sensing system in the field is feasible and can provide relative humidity for more comprehensive parameters related with concrete deterioration.

- Comparative analysis with a commercial sensing system revealed a consistent temperature and a consistent 20% lower humidity reading from the FBG-based sensors, attributed to differences in sensor installation and protection methods. These results highlight the importance of sensor installation and protection and provide valuable experience for future field applications.

**Task 2**: Machine learning aided data analysis with data from long-term field tests of FBG-based sensing system for monitoring relative humidity inside concrete

- GP model provides a viable method for predicting in-beam humidity using historical monitored in-beam humidity and external environmental data. The GP model's probabilistic framework provided predictions with 90% confidence level, which consistently encapsulated the majority of measured humidity values across multiple channels and seasonal conditions.
- The results show GP models excel in modelling complex nonlinear relationships, which is common in fiber optic sensing system data analysis. These results highlight the importance of applying machine learning methods to analyze massive data collected from fiber optic sensing system.

**Task 3**: Development of an embeddable fluorescence-based sensor for monitoring chloride inside the concrete

- The performance of the developed fluorescence-based chloride sensor is tested with chloride solution, concrete simulation solution with different pH values, and solutions containing diverse ions for selectivity assessment. The results show that fluorescence-based chloride sensors are sensitive to chloride ions, stable under different pH values, and insensitive to other ions. These tests show unique advantages of fluorescence-based sensors like inherent sensitivity, selectivity, and real-time detection capabilities.
- The response of fluorescence-based sensors after being embedded in mortar samples is tested as well. The results show that the sensor can detect chloride ions, the sensor's sensitive depths are better than 3 mm and the sensing accuracy for chloride concentration is better than 80%. These tests show that fluorescence-based sensors work well after being embedded in mortar samples and show great possibility of applying fluorescence-based sensors in monitoring chemical parameters inside the concrete.
- The durability of developed fluorescence-based sensors is tested in an environmental chamber. The results show that although degradation was observed on the surface of the armored optical fiber cable, the signal from the sensor can be transmitted by the armored optical fiber cable normally.

It shows that in field applications; the sensing system needs to be better protected to avoid possible excessive degradation.

**Task 4:** Development of an embeddable fluorescence-based sensing system for monitoring chloride and sulphate inside the concrete and field validation

- Scandium-morin fluorescent complex and the film transformed with cellulose acetate are sensitive to sulphate ions. The scandium-morin fluorescent complex with a molar concentration ratio of 2:1 has the highest peak intensity in the excitation-emission map.
- The fluorescence-based sensor using both quinine and scandium-morin complex can monitor chloride and sulphate at the same time. By applying these sensors, the package size can be reduced, the number of armored optic fiber cables and spectrometers can be decreased, thus saving the cost of the structural health monitoring system and can improve accuracy through intercalibration from two different sensing elements. The result extends the application of fluorescence-based sensors in chemical parameters monitoring.
- The commissioning of field tests of the embeddable fluorescence-based sensing system for monitoring chloride and sulphate was carried out in the wave wall project at Lei Yue Mun. The chloride sensitive peak and sulphate sensitive peak had a slow downward trend during the commission. The intensity fluctuation of chloride sensitive peak was larger than that of sulphate sensitive peak. The power consumption of the

system was low and with solar panels the system can operate stably without an external power supply. The spectrometer, laser source and controller in the fluorescence-based sensing system have compact size, thus in field application, the system can be installed with minimum influence on the concrete structure. This test shows a great possibility of applying fluorescence-based sensing system for monitoring chemical parameters inside concrete.

## 7.3 Future Work

The future work is summarized as follows.

- As for the FBG-based relative humidity sensors, in the current comparative study with commercial sensors, the relative humidity collected from the FBG sensors is 20% lower than that from commercial sensors. These results may be caused by the installation of the commercial sensor probe. In future work, more waterproof measures need to be applied to ensure the commercial sensors are not affected by the external environment. Besides, to gain the strategic locations to put the FBG sensor, tests with FBG sensors installed in different depths, dirctions, will be carried out.
- As for the prediction of relative humidity inside the concrete beam, the environmental data is from an automatic weather buoy which is not in the exposure site. In the future, a relative humidity sensor installed in the exposure site may improve the model accuracy. Comparative study with

other machine learning methods can more comprehensively explore the application of machine learning in fiber optic sensing system data analysis. Apart from this, future work could explore extending this framework to other structural parameters (e.g., strain, corrosion) and environmental parameters, as well as incorporating additional covariates (e.g., wind speed, solar radiation) to enhance prediction range.

- As for the fluorescence-based sensing system for monitoring chloride, calibration before installation of the sensing system to the mortar specimen is needed. Besides, the free chloride concentration can be obtained with penetration method to directly compare free chloride obtained from the fluorescence-based sensor and obtained from penetration.
- As for the fluorescence-based sensing system for monitoring chloride and sulphate, replacement of the current solar panel with a larger one to meet the long-term stable power demand of the fluorescence-based sensing system installed in the wave wall project at Lei Yue Mun is needed.
- Besides more performance tests in concrete simulation solutions with different pH values, under different temperature, in mortar samples will study the fluorescence-based sensors for monitoring chloride and sulphate more comprehensively.
- The response of the fluorescence-based sensor for monitoring chloride and sulphate to sulphate and chloride solutions is complex, current

separation is based on 2 peaks in the fluorescence intensity curve. In the future work, more tests with different concentrations of sulphate and chloride may increase the separation accuracy. Besides, machine learning may be another way to increase separation accuracy.

- The penetration height of chloride ion is measured with potentiometric titration method in this study. X-Ray Computed Tomography (X-CT) is a possible approach to achieve non-destructive monitoring of chloride. X-CT applies X-rays to generating a set of radiographs of the object, then the radiographs of $360^{\circ}$ will be converted into a three-dimensional volume with reconstruction. The greyscale values in the reconstructed model are representative of the relative attenuation of the X-rays. Brighter grey values indicate highly attenuating material, and darker grey values represent less attenuating material. In the natural penetration experiment, heavy metal solutions can be used and in X-CT reconstructed model the grey values will be different. Thus, the penetration height can be monitored without destroying mortar specimens.

# REFERENCE

Abi Kaed Bey S.K., Chun Lam C.C., Sun T., and Grattan K.T.V., 2008. Chloride ion optical sensing using a long period grating pair. *Sensors and Actuators A: Physical*. 141: 390-395.

Adachi N., Kaneko Y., Sekiguchi K., Sugiyama H., and Sugeno M., 2015. pH-responsive fluorescence chemical sensor constituted by conjugated polymers containing pyridine rings. *Luminescence*. 30: 1308-1312.

Alloghani M., Al-Jumeily D., Mustafina J., Hussain A., Aljaaf A.J., Berry M.W., Yap B.W., and Mohamed A., 2020. *A systematic review on supervised and unsupervised machine learning algorithms for data science*. Springer International Publishing.

Almubaied O., Chai H.K., Islam M.R., Lim K.S., and Tan C.G., 2017. Monitoring corrosion process of reinforced concrete structure using FBG strain sensor. *Institute of Electrical and Electronics Engineers Transactions on Instrumentation and Measurement*. 66: 2148-2155.

Alwis L., Sun T., and Grattan K.T.V., 2013. Analysis of polyimide-coated optical fiber long period grating-based relative humidity sensor. *Institute of Electrical and Electronics Engineers Sensors Journal*. 13: 767-771.

Alwis L.S.M., Sun T., and Grattan K.T.V., 2016. Fibre Grating-based sensor design for humidity measurement in chemically harsh environment. *Procedia Engineering*. 168: 1317-1320.

An J.L., Jin Y.X., Sun M.M., and Dong X.Y., 2014. Relative humidity sensor based on SMS fiber structure with two waist-enlarged tapers. *Institute of Electrical and Electronics Engineers Sensors Journal*. 14: 2683-2686.

Angst U., Elsener B., Larsen C.K., and Vennesland Ø., 2009. Critical chloride content in reinforced concrete — A review. *Cement and Concrete Research*. 39: 1122-1138.

Azad A.K., Wang L., Guo N., Tam H.Y., and Lu C., 2016. Signal processing using artificial neural network for BOTDA sensor system. *Optics Express*. 24: 6769-6782.

Barroca N., Borges L.M., Velez F.J., Monteiro F., Górski M., and Castro Gomes J., 2013. Wireless sensor networks for temperature and humidity monitoring within concrete structures. *Construction & Building Materials*. 40: 1156-1166.

Bartelmess J., Zimmek D., Bartholmai M., Strangfeld C., and Schaferling M., 2020. Fibre optic ratiometric fluorescence pH sensor for monitoring corrosion in concrete. *Analyst*. 145: 2111-2117.

Blumentritt M., Melhorn K., Flachsbarth J., Kroener M., Kowalsky W., and Johannes H.H., 2008. A novel fabrication method of fiber-optical planar transmission sensors for monitoring pH in concrete structures. *Sensors and Actuators B: Chemical*. 131: 504-508.

Bolse N., Habermehl A., Eschenbaum C., and Lemmer U., 2018. *Fluorescence Quenching Sensor Arrays for the Discrimination of Nitroaromatic Vapors*. IGI Global: United States.

Bouteiller V., Cherrier J.F., L'Hostis V., Rebolledo N., Andrade C., and Marie Victoire E., 2012. Influence of humidity and temperature on the corrosion of reinforced concrete prisms. *European Journal of Environmental and Civil Engineering*. 16: 471-480.

Brault A., and Hoult N., 2019. Monitoring reinforced concrete serviceability performance using fiber optic sensors. *American Concrete Institute Structural Journal*. 116: 57-70.

Butcher J., Day C., Austin J.C., Haycock P.W., Verstraeten D., and Schrauwen B., 2014. Defect detection in reinforced concrete using random neural architectures. *Computer-Aided Civil and Infrastructure Engineering*. 29: 191-207.

Cai Q.Y., Li J., Ge J., Zhang L., Hu Y.L., Li Z.H., and Qu L.B., 2015. A rapid fluorescence “switch-on” assay for glutathione detection by using carbon dots–MnO2 nanocomposites. *Biosensors & Bioelectronics*. 72: 31-36.

Campanella C.E., Cuccovillo A., Campanella C., Yurt A., and Passaro V.M.N., 2018. Fibre Bragg grating based strain sensors: Review of technology and applications. *Sensors*. 18: 3115.

Caponero M., D'Amato R., Polimadei A., and Terranova G., 2018. Polymer-coated FBG humidity sensors for monitoring cultural heritage stone artworks. *Measurement*. 125: 325-329.

Čápová K., Velebil L., and Včelák J., 2020. Laboratory and in-situ testing of integrated fbg sensors for shm for concrete and timber structures. *Sensors* 20: 1661.

Chai J., Liu Q., Liu J.X., and Zhang D.D., 2018. Optical fiber sensors based on novel polyimide for humidity monitoring of building materials. *Optical Fiber Technology*. 41: 40-47.

Chao J.B., Wang H.J., Zhang Y.B., Yin C.X., Huo F.J., Song K.L., Li Z.Q., Zhang T., and Zhao Y.Q., 2017. A novel "donor-pi-acceptor" type fluorescence probe for sensing pH: mechanism and application in vivo. *Talanta*. 174: 468-476.

Che Q., Wen H., Li X., Peng Z., and Chen K.P., 2019. Partial discharge recognition based on optical fiber distributed acoustic sensing and a convolutional neural network. *Institute of Electrical and Electronics Engineers Access*. 7: 101758-101764.

Chen S.Z., Feng D.C., and Han W.S., 2020. Comparative study of damage detection methods based on long-gauge fbg for highway bridges. *Sensors*. 20: 3623.

Chen W., and Dong X.P., 2012. Modification of the wavelength-strain coefficient of FBG for the prediction of steel bar corrosion embedded in concrete. *Optical Fiber Technology*. 18: 47-50.

Chen Y.Z., Tang F.J., Bao Y., Tang Y., and Chen G.D., 2016. A Fe-C coated long-period fiber grating sensor for corrosion-induced mass loss measurement. *Optics Letters*. 41: 2306-2309.

Correia S.F., Antunes P., Pecoraro E., Lima P.P., Varum H., Carlos L.D., Ferreira R.A., and Andre P.S., 2012. Optical fiber relative humidity sensor based on a FBG with a di-ureasil coating. *Sensors*. 12: 8847-8860.

Corres J.M., Del Villar I., Matias I.R., and Arregui F.J., 2007. Fiber-optic pH-sensors in long-period fiber gratings using electrostatic self-assembly. *Optics Letters*. 32: 29-31.

Corres J.M., Matias I.R., del Villar I., and Arregui F.J., 2007. Design of pH sensors in long-period fiber gratings using polymeric nanocoatings. *Institute of Electrical and Electronics Engineers Sensors Journal*. 7: 455-463.

Davis M., Hoult N.A., and Scott A., 2017. Distributed strain sensing to assess corroded RC beams. *Engineering Structures*. 140: 473-482.

Demchenko A.P., 2020. *Introduction to fluorescence sensing. Volume 1, Materials and devices*. Springer: Switzerland.

Derinkuyu S., Ertekin K., Oter O., Denizalti S., and Cetinkaya E., 2007. Fiber optic pH sensing with long wavelength excitable Schiff bases in the pH range of 7.0-12.0. *Analytica Chimica Acta*. 588: 42-49.

Dervilis N., 2013. A machine learning approach to structural health monitoring with a view towards wind turbines. University of Sheffield.

des Tombe B., Schilperoort B., and Bakker M., 2020. Estimation of temperature and associated uncertainty from fiber-optic Raman-spectrum distributed temperature sensing. *Sensors*. 20: 2235.

Dhir R.K., Jones M.R., and McCarthy M.J., 1994. PFA concrete: Chloride-induced reinforcement corrosion. *Magazine of Concrete Research*. 46: 269-277.

Dissanayake K.P.W., Wu W.P., Nguyen H., Sun T., and Grattan K.T.V., 2018. Graphene-oxide-coated long-period grating-based fiber optic sensor for relative humidity and external refractive index. *Journal of Lightwave Technology*. 36: 1145-1151.

Duong H.D., Sohn O.J., Lam H.T., and Rhee J.I.l., 2006. An optical pH sensor with extended detection range based on fluoresceinamine covalently bound to sol–gel support. *Microchemical Journal*. 84: 50-55.

Fan L., Bao Y., and Chen G.D., 2018. Feasibility of distributed fiber otic sensor for corrosion monitoring of steel bars in reinforced concrete. *Sensors*. 18: 3722.

Fan L., Tan X., Zhang Q.H., Meng W.N., Chen G.D., and Bao Y., 2020. Monitoring corrosion of steel bars in reinforced concrete based on helix strains measured from a distributed fiber optic sensor. *Engineering Structures*. 204: 110039.

Feng Q.G., Chen Z., Gao Q., Yang L.F., Wang Y., Han Y., Zhang H. X., Chen F., and Wen J., 2012. The Relationship between the free and the bound chloride in high performance concrete. *Applied Mechanics and Materials*. 117-119: 1387-1390.

Fernandez Castellon D.R., Fenerci A., and Øiseth O.A., 2021. A comparative study of wind-induced dynamic response models of long-span bridges using artificial neural networks, support vector regression and buffeting theory. *Journal of Wind Engineering and Industrial Aerodynamics*. 209: 1-23.

Figueira R.B., Sadovski A., Melo A.P., and Pereira E.V., 2017. Chloride threshold value to initiate reinforcement corrosion in simulated concrete pore solutions: The influence of surface finishing and pH. *Construction & Building Materials*. 141: 183-200.

Fu M.Y., Lin G.R., Liu W.F., and Wu C.W., 2011. Fiber-optic humidity sensor based on an air-gap long period fiber grating. *Optical Review*. 18: 93-95.

Gao J.Q., Wu J., Li J., and Zhao X.M., 2011. Monitoring of corrosion in reinforced concrete structure using Bragg grating sensing. *Non-Destructive Testing and Evaluation International*. 44: 202-205.

Gong J.J., Tanner M.G., Venkateswaran S., Stone J.M., Zhang Y.C., and Bradley M., 2020. A hydrogel-based optical fibre fluorescent pH sensor for observing lung tumor tissue acidity. *Analytica Chimica Acta*. 1134: 136-143.

Goyal P., Malik H., Sharma R., Mishra K.K., Panigrahi B.K., Tiwari S., Singh P.K., and Trivedi M.C., 2018. *Application of evolutionary reinforcement learning (ERL) approach in control domain: A review*. Springer: Singapore.

Grant Jacob J.A., Jain S., Xie Y.H., Mackay B.S., McDonnell M.D.T., Praeger M., Loxham M., Richardson D.J., Eason R.W., and Mills B., 2019. Fibre-optic based particle sensing via deep learning. *Journal of Physics: Photonics*. 1: 44004.

Guo C.R., Fan L., and Chen G.D., 2020. Corrosion-induced mass loss measurement under strain conditions through Gr/AgNW-based, Fe-C coated LPFG sensors. *Sensors*. 20: 1598.

Guo C.R., Fan L., Wu C.L., Chen G.D., and Li W., 2019. Ultrasensitive LPFG corrosion sensor with Fe-C coating electroplated on a Gr/AgNW film. *Sensors and Actuators B: Chemical*. 283: 334-342.

Guo J.Y., Shi B., Sun M.Y., Zhang C.C., Wei G.Q., and Liu J., 2021. Characterization of an ORMOCER®-coated FBG sensor for relative humidity sensing. *Measurement*. 171: 108851.

HE J.Y., 2020. Development of optical fiber SO_4~(2-) ion sensor and its application in concrete inspection. Wuhan University of Technology.

Hewlett P.C., and Lea F.M., 1998. *Lea's chemistry of cement and concrete*. Arnold: London.

Hong C.Y., Zhang Y.F., Li G.W., Zhang M.X., and Liu Z.X., 2017. Recent progress of using Brillouin distributed fiber optic sensors for geotechnical health monitoring. *Sensors and Actuators A: Physical*. 258: 131-145.

Hong C.Y., Zhang Y.F., Zhang M.X., Leung L.M.G., and Liu L.Q., 2016. Application of FBG sensors for geotechnical health monitoring, a review of sensor design, implementation methods and packaging techniques. *Sensors and Actuators A: Physical*. 244: 184-197.

Hromadka J., Mohd Hazlan N.N., Hernandez F.U., Correia R., Norris A., Morgan S.P., and Korposh S., 2019. Simultaneous in situ temperature and relative humidity monitoring in mechanical ventilators using an array of functionalised optical fibre long period grating sensors. *Sensors and Actuators B: Chemical*. 286: 306-314.

Hu P.B., Chen Z.M., Yang M., Yang J.Y., and Zhong C., 2015. Highly sensitive liquid-sealed multimode fiber interferometric temperature sensor. *Sensors and Actuators A: Physical*. 223: 114-118.

Hu T., Zhao Y., and Song A.N., 2016. Fiber optic SPR sensor for refractive index and temperature measurement based on MMF-FBG-MMF structure. *Sensors and Actuators B: Chemical*. 237: 521-525.

Hu W.B., Cai H.L., Yang M.H., Tong X.L., Zhou C.M., and Chen W., 2011. Fe–C-coated fibre Bragg grating sensor for steel corrosion monitoring. *Corrosion Science*. 53: 1933-1938.

Huang Q.D., Lv C.H., Yuan X.L., He M., Lai J.P., and Sun H., 2021. A novel fluorescent optical fiber sensor for highly selective detection of antibiotic ciprofloxacin based on replaceable molecularly imprinted nanoparticles composite hydrogel detector. *Sensors and Actuators B: Chemical*. 328: 129000.

Huang Y., Gao Z., Chen G.D., and Xiao H., 2013. Long period fiber grating sensors coated with nano iron/silica particles for corrosion monitoring. *Smart Materials and Structures*. 22: 75018.

Huang Y., Tang F.J., Liang X., Chen G.D., Xiao H., and Azarmi F., 2014. Steel bar corrosion monitoring with long-period fiber grating sensors coated with nano iron/silica particles and polyurethane. *Structural Health Monitoring*. 14: 178-189.

James S.W., and Tatam R.P., 2003. Optical fibre long-period grating sensors: characteristics and application. *Measurement Science and Technology*. 14: 49-61.

Jayaraman S., and Verkman A.S., 2000. Quenching mechanism of quinolinium-type chloride-sensitive fluorescent indicators. *Biophysical Chemistry*. 85: 49-57.

Jee Y., Yu Y., Abernathy H.W., Lee S., Kalapos T.L., Hackett G.A., and Ohodnicki P.R., 2018. Plasmonic conducting metal oxide-based optical fiber sensors for chemical and intermediate temperature-sensing applications. *American Chemical Society: Applied Materials & Interfaces*. 10: 42552-42563.

Jiang H.L., Feng D.W., Wang K.C., Gu Z.Y., Wei Z.W., Chen Y.P., and Zhou H.C., 2013. An exceptionally stable, porphyrinic Zr metal-organic framework exhibiting pH-dependent fluorescence. *Journal of the Amercian Chemical Society*. 135: 13934-13938.

Jorgenson R.C., and Yee S.S., 1993. A fiber-optic chemical sensor based on surface plasmon resonance. *Sensors and Actuators. B, Chemical*. 12: 213-220.

Kahandawa G.C., Epaarachchi J., Wang H., and Lau K.T., 2012. Use of FBG sensors for SHM in aerospace structures. *Photonic Sensors*. 2: 203-214.

Khandel O., Soliman M., Floyd R.W., and Murray C.D., 2021. Performance assessment of prestressed concrete bridge girders using fiber optic sensors and artificial neural networks. *Structure and Infrastructure Engineering*. 17: 605-619.

Khatib J., 2016. *Sustainability of construction materials*. Elsevier Science & Technology: Cambridge.

Koleva D.A., and Rendon Diaz Miron L.E., 2017. *Concrete durability : cementitious materials and reinforced concrete properties, behavior and corrosion resistance*. Springer: Switzerland.

Konstantaki M., Pissadakis S., Pispas S., Madamopoulos N., and Vainos N.A., 2006. Optical fiber long-period grating humidity sensor with poly(ethylene oxide)/cobalt chloride coating. *Applied Optics*. 45: 4567-4571.

Korposh S., Kodaira S., Selyanchyn R., Ledezma F.H., James S.W., and Lee S.W., 2018. Porphyrin-nanoassembled fiber-optic gas sensor fabrication: Optimization of parameters for sensitive ammonia gas detection. *Optics & Laser Technology*. 101: 1-10.

Kowarik S., Hussels M.T., Chruscicki S., Münzenberger S., Lämmerhirt A., Pohl P., and Schubert M., 2020. Fiber optic train monitoring with distributed acoustic sensing: Conventional and neural network data analysis. *Sensors*. 20: 450.

Kronenberg P., Rastogi P.K., Giaccari P., and Limberger H.G., 2002. Relative humidity sensor with optical fiber Bragg gratings. *Optics Letters*. 27: 1385-1387.

Laxmeshwar L.S., Jadhav M.S., Akki J.F., Raikar P., Kumar J., prakash O., Mahakud R., and Raikar U.S., 2018. Quantification of chloride and iron in sugar factory effluent using long period fiber grating chemical sensor. *Sensors and Actuators B: Chemical*. 258: 850-856.

Lea C., Vidal R., Reiter A., Hager G.D., Hua G., and Jégou H., 2016. *Temporal convolutional networks: A unified approach to action segmentation*. Springer International Publishing: Switzerland.

Lewis E., Sheridan C., O'Farrell M., King D., Flanagan C., Lyons W.B., and Fitzpatrick C., 2007. Principal component analysis and artificial neural network based approach to analysing optical fibre sensors signals. *Sensors and Actuators A: Physical*. 136: 28-38.

Li L.Z., and Lang Q.Y., 1990. PMBP-extraction and fluorescence determination of trace Sc with morin. *Rock and Mineral Analysis*. 9: 103-107.

Li P.F., Yan H.T., Xie Z.W., Zhao X.Y., and Han D.F., 2019. A bandwidth response humidity sensor with micro-nano fibre Bragg grating. *Optical Fiber Technology*. 53: 101998.

Li Q.S., Zhang X.L., Ma Y.H., Yang J.H., Cai L., Liu Q.A., and Shi J.G., 2018. Sodium chloride concentration sensor based on long period fiber grating with dual resonant peak. *Journal of Physics: Conference Series*. 1065: 252021.

Li S.G., Wang W.T., Lu B., Du X., Dong M.M., Zhang T.B., and Bai Z.F., 2023. Long-term structural health monitoring for bridge based on back propagation neural network and long and short-term memory. *Structural Health Monitoring*. 22: 2325-2345.

Li W., Cheng H., Xia M., and Yang K.C., 2013. An experimental study of pH optical sensor using a section of no-core fiber. *Sensors and Actuators A: Physical*. 199: 260-264.

Lin H.F., Liu F.F., Dai Y.T., and Mumtaz F., 2020. Relative humidity sensor based on FISM-SMS fiber structure coated with PVA film. *Optik*. 207: 164320.

Lin H.T., Huang J., and Ding L.Y., 2019. A recyclable optical fiber sensor based on fluorescent carbon dots for the determination of ferric ion concentrations. *Journal of Lightwave Technology*. 37: 4815-4822.

Lipski A., 2020. Change of specimen temperature during the monotonic tensile test and correlation between the yield strength and thermoelasto-plastic limit stress on the example of aluminum alloys. *Materials*. 14: 13-19.

Liu D.W., Gong C., Tang Y., Jian Y.H., Cao K.P., and Chen H.F., 2022. Evaluation of corrosion damage in sulfate-attacked concrete by CT, ultrasonic pulse velocity testing and AHP methods. *Sensors*. 22: 3037.

Liu H.L., Liang H.H., Sun M.M., Ni K., and Jin Y.X., 2014. Simultaneous measurement of humidity and temperature based on a long-period fiber grating inscribed in fiber loop mirror. *Institute of Electrical and Electronics Engineers Sensors Journal*. 14: 893-896.

Liu H.Y., Liang D.K., Zeng J., Jin J., Wu J., and Geng J., 2012. Design of a long-period fiber grating sensor for reinforcing bar corrosion in concrete. *Journal of Intelligent Material Systems and Structures*. 23: 45-51.

Liu J.Z., Ji D.Y., Meng H.M., Zhang L., Wang J.Y., Huang Z.M., Chen J., Li J.J., and Li Z.H., 2018. A portable fluorescence biosensor for rapid and sensitive glutathione detection by using quantum dots-based lateral flow test strip. *Sensors and Actuators. B, Chemical*. 262: 486-492.

Liu Y., Wang L.W., Zhang M., Tu D.S., Mao X.H., and Liao Y.B., 2007. Long-period grating relative humidity sensor with hydrogel coating. *Institute of Electrical and Electronics Engineers Photonics Technology Letters*. 19: 880-882.

Lv H.F., Zhao X.F., Zhan Y.L., and Gong P., 2017. Damage evaluation of concrete based on Brillouin corrosion expansion sensor. *Construction & Building Materials*. 143: 387-394.

Ma R.R., Chen Z.W., Wang S.N., Zhou C.H., Li Y.W., Lu J., Li D.C., and Dou J.M., 2017. PH-dependent fluorescence sensing activities of two water-stable 2-D zinc(II) compounds. *Inorganic Chemistry Communications*. 81: 59-66.

Maierhofer C., Reinhardt H.W., and Dobmann G., 2010. *Non-destructive evaluation of reinforced concrete structures: Deterioration processes and standard test methods*. Elsevier Science & Technology: Cambridge.

Majumder M., Gangopadhyay T.K., Chakraborty A.K., Dasgupta K., and Bhattacharya D.K., 2008. Fibre Bragg gratings in structural health monitoring—Present status and applications. *Sensors and Actuators A: Physical*. 147: 150-164.

Manie Y.C., Li J.W., Peng P.C., Shiu R.K., Chen Y.Y., and Hsu Y.T., 2020. Using a machine learning algorithm integrated with data de-noising techniques to optimize the multipoint sensor network. *Sensors*. 20: 1070.

Manzanares Palenzuela C.L., and Pumera M., 2018. (Bio)Analytical chemistry enabled by 3D printing: Sensors and biosensors. *Trends in Analytical Chemistry*. 103: 110-118.

Martín Pérez B., Zibara H., Hooton R.D., and Thomas M.D.A., 2000. A study of the effect of chloride binding on service life predictions. *Cement and Concrete Research*. 30: 1215-1223.

Massaroni C., Caponero M.A., D'Amato R., Lo Presti D., and Schena E., 2017. Fiber Bragg grating measuring system for simultaneous monitoring of temperature and humidity in mechanical ventilation. *Sensors*. 17: 749.

Mishra S.K., Zou B., and Chiang K.S., 2017. Wide-range pH sensor based on a smart-hydrogel-coated long-period fiber grating. *Institute of Electrical and Electronics Engineers Journal of Selected Topics in Quantum Electronics*. 23: 284-288.

Mohammed T.U., and Hamada H., 2003. Relationship between free chloride and total chloride contents in concrete. *Cement and Concrete Research*. 33: 1487-1490.

Moradi V., Akbari M., and Wild P., 2019. A fluorescence-based pH sensor with microfluidic mixing and fiber optic detection for wide range pH measurements. *Sensors and Actuators A: Physical*. 297: 111507.

Neves A.C., González I., Leander J., and Karoumi R., 2017. Structural health monitoring of bridges: a model-free ANN-based approach to damage detection. *Journal of Civil Structural Health Monitoring*. 7: 689-702.

Nguyen T.H., Venugopala T., Chen S.Y., Sun T., Grattan K.T.V., Taylor S.E., Basheer P.A.M., and Long A.E., 2014. Fluorescence based fibre optic pH sensor for the pH 10–13 range suitable for corrosion monitoring in concrete structures. *Sensors and Actuators B: Chemical*. 191: 498-507.

Ni Y.Q., Ding S.Q., Han B.G., and Wang H.P., 2019. Layer-by-layer assembly of polyelectrolytes-wrapped multi-walled carbon nanotubes on long period fiber grating sensors. *Sensors and Actuators B: Chemical*. 301: 127120.

Nidhi, Tiwari U., Panwar N., Kaler R.S., Bhatnagar R., and Kapur P., 2013. Long period fiber grating humidity sensor with gelatin/cobalt chloride coating. *Institute of Electrical and Electronics Engineers Sensors Journal*. 13: 4139-4140.

Noorani R., 2018. *3D printing : technology, applications, and selection*. Chemical & Rubber & Company Press: Boca Raton.

Panhwar Q.K., Memon S., and Bhanger M.I., 2010. Synthesis, characterization, spectroscopic and antioxidation studies of Cu(II)–morin complex. *Journal of Molecular Structure*. 967: 47-53.

Pęgier M., Dróżdż P., Pomarański P., and Pyrzyńska K., 2021. Magnetic hybrid nanoparticles modified with morin for the removal of Sc(III) from aqueous solutions. *Microchemical Journal*. 170: 106683.

Pereira K., Coimbra W., Lazaro R., Frizera Neto A., Marques C., and Leal Junior A.G., 2021. FBG-based temperature sensors for liquid identification and lquid lvel Estimation via rndom frest. *Sensors*. 21: 4568.

Possetti G.R.C., Kamikawachi R.C., Prevedello C.L., Muller M., and Fabris J.L., 2009. Salinity measurement in water environment with a long period grating based interferometer. *Measurement Science and Technology*. 20: 034003.

Poursaee A., 2016. *Corrosion of steel in concrete structures*. Elsevier, Woodhead Publishing: Duxford,.

Qi Y.F., Jia C., Tang L., Zhang X., Gong C.B., Liu Y.Y., and Liu X.Q., 2019. Research on temperature and humidity sensing characteristics of cascaded LPFG-FBG. *Optik*. 188: 19-26.

Qiao H., Lin Z., Sun X.T., Li W., Zhao Y.P., and Guo C.R., 2023. Fiber Optic-based durability monitoring in smart concrete: A state-of-art review. *Sensors* 23: 7810.

Rao Y.J., Y.P. Wang., Ran Z.L., and Zhu T., 2003. Novel fiber-optic sensors based on long-period fiber gratings written by high-frequency CO/sub 2/ laser pulses. *Journal of Lightwave Technology*. 21: 1320-1327.

Regier R., and Hoult N.A., 2015. Concrete deterioration detection using distributed sensors. *Structures and Buildings*. 168: 118-126.

Salehi H., and Burgueño R., 2018. Emerging artificial intelligence methods in structural engineering. *Engineering Structures*. 171: 170-189.

Sarkar S., Inupakutika D., Banerjee M., Tarhani M., Eghbal M. K., and Shadaram M. 2020. "Discrimination of strain and temperature effects on FBG-based sensor using machine learning." In *2020 Institute of Electrical and Electronics Engineers Photonics Conference*.

Sarkar S., Tarhani M., Khosravi Eghbal M., and Shadaram M., 2020. Discrimination between strain and temperature effects of a single fiber Bragg grating sensor using sidelobe power. *Journal of Applied Physics*. 127: 114503.

Shi X.M., Xie N., Fortune K., and Gong J., 2012. Durability of steel reinforced concrete in chloride environments: An overview. *Construction & Building Materials*. 30: 125-138.

Shi Y., Wang Y.Y., Zhao L., and Fan Z., 2019. An Event Recognition Method for Φ-OTDR Sensing System Based on Deep Learning. *Sensors*. 19: 3421-3421.

Shoukry S.N., William G.W., Downie B., and Riad M.Y., 2011. Effect of moisture and temperature on the mechanical properties of concrete. *Construction & Building Materials*. 25: 688-696.

Shu X.W., Zhang L., and Bennion I., 2002. Sensitivity characteristics of long-period fiber gratings. *Journal of Lightwave Technology*. 20: 255-266.

Taheri S., 2019. A review on five key sensors for monitoring of concrete structures. *Construction & Building Materials*. 204: 492-509.

Tan K.M., Tay C.M., Tjin S.C., Chan C.C., and Rahardjo H., 2005. High relative humidity measurements using gelatin coated long-period grating sensors. *Sensors and Actuators B: Chemical*. 110: 335-341.

Tang F.J., Chen Y.Z., Li Z.C., Tang Y., and Chen G.D., 2018. Application of Fe-C coated LPFG sensor for early stage corrosion monitoring of steel bar in RC structures. *Construction & Building Materials*. 175: 14-25.

Tang F.J., Li Z.C., Chen Y.Z., Li H.N., Huang J., and O'Keefe M.J., 2019. Monitoring passive film growth on steel using Fe-C coated long period grating fiber sensor. *Institute of Electrical and Electronics Engineers Sensors Journal*. 19: 6748-6755.

Tang F.J., Zhao L.Z., Tian H., Li H.N., and Li H., 2021. Localization and monitoring of initiation and propagation of corrosion-induced mortar cracking based on OFDR distributed optical fiber sensor. *Journal of Intelligent Material Systems and Structures*. 32: 1948-1965.

Tang F.J., Zhou G.S., Li H.N., and Verstrynge E., 2021. A review on fiber optic sensors for rebar corrosion monitoring in RC structures. *Construction & Building Materials*. 313: 125578.

Tang J.L., and Wang J.N., 2007. Measurement of chloride-ion concentration with long-period grating technology. *Smart Materials and Structures*. 16: 665-672.

Tariq A., Baydoun J., Remy C., Ghasemi R., Lefevre J.P., Mongin C., Dauzères A., and Leray I., 2021. Fluorescent molecular probe based optical fiber sensor dedicated to pH measurement of concrete. *Sensors and Actuators B: Chemical*. 327: 128906.

Theodosiou A., Min R., Leal-Junior A.G., Ioannou A., Frizera A., Pontes M.J., Marques C.A.F., and Kalli K., 2019. Long period grating in a multimode cyclic transparent optical polymer fiber inscribed using a femtosecond laser. *Optics Letters*. 44: 5346-5349.

Tou Z.Q., Chan C.C., Hong J., Png S., Eddie K.M.T., and Tan T.A.H., 2014. Double-pass Mach-Zehnder fiber interferometer pH sensor. *Journal of Biomedical Optics*. 19: 047002.

Urrutia A., Goicoechea J., Ricchiuti A.L., Barrera D., Sales S., and Arregui F.J., 2016. Simultaneous measurement of humidity and temperature based on a partially coated optical fiber long period grating. *Sensors and Actuators B: Chemical*. 227: 135-141.

Valeur B., and Berberan Santos M.N., 2012. *Molecular fluorescence: principles and applications, Second Edition*. Wiley-Verlag Chemie: Weinheim, Germany.

Venugopalan T., Sun T., and Grattan K.T.V., 2008. Long period grating-based humidity sensor for potential structural health monitoring. *Sensors and Actuators A: Physical*. 148: 57-62.

Verity B., and Bigger S.W., 1996. The dependence of quinine fluorescence quenching on ionic strength. *International Journal of Chemical Kinetics*. 28: 919-923.

Villar I.D., and Matias I.R., 2021. *Optical fiber sensors : fundamentals for development of optimized devices*. Wiley-Institute of Electrical and Electronics Engineers Press: Hoboken, New Jersey.

Wang B.W., Wang L., Yu C.Y., and Lu C., 2019. Long-distance BOTDA sensing systems using video-BM3D denoising for both static and slowly varying environment. *Optics Express*. 27: 36100-36113.

Wang X.F., Farrell G., Lewis E., Tian K., Yuan L.B., and Wang P.F., 2017. A humidity sensor based on a singlemode-side polished multimode–singlemode optical fibre structure coated with gelatin. *Journal of Lightwave Technology*. 35: 4087-4094.

Wen Z.Q., Song S.L., Wang C.X., Qu F.D., Thomas T.J., Hu T.T., Wang P., and Yang M.H., 2019. Large-scale synthesis of dual-emitting-based visualization sensing paper for humidity and ethanol detection. *Sensors and Actuators B: Chemical*. 282: 9-15.

Wu H., Wang L., Guo N., Shu C., and Lu C., 2017. Brillouin optical time-domain analyzer assisted by support vector machine for ultrafast temperature extraction. *Journal of Lightwave Technology*. 35: 4159-4167.

Xiao W., Liu F., Yan G.P., Shi W.G., Peng K.L., Yang X.Q., Li X.J., Yu H.C., Shi Z.Y., and Zeng H.H., 2020. Yttrium vanadates based ratiometric fluorescence probe for alkaline phosphatase activity sensing. *Colloids and Surfaces, B, Biointerfaces*. 185: 110618.

Xu W., Shi J., Yang X.C., Xu D.G., Rong F., Zhao J.F., and Yao J.Q., 2017. Relative humidity sensor based on no-core fiber coated by agarose-gel film. *Sensors*. 17: 2353.

Yang F., Hlushko R., Wu D., Sukhishvili S.A., Du H., and Tian F., 2019. Ocean salinity sensing using long-period fiber gratings functionalized with layer-by-layer hydrogels. *American Chemical Society Omega*. 4: 2134-2141.

Yang F., Sukhishvili S., Du H., and Tian F., 2017. Marine salinity sensing using long-period fiber gratings enabled by stimuli-responsive polyelectrolyte multilayers. *Sensors and Actuators B: Chemical*. 253: 745-751.

Ye X.W., Su Y.H., and Xi P., 2018. Statistical analysis of stress signals from bridge monitoring by FBG system. *Sensors*. 18: 491.

Yeo T.L., Sun T., Grattan K.T.V., Parry D., Lade R., and Powell B.D., 2005a. Characterisation of a polymer-coated fibre Bragg grating sensor for relative humidity sensing. *Sensors and Actuators B: Chemical*. 110: 148-156.

Yeo T.L., Sun T., Grattan K.T.V., Parry D., Lade R., and Powell B.D., 2005b. Polymer-coated fiber Bragg grating for relative humidity sensing. *Institute of Electrical and Electronics Engineers Sensors Journal*. 5: 1082-1089.

Yu P., Duan Y.H., Fan Q.X., and Tang S.W., 2020. Improved MPS model for concrete creep under variable humidity and temperature. *Construction & Building Materials*. 243: 118183.

Yu X.J., Childs P., Zhang M., Liao Y.B., Ju J., and Jin W., 2009. Relative humidity sensor based on cascaded long-period gratings with hydrogel coatings and fourier demodulation. *Institute of Electrical and Electronics Engineers Photonics Technology Letters*. 21: 1828-1830.

Yuan Q., Shi C.J., De Schutter G., Audenaert K., and Deng D.H., 2009. Chloride binding of cement-based materials subjected to external chloride environment – A review. *Construction & Building Materials*. 23: 1-13.

Zhang F., Hu Z.P., Wei F., Wen X., Li X.G., Dai L., and Liu L., 2021. Study on concrete deterioration in different NaCl-Na2SO4 solutions and the mechanism of Cl(-) diffusion. *Materials*. 14: 5054.

Zhang J.X., Shen X.Y., Qian M., Xiang Z., and Hu X.D., 2021. An optical fiber sensor based on polyimide coated fiber Bragg grating for measurement of relative humidity. *Optical Fiber Technology*. 61: 102406.

Zhang Y.J., Fu G.W., Liu Y., Bi W.H., and Li D., 2013. A novel fitting algorithm for Brillouin scattering spectrum of distributed sensing systems based on RBFN networks. *Optik - International Journal for Light and Electron Optics*. 124: 718-721.

Zhang Z.F., Zhang C., Tao X.M., Wang G.F., and Peng G.D., 2010. Inscription of polymer optical fiber Bragg grating at 962 nm and its potential in strain sensing. *Institute of Electrical and Electronics Engineers Photonics Technology Letters*. 22: 1562-1564.

Zhao X.F., Gong P., Qiao G.F., Lu J., Lv X.J., and Ou J.P., 2011. Brillouin corrosion expansion sensors for steel reinforced concrete structures using a fiber optic coil winding method. *Sensors*. 11: 10798-10819.

Zhao Y., Lei M., Liu S.X., and Zhao Q., 2018. Smart hydrogel-based optical fiber SPR sensor for pH measurements. *Sensors and Actuators B: Chemical*. 261: 226-232.

Zhao Y., Li X.G., Meng F.C., and Zhao Z., 2014. A vibration-sensing system based on SMS fiber structure. *Sensors and Actuators A: Physical*. 214: 163-167.

Zheng S.J., 2014. Long-period fiber grating moisture sensor with nano-structured coatings for structural health monitoring. *Structural Health Monitoring*. 14: 148-157.

Zheng Y., Zhu Z.W., Yi X., and Li W.J., 2019. Review and comparative study of strain-displacement conversion methods used in fiber Bragg grating-based inclinometers. *Measurement*. 137: 28-38.

Zheng Z.P., Sun X.N., and Lei Y., 2009. Monitoring corrosion of reinforcement in concrete structures via fiber Bragg grating sensors. *Frontiers of Mechanical Engineering*. 4: 316-319.